

DISSERTATION

LUMINESCENCE MEASUREMENTS INFORM A STRATEGY FOR UNLOCKING THE
FULL POTENTIAL OF CDTE-BASED PHOTOVOLTAICS

Submitted by

Pascal M. Jundt

Department of Physics

In partial fulfillment of the requirements

For the Degree of Doctor of Philosophy

Colorado State University

Fort Collins, Colorado

Spring 2023

Doctoral Committee:

Advisor: James R. Sites

Walajabad S. Sampath

Dylan C. Yost

Martin P. Gelfand

Darius Kuciauskas

Copyright by Pascal Jundt 2023

All Rights Reserved

ABSTRACT

LUMINESCENCE MEASUREMENTS INFORM A STRATEGY FOR UNLOCKING THE FULL POTENTIAL OF CDTE-BASED PHOTOVOLTAICS

Cadmium telluride (CdTe) photovoltaics are characterized by simplicity and speed of fabrication with low usage of materials, all of which translate into low cost. These significant advantages have earned CdTe the second-highest adoption rate of all photovoltaic technologies. However, conversion efficiencies, while functional, are significantly lower than the theoretical limit for this material. This discrepancy is almost entirely a discrepancy in voltage, and the so-called “voltage deficit” of CdTe has stubbornly persisted for decades. While many strategies are being pursued to attempt to reduce the voltage deficit, this issue is fundamentally one of excessive nonradiative recombination due to defects within the absorber material, as will be demonstrated in this dissertation.

Recombination is evaluated primarily by luminescence measurements, and as such this class of measurements is particularly relevant to the challenges faced by CdTe research today. The rate of recombination is parameterized by the carrier lifetime, and time-resolved photoluminescence (TRPL) is the most common method of determining this parameter in CdTe. Historically, accurate determination of bulk lifetime was as simple as extracting the time constant of the slowest component of a TRPL decay. However, significant gains in material passivation and doping over the last few years have both decreased the relative influence of trap-assisted recombination and increased the influence of p-n junction fields on TRPL measurements. Consequently, when measurements are performed on complete cells, extracting

the tail time constant from a TRPL decay no longer necessarily gives an accurate representation of the bulk material lifetime, and the result is distorted by field effect contributions. This fact is not necessarily well-known by the CdTe community, and extraction of the tail time constant is still the most common way to report lifetimes, even in measurements on complete state-of-the-art cells.

This dissertation demonstrates the skewing effects of junction fields, and identifies under which conditions they manifest and how. To probe field effects, external electrical bias was incorporated during TRPL measurements, which allows fairly precise manipulation of fields. Biased TRPL measurements were performed on a variety of samples, and a model was developed to substantiate and better explain the results. It was found that the same characteristics which enable good performance (high lifetime, doping, and mobility) are the same which add complexity to TRPL interpretation. It was also found that field effects can be effectively suppressed by significant forward bias, leading to far more accurate determination of bulk lifetime.

TRPL and external radiative efficiency (ERE) luminescence measurement results have indicated very low rates of nonradiative recombination and associated very high lifetime for some CdTe-based materials deposited at Colorado State University, particularly the cadmium selenium telluride (CdSeTe) alloy. While these attributes should allow voltages approaching 1 V and efficiencies on the order of 25%, when incorporated into “traditional” cell architectures these materials typically achieve middling performance at best, and often no performance at all.

To unlock the great potential indicated by luminescence measurements, a different cell architecture is proposed which aims to accommodate these materials and take advantage of their

characteristics. In an n-i-p configuration, an intrinsic absorber material is sandwiched between two carrier-selective contacts, at least one of which must be transparent. This design eliminates the requirement that the absorber be doped, which penalizes lifetime. Based on the findings of modeling reported here, undoped CdSeTe appears to be an ideal intrinsic layer material. The currently-utilized SnO₂:F/MgZnO front contact appears to be excellent as the n-type electron-selective layer. The one missing component is the p-type hole-selective layer; modeling in this dissertation describes in detail what attributes are required of this material. Most important is band alignment with CdSeTe, which should produce a valence band offset as close to zero as possible, and a conduction band offset which forms a sufficiently high electron barrier. Sufficient p-type doping is also quite important.

Based on these criteria, ZnTe was identified as a suitable candidate material, and several cells were fabricated with this architecture. While preliminary cells achieved relatively poor performance compared with traditional designs, J-V curves were surprisingly well-behaved, and the almost immediate achievement of functioning cells using an entirely new approach is promising. Luminescence characterization of these structures identified several areas for improvement, namely the use of a p-type dopant other than copper and the replacement of ZnTe with another material with similar band structure but more compatible lattice constant.

ACKNOWLEDGMENTS

I would like to thank my advisor, Dr. Sites, for being an excellent source of knowledge and guidance, and for allowing (even encouraging) me to strike a healthy work-life balance, making my experience as a graduate student a pleasant one, and enabling positive growth in this period of my life both professionally *and* personally. The importance of this cannot be overstated. I would also like to thank the other members of my committee, Dr. Yost and Dr. Gelfand, Dr. Sampath for his enthusiasm and perspective, and particularly Dr. Kuciauskas for his mentorship.

I would also like to thank my current and former colleagues Adam Danielson, Carey Reich, Taylor Hill, Camden Kasik, Daniel Shaw, Tushar Shimpi, Alex Bothwell, Ramesh Pandey, Anthony Nicholson, Akash Shah, Aanand Thiyagarajan, Anna Kindvall, Kevan Cameron, Jen Drayton, and Amit Munshi variously for their knowledge, assistance, guidance, and viewpoints. All science is a team effort, and I have had the privilege of working with a great team.

Lastly, I must thank my loving partner, India, for providing the valuable sociological perspective which is far too often missing in the natural sciences. Our conversations have taught me so much and have significantly broadened my way of thinking. Her support and companionship has been invaluable for the past several years, and to her I am forever grateful.

The research described in the thesis has been supported in part by the U.S. Department of Energy's Solar Energy Technologies Office and by the National Science Foundation's Industry/University Cooperative Research Program, with some of the deposition materials provided by 5N Plus Inc. as in-kind support.

TABLE OF CONTENTS

ABSTRACT.....	ii
ACKNOWLEDGMENTS	v
LIST OF TABLES	ix
LIST OF FIGURES	x
LIST OF NOMENCLATURE.....	xii
CHAPTER 1. INTRODUCTION.....	1
1.1 Potential of Solar.....	4
1.2 Outline of Photovoltaic Technologies.....	9
1.3 Cadmium Telluride Photovoltaics.....	11
CHAPTER 2. HOW DO SOLAR CELLS WORK.....	14
2.1 Semiconductors.....	14
2.2 Doping.....	16
2.3 Semiconductors Under Illumination	17
2.4 p-n Junctions	21
2.5 Selectivity	24
2.6 Recombination	26
2.7 Solar Cell Characterization	31
CHAPTER 3. TRPL MEASUREMENT AND ANALYSIS	35
3.1 TRPL System.....	36
3.1.1 Oscillator.....	37
3.1.2 Optical Parametric Amplifier.....	37
3.1.3 Time-Correlated Single Photon Counting	39
3.2 Decay Fitting.....	41
3.3 TRPL Modeling.....	43
3.3.1 Fundamental Equations.....	43
3.3.2 Adding Fields.....	47
3.3.3 Simulating Biased TRPL of a Solar Cell	50
3.4 TRPL Modeling Results	51

3.5	Cell Fabrication.....	57
3.6	TRPL Measurement Results	58
3.6.1	Low and High Lifetime.....	58
3.6.2	Low and High Doping	63
3.6.3	Charge Storage Effect	70
3.7	Conclusion	72
CHAPTER 4.	N-I-P STRUCTURE TO IMPROVE VOLTAGE	74
4.1	ERE Measurement, and Potential of CdSeTe.....	74
4.2	n-i-p Structure Overview	81
4.3	Absorber Requirements	84
4.3.1	Lifetime.....	85
4.3.2	Hole Mobility.....	90
4.3.3	Diffusion Length.....	91
4.3.4	Thickness	95
4.4	p-contact Requirements	100
4.4.1	CdSeTe/p-contact Valence Band Offset	103
4.4.2	CdSeTe/p-contact Conduction Band Offset.....	108
4.4.3	Interface Recombination.....	112
4.5	n-i-p Experiments.....	112
4.5.1	NiO.....	113
4.5.2	ZnTe.....	115
CHAPTER 5.	CONCLUSIONS AND FUTURE WORK	124
5.1	Summary of Primary Conclusions.....	124
5.1.1	Field-effect Influence in TRPL.....	124
5.1.2	Strategies for Assisting TRPL Interpretation.....	125
5.1.3	n-i-p Architecture for Improved Voltages	126
5.2	Future Work.....	128
5.2.1	Repeatability of CdSeTe Deposition	129
5.2.2	Removal of Copper	130
5.2.3	Addressing Back Interface Recombination	130
5.2.4	Conclusion	132

REFERENCES	134
PUBLICATIONS.....	149
LIST OF ABBREVIATIONS.....	150

LIST OF TABLES

Table 1. Parameters for TRPL modeling.	51
Table 2. Fixed parameter values for the modeled CdSeTe absorber.	85
Table 3. Fixed parameter values for the modeled p-contact.	102

LIST OF FIGURES

Figure 1. Global CO ₂ atmospheric concentration and temperature fluctuations.	3
Figure 2. A projected path towards 100% renewable energy by 2050 in the United States.....	5
Figure 3. A visual comparison of the world’s energy use in 2015 with the potential annual (renewable) and total (nonrenewable) supply of various energy sources planetwide.	7
Figure 4. Cumulative photon absorption as a function of depth within a CdTe absorber at several photon energies.	18
Figure 5. Standardized solar irradiance spectra.	19
Figure 6. Illustration of p-n homojunction formation.	22
Figure 7. p-n homojunction under illumination.	23
Figure 8. Demonstration of perfect vs. imperfect selectivity at open circuit.....	25
Figure 9. Illustration of heterojunction between two semiconductors with different band gaps.	26
Figure 10. Illustration of absorption and the three primary recombination mechanisms.	27
Figure 11. Schematic of several types of “one-dimensional” impurities in a crystal lattice.	29
Figure 12. Example J-V curve with derived performance parameters indicated.	32
Figure 13. Example of a measured TRPL decay.	42
Figure 14. Simulated conduction band profile of CdTe absorber at a range of biases.	52
Figure 15. Extracted τ_2 lifetime vs input bulk lifetime for simulated TRPL decays at a range of biases.....	53
Figure 16. Spread of simulated lifetime vs carrier mobility for four bulk lifetime values.	55
Figure 17. TRPL of CdTe and CdSeTe/CdTe absorbers at a range of external biases.....	59
Figure 18. Schematic of steady-state photoluminescence system developed at CSU.	61
Figure 19. Biased steady-state photoluminescence of CdTe and CdSeTe/CdTe absorbers.	62
Figure 20. C-V measurements of Cu- and As-doped cells with accompanying simulated band diagrams.....	64
Figure 21. TRPL of measured and simulated cells with low absorber carrier concentration.	65
Figure 22. TRPL of measured and simulated cells with high absorber carrier concentration.	68
Figure 23. Same measurement as Figure 22a but over a much longer timescale.	70
Figure 24. Measured lifetimes of several CdSeTe and bilayer CdSeTe/CdTe absorbers with different back layers.....	77
Figure 25. ERE of several CdSeTe and CdSeTe/CdTe absorbers with different back layers.	78
Figure 26. Implied J-V for CdseTe and CdSeTe/CdTe absorbers with different back layers.	79
Figure 27. ERE of CdSeTe and CdSeTe/CdTe absorbers with Cu, As, and no doping.	80
Figure 28. Structure of n-i-p cell utilizing a CdSeTe absorber.	82
Figure 29. Band diagram of ideal n-i-p cell utilizing a CdSeTe absorber at 0 V bias.	82
Figure 30. Simulated J-V curves of n-i-p structure over a range of absorber lifetimes.....	86
Figure 31. Band diagrams at V _{OC} of n-i-p structure over a range of absorber lifetimes.....	87
Figure 32. Simulated J-V curves of n-i-p structure over a range of absorber hole mobilities.	91

Figure 33. J_{SC} as a function of hole diffusion length for simulated n-i-p structure.	92
Figure 34. Contour plots indicating simulated efficiency, V_{OC} , J_{SC} , and fill factor as a function of absorber lifetime and hole mobility.	94
Figure 35. Efficiency as a function of absorber thickness for simulated n-i-p structure.	96
Figure 36. V_{OC} as a function of absorber thickness for simulated n-i-p structure.	97
Figure 37. J_{SC} as a function of absorber thickness for simulated n-i-p structure.	98
Figure 38. Fill factor as a function of absorber thickness for simulated n-i-p structure.	99
Figure 39. Schematic illustrating band offset naming convention.	102
Figure 40. Efficiency of simulated n-i-p cell as a function of valence band offset.	103
Figure 41. Demonstration of hole barrier at low and high p-type p-contact doping.	105
Figure 42. J_{SC} and fill factor of simulated n-i-p cell as a function of valence band offset.	106
Figure 43. Demonstration of fill factor penalty with positive valence band offset.	107
Figure 44. Efficiency of simulated n-i-p cell as a function of conduction band offset.	109
Figure 45. V_{OC} of simulated n-i-p cell as a function of conduction band offset.	109
Figure 46. Demonstration of electron reflector with high p-type p-contact doping.	110
Figure 47. Structure of fabricated n-i-p cells with NiO p-contact.	114
Figure 48. J-V measurement of n-i-p cell with NiO p-contact.	114
Figure 49. Structure of fabricated n-i-p cells with ZnTe:Cu p-contact.	118
Figure 50. J-V measurement of n-i-p cell with ZnTe:Cu p-contact.	118
Figure 51. Steady-state PL before and after ZnTe:Cu deposition.	120
Figure 52. Steady-state PL before ZnTe deposition, after ZnTe deposition, and after ZnTe:Cu deposition.	121

LIST OF NOMENCLATURE

List of Parameters

Note that the units given are not necessarily SI units, but are instead those generally used in the field. In modeling and simulations, all calculations are done with SI units.

Representation	Description	Units
B	radiative recombination coefficient	$\text{cm}^3 \text{s}^{-1}$
c	speed of light	m s^{-1}
C_n / C_p	capture rate of electrons/holes	$\text{cm}^{-3} \text{s}^{-1}$
D	diffusion coefficient	$\text{cm}^2 \text{s}^{-1}$
E	field	V cm^{-1}
E_C	energy of conduction band minimum	eV
E_F	Fermi energy	eV
$E_{F,C}$	conduction band quasi-Fermi level	eV
$E_{F,V}$	valence band quasi-Fermi level	eV
E_G	band gap	eV
E_n / E_p	emission rate of electrons/holes	$\text{cm}^{-3} \text{s}^{-1}$
E_{trap}	trap energy	eV
E_V	energy of valence band maximum	eV
FF	fill factor	%
h	Planck constant	eV s
iV_{OC}	implied voltage	V
J	current density	mA cm^{-2}
j_0	recombination flux	mA cm^{-2}
J_{mp}	current density at maximum power point	mA cm^{-2}
J_{SC}	short-circuit current density	mA cm^{-2}
k	Boltzmann constant	eV K^{-1}
L	absorber thickness	μm
L_D	diffusion length	μm
L_γ	absorption depth	μm
m_e^*	electron effective mass	kg
m_h^*	hole effective mass	kg
n	electron concentration	cm^{-3}
n_0	electron concentration at equilibrium	cm^{-3}
N_A	acceptor doping density	cm^{-3}
N_C	conduction band density of states	cm^{-3}
N_D	donor doping density	cm^{-3}
n_i	intrinsic carrier concentration	cm^{-3}
N_{trap}	trap density	cm^{-3}
n_{trap}	concentration of carriers in trap	cm^{-3}
N_V	valence band density of states	cm^{-3}
p	hole concentration	cm^{-3}
p_0	hole concentration at equilibrium	cm^{-3}

P_{in}	incident solar power per unit area	mW cm^{-2}
PL	photoluminescence yield	$\text{s}^{-1} \text{cm}^{-2}$
q	elementary charge	C^*
$QFLS$	quasi-Fermi level splitting	eV
R	recombination rate	$\text{cm}^{-3} \text{s}^{-1}$
S	interface recombination velocity	cm s^{-1}
T	temperature	K
V	voltage / potential	V
V_0	built-in voltage	V
V_{mp}	voltage at maximum power point	V
V_{OC}	open-circuit voltage	V
$V_{OC,ideal}$	ideal voltage, maximum attainable of material	V
V_T	thermal voltage	V
v_{th}	thermal velocity	cm s^{-1}
W	depletion region width	μm
W_n	depletion width in n-type material in p-n junction	μm
W_p	depletion width in p-type material in p-n junction	μm
α	absorption coefficient	cm^{-1}
ϵ	permittivity	$\text{C V}^{-1} \text{m}^{-1}$ *
ϵ_0	permittivity of free space	$\text{C V}^{-1} \text{m}^{-1}$ *
η	conversion efficiency	$\%$
κ	relative permittivity	unitless
λ	photon wavelength	nm
μ	mobility	$\text{cm}^2 \text{V}^{-1} \text{s}^{-1}$
ρ	generic carrier concentration (electrons or holes)	cm^{-3}
σ	trap cross section	cm^2
τ	lifetime	ns
χ	electron affinity	eV

*SI units indicated; in practice Coulombs never appear, as the relation $\frac{\text{eV}}{q} = V$ is used, rendering q quasi-unitless.

CHAPTER 1. INTRODUCTION

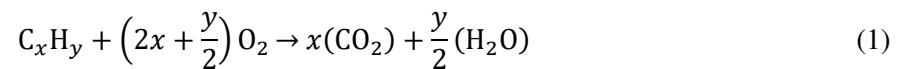
Since the industrial revolution, humanity's energy consumption has grown nearly exponentially [1]. This increased energy utilization has been powered almost exclusively through the burning of fossil fuels, first primarily coal (~1860-1940), followed by oil (~1940-2000) and more recently natural gas. This is due to a similarly exponential increase in global population in addition to increased energy use per capita as most countries industrialized and economic standards of living improved.

Unfortunately, the burning of fossil fuels for energy has several serious consequences which make it thoroughly unsustainable. The simplest, inescapable problem is that supply is finite. Fossil fuels are the result of accumulated dead organic matter being compressed by the weight of the Earth's crust for millions of years [2], creating materials which are very energy-dense. As it takes millions of years for these substances to form, the rate of replenishment is far outpaced by the rate of extraction. Fossil fuels therefore fundamentally could never be relied on as a long-term, stable energy solution – their continued use pushes humanity towards an inevitable insurmountable problem.

There are many, many other issues, however. The extraction, transportation, and processing of fossil fuels comes with an abundance of serious negative environmental consequences. Mountaintop removal and strip mining of coal are incredibly destructive to the natural landscape. Oil spills by tankers and pipelines are unavoidable and cause vast and enduring damage to ecosystems and communities, particularly when they occur in water. Oil refineries are major sources of pollution. Hydraulic fracturing is particularly problematic for causing surface and groundwater pollution as well as for very high water consumption.

Combustion of fossil fuels emits nitric and sulfuric acids into the atmosphere where they return to the surface in the form of acid rain. Particulate matter emissions cause respiratory illness and premature death – one estimate attributes 8.7 million deaths in 2018 [3] (one in five) to air pollution from combustion of fossil fuels.

Above all else, the most serious problem with fossil fuels is that they bring about climate change. Combustion of hydrocarbons produces carbon dioxide by the simple chemical reaction:



This process releases energy as heat, and through conservation of mass, carbon dioxide *must* be a reaction product. Carbon dioxide is a greenhouse gas, meaning it is very effective in absorbing and transmitting energy within the thermal infrared range. Accumulation of greenhouse gasses in the atmosphere therefore allows the atmosphere to retain more heat, raising the temperature of the planet's surface. There is thus a strong historic correlation between temperature and atmospheric carbon dioxide concentration [4] (see Figure 1), both in the planet's distant past and since the industrial revolution.

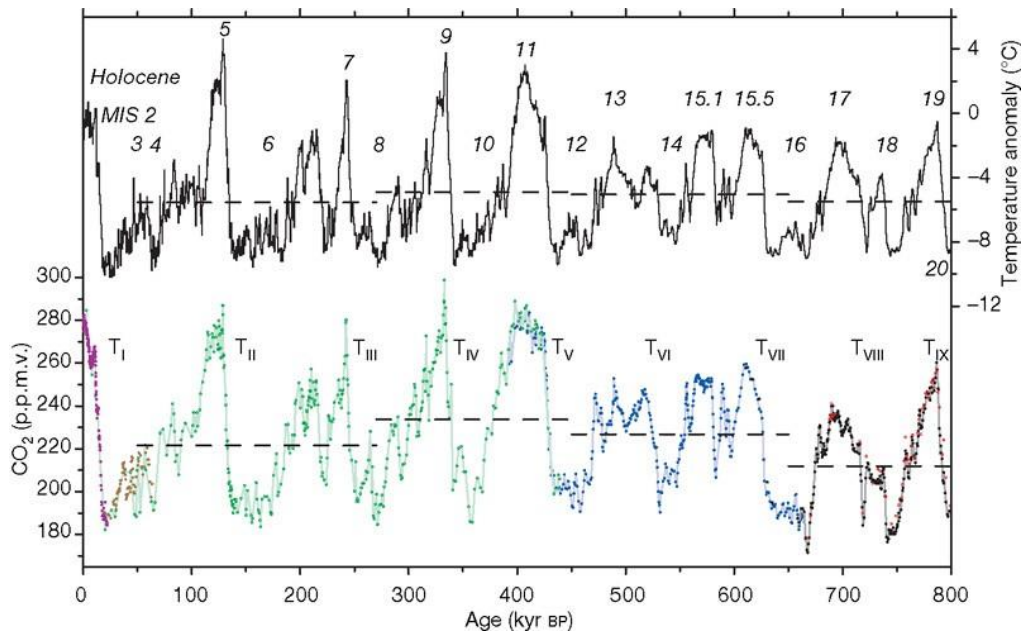


Figure 1. Global CO₂ atmospheric concentration and temperature fluctuations for the last 800,000 years as determined from measurements on ice cores in Antarctica. Global temperature tracks very closely with atmospheric CO₂ concentration. Taken from [4].

Elevated global temperatures bring about a host of changes which would ultimately be catastrophic for human civilization. The melting of polar ice sheets would cause a significant rise in global sea levels [5], destroying coastal settlements and displacing potentially billions of people. Associated desalinization of the world's oceans and reduction in their pH due to absorption of CO₂ from the atmosphere [1] would decimate marine life and disrupt oceanic currents causing dramatic changes in climate and weather patterns over large areas of the planet. These climactic changes would lead to increases in the frequency and severity of major storms and weather events (as has already been observed) [6], as well as proliferate climate-sensitive diseases such as malaria and dengue fever [7]. Rising temperature and less stable weather will lead to longer and hotter heatwaves, increasing the prevalence of wildfires and drought. Scarcity

of resources and displacement due to drought and rising seas will engender conflict and mass migration, leading to widespread political destabilization.

It must be noted that hydrocarbon consumption also exacerbates inequality [8], [9]. The hazardous work of fossil fuel extraction and processing is done by the world's poorest to supply and enrich in large part the world's wealthiest. As such the poor are disproportionately far more likely to suffer negative effects from exposure to pollution, industrial accidents, etc. On a global scale, the impacts of climate change have already been and will continue to be experienced most by the world's poorest, who bear disproportionately miniscule responsibility for the situation.

The burning of fossil fuels is not the only contributor to climate change. Agriculture, particularly animal agriculture, is responsible for the emission of large amounts of potent greenhouse gasses like nitrous oxides and methane. Deforestation, in large part caused by the demands of animal agriculture in particular, reduces the amount of carbon-absorbing biomass on the planet, increasing the concentration of CO₂ in the atmosphere. Industrial processes such as the production of cement, steel, and chemicals produce greenhouse gasses [10]. Extracting and transporting fossil fuels also directly releases greenhouse gasses through fugitive emissions. Solving climate change will involve addressing and rectifying *all* of these problems, though transitioning to carbon-free, renewable electrical energy generation is arguably the most important.

1.1 Potential of Solar

Crucial for halting and reversing climate change is transitioning entirely away from fossil fuels for energy generation as soon as possible. Thankfully, there are many alternatives readily available, including solar, wind, hydroelectric, nuclear fission, and other more exotic

technologies like geothermal, tidal, ocean thermal energy conversion, and others. Proposed sustainable, carbon-free energy generation mixes tend to rely heavily on wind and solar energy, with other renewables in smaller roles [11] (see Figure 2). Wind and solar are both widely implementable and complement each other well, with wind often blowing when there is less sunlight. Smaller-scale niche technologies should be applied where they are feasible. While there is no single, universal solution – all generation strategies are useful in various applications – solar energy will be particularly important in the immediate and long-term future.

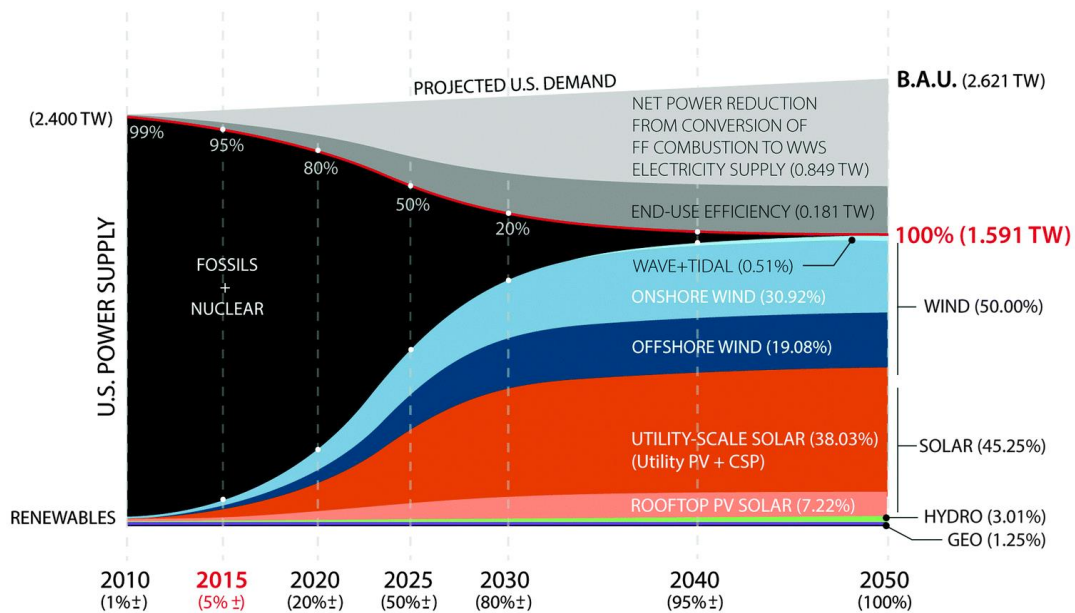


Figure 2. A projected path towards 100% renewable energy by 2050 in the United States. This model is typical, incorporating demand reduction with generation from a variety of renewable sources, with wind and solar providing the bulk of electricity production. Taken from [11].

“Solar energy” can refer to several mostly unrelated technologies. Conversion of sunlight directly into electricity using semiconductors is called **photovoltaics (PV)**. Solar thermal plants and solar updraft towers harness the sun’s energy by heating fluids and exploiting the chimney effect, respectively, but both ultimately rely on spinning turbines and thus are fundamentally

very different from PV. As neither of these technologies has seen deployment and adoption anywhere near the scale of PV, from here on “solar energy” will exclusively refer to photovoltaics. Solar PV is unique among energy generation sources in that turbines are not necessary and there are no moving parts. This offers immense scalability, with installation potential ranging from massive solar power stations generating hundreds or even thousands of megawatts down to highly localized applications (a solar-powered calculator is an extreme example). They generate no noise or pollution, so they can be deployed anywhere, even in densely populated areas.

Solar energy has many highly desirable attributes, but perhaps the most significant is capacity. The amount of capturable solar radiation incident on the planet each year is orders of magnitude larger than the resource availability of all other renewable sources, as well as the total energy potential of all fossil fuels and nuclear [12], [13]. Figure 3 highlights this fact, demonstrating the potential of various energy technologies alongside global energy consumption in 2015. Total reserves are indicated for nonrenewable sources and annual capacity is represented for renewables. The potential of solar dwarfs not only humanity’s energy needs, but also the potential of all other sources. In fact, assuming an average of 1 kW/m^2 solar irradiance [14] over half of earth’s $5 \times 10^{14} \text{ m}^2$ area [15], in 40 minutes more solar energy has reached the Earth than all $6 \times 10^{20} \text{ J}$ of energy consumed by humanity in 2020 [16]. This vast energy source is also effectively eternal, contingent only on the continued fusion of $1.5 \times 10^{30} \text{ kg}$ of hydrogen into helium [17] within our sun’s main sequence, estimated to continue for another five billion years [18].

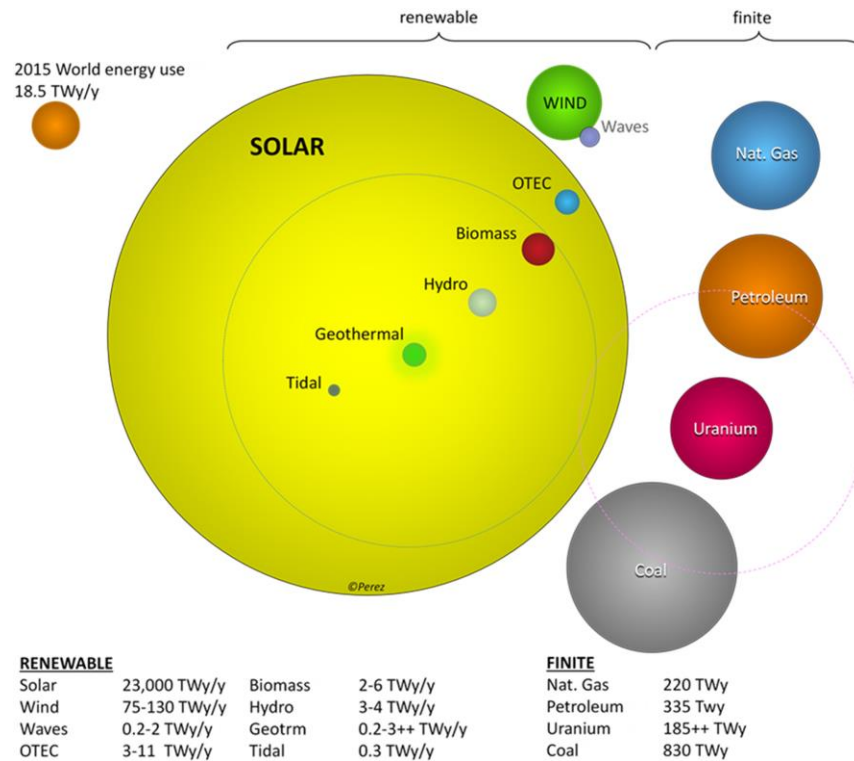


Figure 3. A visual comparison of the world’s energy use in 2015 with the potential annual (renewable) and total (nonrenewable) supply of various energy sources planetwide. The potential of solar energy far exceeds all other sources, as well as the world’s energy consumption. Taken from [13].

These reasons alone make solar energy very appealing, and it could be argued (this author certainly would) that the externalities of fossil fuel consumption are so great that almost no cost is too high for widespread supplantation of fossil fuels with solar and other renewable sources. However, renewables’ very large reduction in cost and increase in adoption over the past decade have made this argument unnecessary. Not only does solar PV provide a pathway towards sustainable energy generation for the near and distant future, utility-scale solar PV is already cost-competitive with fossil fuels. In 2020, the unsubsidized levelized cost of energy (LCOE) of utility scale PV was \$29 to \$42 per MWh, compared to \$44 to \$73 for gas combined cycle, and

\$65 to \$159 for coal [19]. And while the cost of fossil fuels is particularly volatile and generally increasing, the cost of PV continues to steadily fall each year.

There is another perspective which should be addressed, beyond science and economics. The point of a green energy transition is to correct past mistakes and build a better world for ourselves. It is not enough to expect that technology alone will accomplish this. Humanity's addiction to fossil fuels has created extreme concentrations of wealth and political influence, and has empowered dictators and autocrats the world over as market demands compel capitalist democracies to turn a blind eye, fomenting exploitation, coercion, and inequality. It is vitally important that these same systems of injustice are not allowed to survive the energy transition, or to simply be replaced by new "green" ones. Such an arrangement would be just as unsustainable and unacceptable as the present circumstances. The transition to a sustainable existence in harmony with our planet must come from the bottom up, not be dictated from above; we *all* have a stake in our future, and our society must serve *all* of us.

Solar photovoltaics is certainly entirely compatible with such a vision for the future, but it can just as easily perpetuate the same systemic pathologies which currently exist if we are not careful, particularly concerning extraction of the required rare materials and ownership of energy production. Regardless, given all of its advantages it is clear that PV will be of major consequence in the near- and long-term future. Although it is not *sufficient*, sustainable technology is *necessary* to ensure a successful transition from fossil fuels, so continued research and improvement is essential.

1.2 Outline of Photovoltaic Technologies

Solar photovoltaic technologies are characterized by their light-absorbing material, called the **absorber**. Many absorbers exist, and different absorber technologies have unique challenges, existing at different stages of maturity achieving different levels of performance at different costs. This section will briefly describe the most significant.

Solar cells made of silicon have existed since the 1950s [20], and silicon has been the dominant photovoltaic technology ever since. Today, silicon represents ~95% of global photovoltaic production [21]. Panels are made by arranging wafers sliced from solid ingots of either single crystals or polycrystalline stock. A steady increase in the adoption of polycrystalline silicon up to a significant majority of production in 2016 has seen a sharp reversal as monocrystalline silicon has again become dominant, representing ~80% of total PV production in 2020 [21] as a consequence of cost reductions in ingot fabrication and wafer slicing techniques [22]. Many decades of development have resulted in typical module efficiencies around 23% in 2020 [22], not far from the Shockley-Queisser limit for this material (the theoretical maximum achievable performance). Silicon benefits from a substantial economy of scale and large investments in material research and process optimization, both a product of the larger semiconductor and electronics industries.

The next largest group are so-called “thin-film” PV materials. This is a loose term which can refer to many wholly unrelated technologies, but for practical purposes it essentially consists of cadmium telluride (~4%) and CIGS (~1%) [21], respectively belonging to the chalcogenide (“II-VI”) and chalcopyrite (“I-III-VI”) semiconductor classes. Cadmium telluride (CdTe) is the subject of this dissertation, and will be elaborated on in the next section. The (Ag,Cu)(In,Ga)(S,Se)₂ alloys commonly collectively referred to as CIGS are well-suited for

photovoltaic applications, and a record 23.4% small-area device conversion efficiency has been attained [23], higher than CdTe. Versatility in form factor implementation is high, and deposition on metal foils or polymers allows fabrication of lightweight and flexible modules at relatively low cost. However, scalability represents a major problem, and the efficiency gap between small-area research cells and commercial modules is greater than with silicon or CdTe.

All other technologies combined represent less than one percent of the global PV market share, but a few nevertheless significant ones will be briefly discussed.

Gallium arsenide (and other so called “III-V” materials) is a well-established, high-performing technology with very small market penetration. III-V’s claim the world record single-junction terrestrial conversion efficiency of 29.1% [24], as well as the record for highest-performing photovoltaic device, a six-junction cell attaining 47.1% efficiency under 143-sun concentration [25]. Gallium arsenide alloys are particularly well suited for concentrator and multijunction applications, and can be thin, flexible, and durable. However, complicated, lengthy fabrication methods requiring a multitude of low-throughput, labor-intensive processes with costly materials make gallium arsenide modules orders of magnitude more expensive than silicon [22]. For this reason, this technology has only seen applications in circumstances where energy density is paramount and cost is no issue; historically this has mainly meant adoption for space-based photovoltaics (also due to exceptional gamma radiation resistance [26]) and military applications.

Perovskites are a class of thin-film photovoltaics which have seen astronomical improvements in conversion efficiency over a very short time, from 9.7% in 2012 [27] to 25.2% in 2021 [28]. They are characterized by strong absorption and high defect tolerance [22]. The

ease with which perovskite bandgaps can be tuned over a large range [29] make them particularly suitable for high-efficiency tandem structures, and allow flexibility which will likely be particularly valuable in future PV implementation schemes. However, perovskites currently exist only in research-scale and prototype form, with no commercial production. The technology has had serious stability and longevity issues, scalability is questionable, lead toxicity is a concern, and overall large-scale manufacturing feasibility has not yet been demonstrated [22]. While perovskites may prove invaluable in the medium to long term, they have yet to contribute to the transition to renewable energy in the short term.

There exist other niche technologies in varying stages of maturity and commercialization, including organic PV, quantum dots, amorphous silicon, kesterites, and others.

1.3 Cadmium Telluride Photovoltaics

Positioned between proven, reliable, high-performing, yet relatively stagnant silicon with little room for improvement, and auspicious yet unproven technologies like perovskites, cadmium telluride (CdTe) represents perhaps the most promising technology for the near future. CdTe PV has the second-largest production volume behind silicon, accounting for ~4% of global market share in 2020 [21]. Like silicon, it has many decades of development history and has demonstrated reliability, scalability, and high manufacturing capacity.

While its comparatively small adoption may seem to indicate serious deficiencies, CdTe in fact has numerous significant advantages over silicon as a photovoltaic material. CdTe's 1.5-eV direct bandgap is far better at absorbing solar photons than silicon's 1.1-eV indirect bandgap. Up to 99% of absorbable solar spectrum photons are absorbed within 2 μm of CdTe film, a hundredfold improvement over silicon [30]. This confers a number of manufacturing advantages.

Far less material is needed, reducing costs. Fabrication of polycrystalline thin-film modules is much simpler than monocrystalline silicon. A single assembly line can produce an entire CdTe panel in ~3 hours, whereas a typical silicon panel takes several days over multiple facilities. All of this translates into significant capital and operating cost reductions, as well as reduced energy consumption during manufacturing. CdTe has the shortest energy payback time of all PV technologies, generally on the order of *months*, with the lowest carbon footprint [31], [32]. Life-cycle water usage is lower in CdTe than most other electricity generation sources [33], and lower than silicon [34]. Silicon processing requires hydrofluoric acid and produces highly toxic silicon tetrachloride, while a CdTe module's toxicity potential over its lifespan is negligible [35]. The effect of performance reduction at higher temperature is smaller with larger bandgap materials [36], so CdTe is better suited than silicon for hot climates. Longevity of CdTe modules is generally better than their silicon counterparts.

Despite all of its advantages, CdTe suffers from comparatively low conversion efficiency. Small-area research cells have attained a record efficiency of only 22.1% [37], although it is important to note that commercial modules are not far behind – First Solar's Series 6 modules attain 18.3% efficiency [38]. For decades polycrystalline CdTe has suffered from low open-circuit voltage (V_{OC}) relative to its band gap [39]. While short-circuit current density has come very close to its Shockley-Queisser limit with fill factor not far behind [40], open-circuit voltage losses have stubbornly persisted. Reducing the voltage deficit is perhaps the single highest priority research focus in the field, and several concurrent strategies are being pursued. These include trying to achieve higher carrier concentration (notably with group V elements), optimization of p-n junction interface and band alignment, incorporation of electron reflectors, back interface passivation, and improvement of carrier lifetime [22].

Single-crystal CdTe cells have in general demonstrated higher V_{OC} , with multiple published reports of examples breaking the 900-mV barrier [41]–[43]. A very small number of highly unconventional single-crystal CdTe cells fabricated specifically for this purpose have demonstrated open-circuit voltage greater than 1 Volt, one employing phosphorous doping [39] and the other utilizing n-type CdTe sandwiched between MgCdTe buffer layers [44]. While these results prove that this significant milestone is possible to achieve with this material, single-crystal CdTe cells are difficult and expensive to produce and have not demonstrated widespread adoption feasibility. The challenge remains to realize this voltage improvement in polycrystalline thin-film cells, whose low cost, ease and speed of manufacture, scalability, low energy payback time, and versatility constitute CdTe's significant strengths.

Despite these challenges, there is reason for optimism. CdTe has already proven its feasibility, currently demonstrating very low cost at large and rapidly increasing production volumes. Its performance deficit in relation to silicon is a problem of unrealized potential, not inherent weakness of the material. Silicon has benefitted from much more investment in research and development spanning many decades, as well as a robust and well-established supply chain and processing infrastructure. As CdTe production continues to scale up costs will certainly fall even farther, and as investment increases and research progresses efficiencies will certainly increase. For these reasons, CdTe may be the most promising PV technology in the near term, and as such it is a particularly valuable area of research.

CHAPTER 2. HOW DO SOLAR CELLS WORK

At its most basic, a photovoltaic device requires two things. The first is a way to transform sunlight into free electrons with some degree of permanence. The second is a way to passively move these electrons in the same direction and out of the device, creating a current external to the device which can be used to do work.

2.1 Semiconductors

Semiconductors can fulfill both of these requirements, and are thus fundamental to photovoltaics. Semiconductor materials are usually highly-structured repeating crystal lattices. Electrons orbiting the nucleus of an atom are bound particles, and as such their allowed energy states are quantized. Electrons orbiting isolated atoms have few, largely-spaced energy states. In a grouping of a large number of identical atoms with small interatomic distances, such as in a crystal solid, overlapping of atomic orbitals causes these few energy levels to finely split into as many energy values as there are atoms, forming a near-continuum of energy states [36]. Semiconductors uniquely have a substantial forbidden region where no discrete electron energy states exist, a kind of “leftover” energy space not covered by overlapping orbitals. The continuum of low-energy states below the forbidden region is called the **valence band**, and the group of states with energy above the forbidden region is called the **conduction band**. The difference in energy between the highest energy state in the valence band (the valence band maximum, E_V) and the lowest energy state in the conduction band (the conduction band minimum, E_C) is called the **band gap** E_G of the semiconductor. Valence band energy states are almost entirely filled at all times, so electrons, being subject to the Pauli exclusion principle, are not free to move. Conversely, as the conduction band energy states are sparsely populated,

electrons in the conduction band are free to move about the semiconductor lattice; the band gap therefore describes the energy required to liberate a valence electron and make it mobile. For comparison, *conductors* do not have a region of forbidden energy states, and in *insulators* this region is so large as to be essentially uncrossable.

When an electron absorbs sufficient energy (from a photon, for instance) and enters the conduction band, it leaves behind a vacancy in the valence band. Neighboring electrons are free to enter this vacancy, which moves the vacancy to the next atom in the lattice, and so on. Therefore, this valence band vacancy itself can be considered as a quasiparticle which is free to move about the crystal lattice. This positively-charged quasiparticle is called a **hole**, analogous to the negatively-charged **electron** in the conduction band. Absorption of a photon with sufficient energy thus creates an electron-hole pair within the semiconductor, and management of these charge carriers is essential for solar cell functionality.

A useful concept in semiconductors is the **Fermi level**; this is an energy level E_F below which, at absolute zero, all energy states are occupied by electrons and above which, no states are. Above 0 K, there is a symmetrical smearing of the distribution such that some electrons can exist above E_F and an equal number of holes can exist below it. This smearing is described by the Fermi-Dirac distribution function [36]:

$$f_e(E) = \frac{1}{\exp\left(\frac{E - E_F}{kT}\right) + 1} \quad (2)$$

which expresses the probability of finding an electron at energy E . k is the Boltzmann constant and T is the temperature. The balance of electrons and holes on either side of E_F is symmetric; therefore, the Fermi level represents a hypothetical energy level where there is equal probability

of occupation by electrons and holes [45]. In a semiconductor, E_F almost always lies within the forbidden region, so while E_F represents energy, it is *not* an occupiable energy *state*.

The concentration of electrons per unit volume n in the conduction band is

$$n = N_C e^{\frac{(E_F - E_C)}{kT}} \quad (3)$$

Similarly, the concentration of holes p in the valence band is

$$p = N_V e^{\frac{(E_V - E_F)}{kT}} \quad (4)$$

where N_C and N_V are the density of states in the conduction and valence bands, respectively, and E_C and E_V are the conduction band minimum and valence band maximum [46]. N_C and N_V are defined as [36]:

$$N_C = 2 \left(\frac{2\pi m_e^* kT}{h^2} \right)^{\frac{3}{2}} \quad (5)$$

$$N_V = 2 \left(\frac{2\pi m_h^* kT}{h^2} \right)^{\frac{3}{2}} \quad (6)$$

where m_e^* and m_h^* are the effective masses of electrons and holes and h is the Planck constant.

2.2 Doping

Doping is the process by which impurities are added to the semiconductor lattice to alter its electronic properties. For example, phosphorous has 5 valence electrons compared to silicon's 4, and boron has 3. Substitutional phosphorous atoms in a silicon lattice will therefore add free electrons to the material, while boron atoms will remove electrons, equivalent to *adding* holes. Materials which have been doped to contain extra electrons and holes are called **n-type** and **p-type**, respectively, and the dopant atoms are accordingly called **donors** and **acceptors**. The concentrations by volume of donors and acceptors are represented as N_D and N_A . Note that n-

and p-type semiconductors still have net *neutral* charge, as the total number of electrons and protons are equal.

In an intrinsic (undoped) semiconductor, the condition $n = p$ along with equations (3) and (4) yields the following relation for the Fermi level:

$$E_F = \frac{E_C + E_V}{2} + \frac{kT}{2} \ln \left(\frac{N_V}{N_C} \right) \quad (7)$$

Typically the density of states of the bands are comparable, $N_V \approx N_C$; therefore, the Fermi level of an intrinsic semiconductor is essentially in the middle of the bandgap. In a sufficiently n-type material, the approximate condition $n \approx N_D \gg p$ leads to

$$E_F = E_C + kT \ln \left(\frac{N_D}{N_C} \right) \quad (8)$$

while in a p-type material, the condition $p \approx N_A \gg n$ leads to

$$E_F = E_V - kT \ln \left(\frac{N_A}{N_V} \right) \quad (9)$$

Therefore, as the material becomes more n-type, E_F approaches E_C , while as the material becomes more p-type, E_F approaches E_V [36]. In so-called “degenerately-doped” semiconductors, doping is so great that E_F can exist above E_C or below E_V , though in these situations the effective density of states approximation used in equations (8) and (9) no longer applies.

2.3 Semiconductors Under Illumination

The absorption of photons within a semiconductor is governed by the Beer-Lambert law, which yields an exponential relation [47]:

$$I(x) = I_0 e^{-\alpha(\lambda)x} \quad (10)$$

where $I(x)$ represents the transmitted optical intensity at depth x within the material, I_0 is the initial intensity, and $\alpha(\lambda)$ is the absorption coefficient of the semiconductor at photon wavelength λ . An associated parameter is the absorption depth L_γ :

$$L_\gamma(\lambda) = \frac{1}{\alpha(\lambda)} \quad (11)$$

which represents the penetration depth at which the optical intensity is $\frac{I_0}{e}$. As an example, Figure 4 shows the cumulative absorption as a function of depth in CdTe at several discrete photon energies; absorption coefficients are taken from [48]. The vast majority of photons with wavelength <700 nm are absorbed within $2 \mu\text{m}$ of material, and the rapid reduction of absorptance as photon wavelength approaches CdTe's ~ 830 -nm bandgap is clear. The AM1.5 solar insolation standard is shown in Figure 5. The terrestrial spectrum is largely concentrated in the visible and near-infrared regions, so CdTe is well-positioned to absorb substantial amounts of solar radiation with very thin layers.

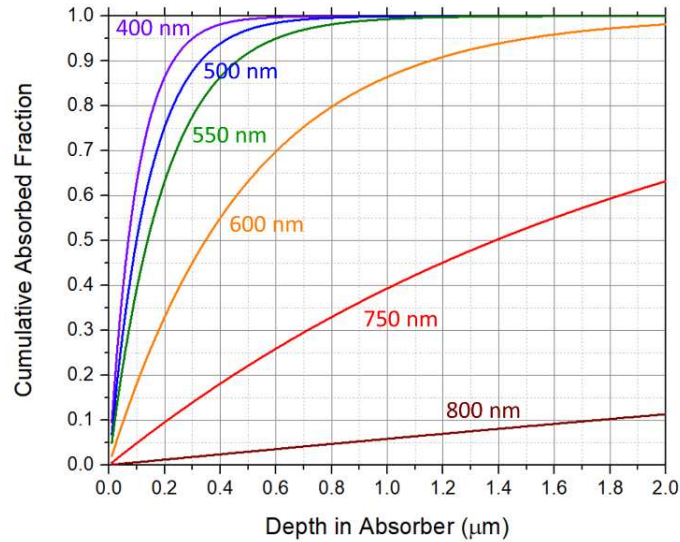


Figure 4. Cumulative photon absorption as a function of depth within a CdTe absorber at several photon energies (wavelengths indicated). For photon wavelengths <700 nm, $2 \mu\text{m}$ is enough to

absorb virtually all photons. Rapid reduction in absorptance is visible as CdTe's ~830-nm bandgap is approached.

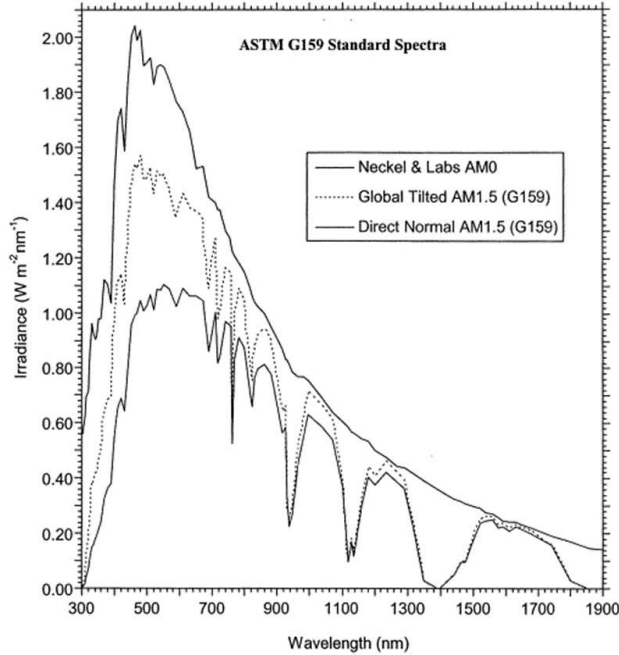


Figure 5. Standardized solar irradiance spectra. AM0 is the solar spectrum above the atmosphere. AM1.5 is the terrestrial standard of transmission through 1.5 atmospheres, representing the overall yearly average insolation at mid-latitudes. The dips are due to optical absorption by molecules in the atmosphere, chiefly water vapor. The two AM1.5 spectra shown correspond to panels with normal orientation and panels with 37° tilt towards the sun. Taken from [49].

Under illumination, electron-hole pairs are created with energy separation equal to the energy of the absorbed photons. Solar radiation, as with a black body at 5800 K, has a broad spectrum (see Figure 5), so many of the absorbed photons have energy greater than E_G . The photogenerated carriers are thus excited to some higher energy within their respective bands. Over a very short timescale of $\sim 10^{-12}$ s [36] these carriers lose energy until they reach the band edges (valence band maximum and conduction band minimum), a process called **thermalization**. At the band edge, they are metastable.

Under illumination, the conditions of equations (3) and (4) no longer hold; there are greater numbers of electrons and holes in a semiconductor than the equilibrium concentration, $np > N_D N_A$. Therefore, the Fermi distribution of electrons must be closer to the conduction band than its distribution in the dark, and the distribution of holes must likewise be closer to the valence band. These conditions are impossible to satisfy simultaneously with a single Fermi level. Therefore, there are in fact *two* so-called **quasi-Fermi levels**, one which describes the occupation of electrons in the conduction band $E_{F,C}$, and the other describing the occupation of holes in the valence band $E_{F,V}$:

$$E_{F,C} = E_C + kT \ln\left(\frac{n}{N_C}\right), \text{ and conversely } n = N_C e^{\frac{(E_{F,C} - E_C)}{kT}} \quad (12), (13)$$

$$E_{F,V} = E_V - kT \ln\left(\frac{p}{N_V}\right), \text{ and conversely } p = N_V e^{\frac{(E_V - E_{F,V})}{kT}} \quad (14), (15)$$

This duality in fact always exists, it is simply the case that in the dark, $E_{F,C} = E_{F,V}$. Under illumination, these quasi-Fermi levels separate, leading to so-called **quasi-Fermi level splitting (QFLS)**, the magnitude of which is [50]:

$$QFLS = E_{F,C} - E_{F,V} = E_G + kT \ln\left(\frac{np}{N_C N_V}\right) \quad (16)$$

The quasi-Fermi levels $E_{F,C}$ and $E_{F,V}$ are equivalent to the electrochemical potential of electrons and holes. As will be discussed in Chapter 4, QFLS is an extremely important characteristic. The greater the difference in electrochemical potential, the more work can be done by a photovoltaic device. As QFLS is proportional to np , increasing carrier concentration by doping increases QFLS, as does increasing the amount of photogenerated carriers with higher illumination intensity.

2.4 p-n Junctions

A semiconductor material, whether n-type, p-type, or intrinsic, is capable of generating free carriers through the absorption of photons. However, performing work requires extraction of these carriers out of the material. The most common way of accomplishing this in photovoltaic devices is through a p-n junction.

When an n-type and a p-type semiconductor are bonded to each other, the excess electrons and holes diffuse in opposite directions, leaving behind charged ions in the crystal lattice. The presence of positive ions in the n-type side and negative ions in the p-type side creates a built-in electric field at the p-n junction. This field influences the motion of unbound electrons and holes, pushing them in opposite directions. The resulting potential difference which forms between the contacts of the cell is [51]:

$$V_0 = \frac{kT}{q} \ln \left(\frac{N_A N_D}{n_i^2} \right) \quad (17)$$

where n_i is the intrinsic carrier concentration, which is an inherent property of a particular semiconductor at a given temperature. In an undoped semiconductor at equilibrium, every conduction band electron originates from the valence band, so:

$$n_i^2 = n_0 p_0 \quad (18)$$

where n_0 and p_0 represent the carrier concentrations at equilibrium.

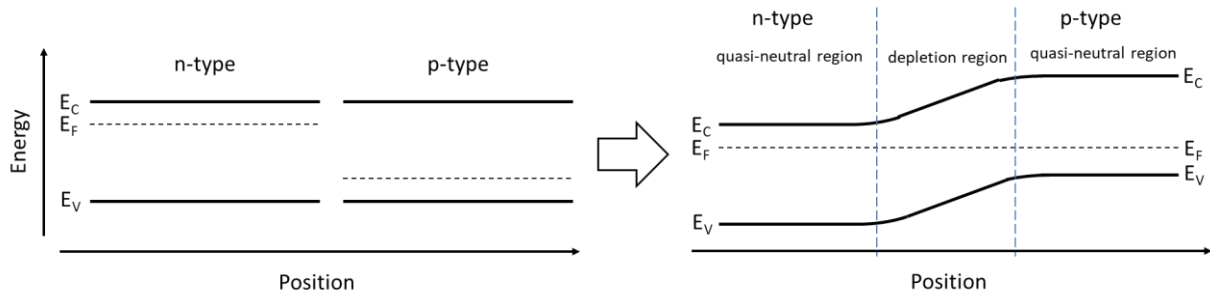


Figure 6. Illustration of p-n homojunction formation. In unilluminated thermodynamic equilibrium, the single Fermi level must be constant throughout the cell, forcing the bands to bend to compensate, creating fields.

This p-n junction behavior can be illustrated with the electronic band structure model. Figure 6 illustrates p-n junction formation in a homojunction (both n- and p-type materials are the same semiconductor). A system in thermal equilibrium can only have a single Fermi level ($E_{F,C} = E_{F,V}$ everywhere); no current can flow if there is no energy source. When n- and p-type materials are bonded, the band edges of both materials must bend to compensate. A slope in the bands signifies a field – a change in potential over a distance. When illuminated, the quasi-Fermi levels separate following this field, shown in Figure 7. Photogenerated electrons move from low potential to high potential in the conduction band following the positive gradient of $E_{F,C}$, and holes move in the opposite direction in the valence band; as shown in Figure 7, electrons are swept into the n-type material and holes to the p-type material. The field-containing region of bent bands surrounding the junction is called the **depletion region**, so called because all mobile charge carriers here are swept away by the fields. Far from the junction, the bands are flat; these areas of no field are called **quasi-neutral regions**, in which carriers move only by diffusion. The width of the depletion region is given by [51]:

$$W = \sqrt{\frac{2\epsilon}{q} V_0 \left(\frac{1}{N_A} + \frac{1}{N_D} \right)} \quad (19)$$

where ϵ is the permittivity of the semiconductor, often denoted $\epsilon = \kappa\epsilon_0$ where κ is the relative permittivity of the material and ϵ_0 is the permittivity of free space. The relative widths of the depleted region within in the n- and p-type materials are:

$$W_n = W \frac{N_A}{N_A + N_D} \quad (20)$$

$$W_p = W \frac{N_D}{N_A + N_D} \quad (21)$$

Therefore, if $N_D \gg N_A$, the p-type material will contain a much larger portion of the depletion width, and vice versa. Depending on the amount of doping and the thickness of the layers, there may be no quasi-neutral regions; in this circumstance the cell is designated “fully depleted.”

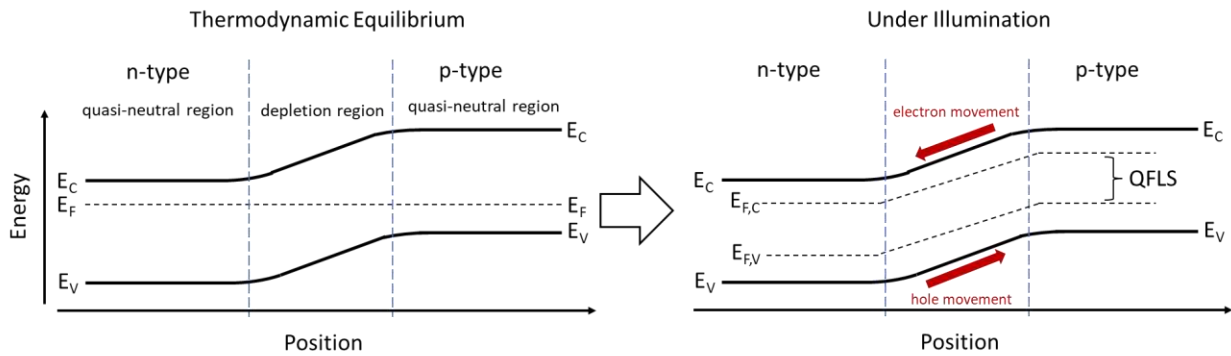


Figure 7. Under illumination, the single Fermi level splits into separate quasi-Fermi levels for each band. The gradients of these Fermi levels drive the motion of electrons and holes in opposite directions. Note that this symbolic representation assumes uniform generation of carriers throughout the cell. This representation is at short circuit.

2.5 Selectivity

As will be discussed in depth in Chapter 4, p-n junctions are not the only way to extract carriers. **Selectivity** describes a structure's ability to ensure that only carriers of the correct type can reach each contact. A perfectly selective electron contact will facilitate the flow of electrons while blocking the hole current. Perfect selectivity of *both* contacts is needed to attain maximum performance. Ultimately, this requires differences in conductivity: part of the cell must be a material which preferentially conducts electrons, and another part must be a material which preferentially conducts holes. Selectivity S can be expressed quantitatively using the partial specific resistivities of each carrier type for each selective layer [52]:

$$S = 1 - \frac{r_h^h}{r_e^h + r_h^h} - \frac{r_e^e}{r_e^e + r_h^e} \quad (22)$$

where r_e^h is the partial resistivity to electrons of the hole-selective material, for example. This expression of selectivity is of little empirical utility as it not based on any easily-measurable quantities, but it is useful from a modeling and conceptual perspective. Selectivity directly relates QFLS and the cell's voltage at open circuit, V_{OC} (introduced in Section 2.7):

$$V_{OC} = S \times \frac{QFLS}{q} \quad (23)$$

where q is the elementary charge. This is illustrated with band diagrams of structures with low and high selectivity, shown in Figure 8. Quasi-Fermi levels must collapse to a single Fermi level at the electrodes of the cell, as conductors and degenerate semiconductors do not support two Fermi levels. How this collapse is distributed is dependent on the partial specific resistivities of each carrier type in the selective layers.

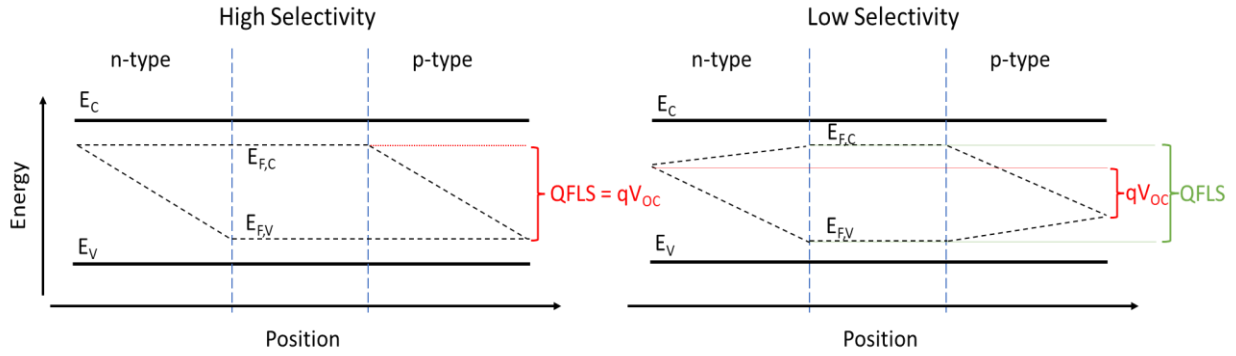


Figure 8. Demonstration of perfect vs. imperfect selectivity at open circuit. With perfect selectivity, $V_{OC} = \frac{QFLS}{q}$. With imperfect selectivity, the difference in chemical potential at the contacts is less than the QFLS in the bulk, so $V_{OC} < \frac{QFLS}{q}$. This representation is at open circuit.

In a p-n homojunction, the n-type material conducts electrons and repels holes due to the fields which form; the p-type material does the opposite. There are other ways to promote selectivity, however. Abrupt energy barriers which can form at heterojunctions between different semiconductor materials with different bandgaps can effectively block one type of carrier from passing (example in Figure 9). In the simplest case, materials with vastly different mobilities for each carrier type can induce selectivity [50]. In real cells there is a significant reason, discussed in the next section, why this simplest approach is unlikely to ever work, but it is important to keep in mind that p-n junctions specifically are not what allow solar cells to function – it is instead asymmetric conductivity producing selectivity. Passive separation and extraction of photogenerated carriers is what allows a photovoltaic device to do work. The performance of photovoltaic cells ultimately depends on the efficacy of this process, and there are many device and material parameters which describe different aspects of it.

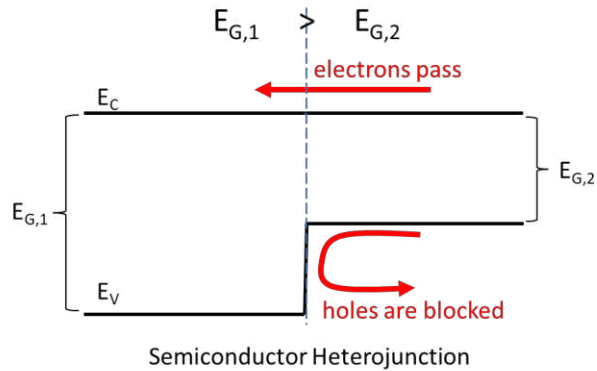


Figure 9. Illustration of heterojunction between two semiconductors with different band gaps. This particular example is electron-selective: the band alignment is such that electrons are free to conduct through the junction while holes are blocked.

2.6 Recombination

Photoexcited carriers at the band edges in a semiconductor are metastable. They will only exist in this state for a finite amount of time, the average of which is denoted the **lifetime** of the material. Electrons in the conduction band will eventually lose their energy and cross the band gap back down to the valence band, eliminating an electron and a hole in the process. This electron-hole annihilation process is called **recombination**, and there are several pathways by which this can occur [53], [54]. All discussed pathways are shown in Figure 10.

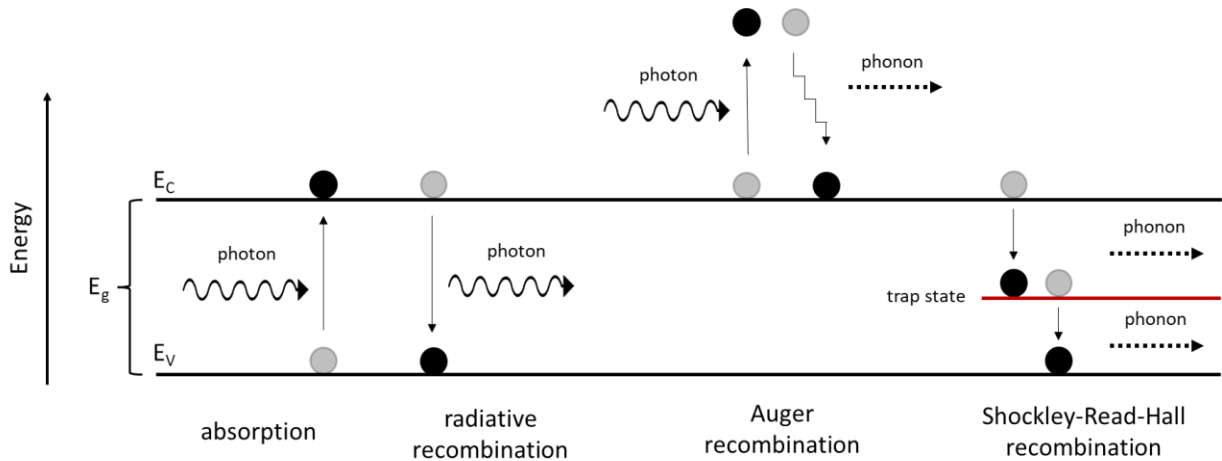


Figure 10. Illustration of absorption and the three primary recombination mechanisms. During **absorption**, a photon with sufficient energy is absorbed by a valence band electron, exciting the electron across the band gap into the conduction band, where it is prevented (for some time) from returning to the valence band by lack of available energy states. **Radiative recombination** is the opposite of absorption, whereby a conduction band electron crosses the band gap to the valence band in one discrete step, releasing its energy as a single photon with energy equal to the band gap E_g . In **Auger recombination**, an incoming photon is absorbed by a conduction band electron, pushing that electron higher into the conduction band where it will quickly thermalize down to the conduction band edge, releasing phonons in the process. In **Shockley-Read-Hall recombination**, a conduction band electron crosses the band gap to the valence band via a defect-created midgap energy state, releasing its energy in two discrete steps in the form of phonons.

The most direct pathway involves an electron losing all of its energy in a single step, falling directly to the valence band. This packet of lost energy is emitted as a photon with energy corresponding to the band gap. This process is therefore called **radiative recombination** [55], and is effectively the opposite of absorption. This form of recombination is not detrimental as the emitted photon is energetic enough to be reabsorbed by another valence band electron in the semiconductor material, creating a new electron-hole pair, in a process called photon recycling. In other words, this process is reversible, so entropy is not increased. In particularly high-performing single-crystal semiconductor materials such as gallium arsenide, material quality can be so high that lifetimes are determined by radiative recombination alone [56]. In cadmium

telluride and other polycrystalline materials, the rate of radiative recombination at one sun is typically orders of magnitude lower than by other mechanisms, so it is not usually considered.

A variation of this recombination pathway involves the radiatively emitted photon becoming absorbed by a conduction band electron rather than a valence band electron. In this process, called **Auger recombination**, instead of creating a new, useful electron-hole pair, the released energy is used to excite an electron to a higher energy within the conduction band. This electron will then thermalize back to the conduction band edge, releasing many non-usable phonons (propagating vibrations in the crystal lattice) in the process [54]. This is detrimental, as the solar photon energy which excited the initial electron-hole pair has effectively gone to waste, being ultimately converted into heat. Auger recombination only becomes significant when carrier densities are very high, such as at high irradiance or with very highly-doped materials, such as silicon [57]. As CdTe cannot yet attain very high doping and is not used with concentrator photovoltaics, Auger recombination is not significant in this technology.

A third recombination pathway involves the presence of energy states within the forbidden region of the semiconductor. These “trap states,” so called because electrons can fall from the conduction band and occupy these energy states where they are no longer free to move about the lattice, are caused by defects within the lattice structure. Defects can be “zero-dimensional” (vacancies, interstitial impurities, substitution impurities), “one-dimensional” (dislocations), and “two-dimensional” (stacking faults, grain boundaries) [58]. These energy states provide an alternative pathway for photoexcited electrons to relax to the valence band, losing their energy in two steps. Whereas the single-step energy loss of radiative recombination yields a single high-energy photon, the two-step trap-mediated recombination process instead typically yields two low-energy photons or phonons [54], and the energy of the initial absorbed

photon is effectively wasted. This detrimental process is called **Shockley-Read-Hall (SRH) recombination** [59], [60], and it is the most significant recombination mechanism in CdTe and most polycrystalline semiconductor materials.

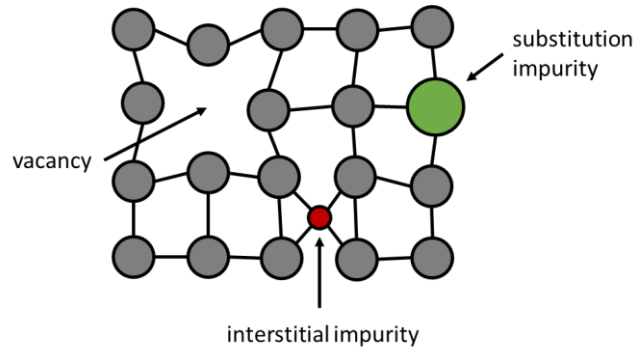


Figure 11. Schematic of several types of “one-dimensional” impurities in a crystal lattice.

There is often a distinction made between SRH recombination in the material bulk and at the interfaces between materials in the solar cell structure. Within the bulk of any polycrystalline material absorber, grain boundaries have high concentrations of defects [61]–[64] where lattices intersect non-orthogonally. Chemical impurities within the material also distort the lattice shape, creating trap states [65], [66]. Interfaces between material layers in the solar cell stack are also sites of large amounts of defects [54], particularly in CdTe where there are many heterojunctions. Lattice mismatch between materials with different crystal structure produces dangling bonds and dislocations [67], all of which inhibit electron movement and introduce undesirable energy states within the semiconductor bandgap. In CdTe, the dominant non-radiative recombination center in bulk material is the doubly-ionized $\text{Te}_{\text{Cd}}^{2+}$ defect where tellurium sits in a cadmium lattice site [68]. When CdTe traditionally undergoes copper doping to make it p-type, Cu_i and Cu_{Cd} both become problematic, representing interstitial copper and copper in a cadmium site [69]. Strategies for mitigating SRH recombination in the bulk and at interfaces are broadly similar,

with some distinctions. In both cases, lattice boundaries must be **passivated**, whereby recombination is reduced through elimination of defects or prevention of carriers from encountering defects. Without passivation, CdTe lifetimes are typically observed on the order of ~100 ps [70], with corresponding cell conversion efficiencies <5% at most [71]. Passivation in CdTe cells is almost universally accomplished by a high temperature CdCl₂ treatment, which does many beneficial things simultaneously. Chiefly, such a treatment catalyzes CdTe recrystallization into larger grains with more preferable orientation [72], as well as substantially reducing recombination at grain boundaries, identified both by first principles modeling [73] and observed experimentally [74], [75]. The result is substantially improved luminescence [70], enabling in large part the high efficiencies observed today.

The lattice constant of a crystalline material gives the interatomic distance between two equivalent atoms, effectively characterizing the lattice “size.” At layer interfaces, the more closely-matched the lattice constants of the layer materials the less the lattice geometry must distort to accommodate the chemical bonding, so the fewer opportunities for defects to form.

As two electrons cannot occupy the same lattice position due to the Pauli exclusion principle, a conduction band electron is unable to recombine if there is not a hole nearby for it to fall into. Separation of carrier types from each other is thus effective in reducing recombination even where there is a high density of traps, a phenomenon sometimes referred to as “field-effect passivation.”

Lifetime is an essential semiconductor performance parameter. As shown in equation (16), QFLS is proportional to the np product. The higher the lifetime of a material, the higher the concentration of photoexcited carriers at a given time, and thus the higher the QFLS. Lifetime is

a “macroscopic” parameter which describes millions of “microscopic” processes – as such it is a convenient interface between reality and simulation, being relatively easy to both measure in a material and implement in a model. Despite CdCl_2 passivation, lifetimes in state-of-the-art CdTe cells are still quite low when compared to other mainstream technologies. Improvement of lifetimes are a significant research focus in cadmium telluride photovoltaics; lifetime has been repeatedly identified as a primary limitation to the performance of this technology [76]–[78]. Remedial strategies involve both improving material quality and honing cell design.

2.7 Solar Cell Characterization

The most fundamental characterization measurement performed on solar cells is the current-voltage measurement, or “J-V.” In this measurement, a completed cell is illuminated by a light source simulating sunlight, a range of voltages are applied, and the current is measured at each voltage. When the current density J is plotted as a function of the voltage V , a J-V curve is created, an example of which is shown in Figure 12.

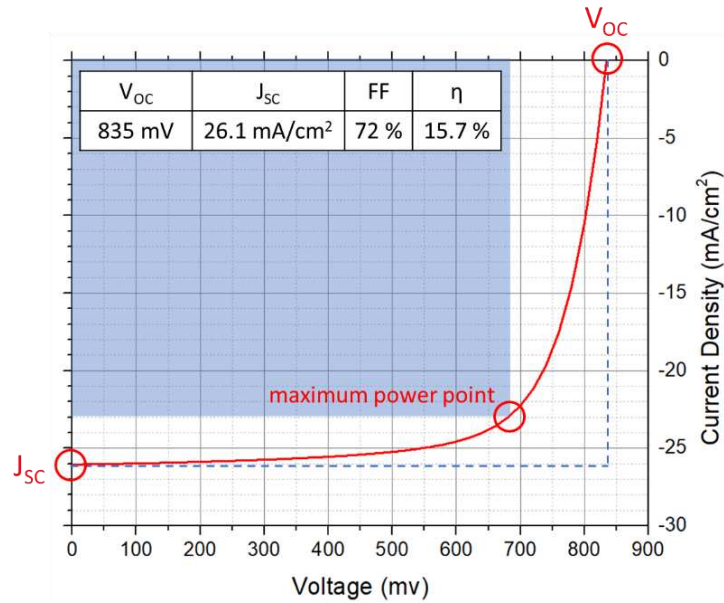


Figure 12. Example J-V curve with derived performance parameters indicated. The fill factor is essentially the ratio of areas between the shaded and unshaded rectangles.

From this curve, four important parameters are extracted. The **short-circuit current density J_{sc}** is the measured current per unit area at 0-V applied bias. The **open-circuit voltage V_{oc}** is the applied bias at which no current is extracted. Power $P = IV$, so there will be a point between J_{sc} and V_{oc} at which power is maximum; the current and voltage at this maximum power point are called J_{mp} and V_{mp} . The **fill factor FF** is defined as:

$$FF = \frac{V_{mp}J_{mp}}{V_{oc}J_{sc}} \quad (24)$$

This value essentially describes the “squareness” of the J-V curve: how close are J_{mp} and V_{mp} to J_{sc} and V_{oc} . The final parameter is the **conversion efficiency η** of the solar cell, determined from the other three:

$$\eta = \frac{V_{oc}J_{sc}FF}{P_{in}} \quad (25)$$

where P_{in} is the incident solar power per unit area, which is $\sim 100 \text{ mW/cm}^2$ at AM1.5. A cell's conversion efficiency is its highest order performance metric. However, while there is certainly information to be gained from analysis of the J-V curve, this result says very little about *why* a cell's performance is the way it is.

To answer this question, there are a large number of other characterization tools which researchers have at their disposal. Other commonly performed electrical measurements include quantum efficiency (QE) measurements in which the ratio of extracted current to incident photon flux is measured as a function of incident light wavelength. Capacitance-voltage (C-V) measurements are used to determine depletion width and carrier concentration in a cell by modulating an applied voltage and measuring capacitance.

In addition to electrical characterization requiring completed photovoltaic devices, a variety of material characterization tools are available which determine attributes such as grain size and shape, elemental composition, crystal orientation, band structure, and more. A partial list includes scanning and transmission electron microscopy, secondary ion mass spectrometry, x-ray diffraction crystallography, x-ray and ultraviolet photoelectron spectroscopy, energy-dispersive x-ray spectroscopy, and electron energy loss spectroscopy. None of these tools will be discussed in this dissertation, but all are valuable for gaining understanding of cell performance beyond the J-V curve.

Luminescence measurements are another class of semiconductor characterization, involving the detection of radiative emission due to recombination of injected carriers. These include steady-state and time-resolved photoluminescence, electroluminescence, and

cathodoluminescence. Though the carrier injection and detection methodologies differ, all of these measurements ultimately reflect radiative and nonradiative recombination processes, allowing for the most direct observation of carrier recombination dynamics. Information which can be gained from such measurements includes lifetime, bandgap, trap characterization, spatial uniformity, and identification of recombination centers. As substantial nonradiative recombination is a contributor to CdTe's persistent voltage deficit, this class of measurements is particularly pertinent to the challenge of improving CdTe cell efficiency, and closing the gap to the Shockley-Queisser limit.

CHAPTER 3. TRPL MEASUREMENT AND ANALYSIS

Time-resolved photoluminescence (TRPL) is the definitive method for determining carrier lifetimes in thin-film polycrystalline solar cells. This measurement creates electron-hole pairs in the semiconductor material using pulsed laser light, and the decay of radiative emission is measured in between the pulses. The short ($<1 \mu\text{s}$) lifetimes in these polycrystalline materials generally require detection using time-correlated single photon counting (TCSPC) [79], [80]. In this technique individual photons are detected by a photomultiplier tube or avalanche diode, and precision timing electronics assign each photon to a time “bin” in a histogram. Accumulated counts over many millions of pulses yields a decay curve containing information about carrier dynamics within the material. TRPL is a particularly useful method of characterization as it is nondestructive, very sensitive, and can be performed at nearly any point within the solar cell fabrication process [81]. Contacts and even basic cell structure are not needed; indeed, TRPL is often performed on semiconductor materials in isolation.

Interpretation of TRPL is well-established when performed on pure semiconductor materials or specialized double-heterostructures (DHs). This non-diode DH architecture consists of a semiconductor layer flanked by transparent passivating barrier layers, and is used to probe bulk material properties in polycrystalline thin-film technologies. Measurements performed on these structures at low injection generally yield single-exponential decays [82]–[84], the time constants of which represent the limiting recombination mechanism – in CdTe this is typically SRH recombination. However, fabrication of double-heterostructures to probe bulk material properties is highly specialized, and material properties may be substantially different in the processes used in actual cell fabrication. It is therefore essential to measure TRPL on completed solar cells and extract material properties from such data.

While TRPL measurements on completed cells are commonly performed, their interpretation is often complicated by recombination at interfaces between the different cell layer materials. In addition, p-n junction fields can have significant effects on carrier dynamics, which can have a major impact on the TRPL decay curves [85], [86]. This chapter aims to shed some light on the effects of junction fields, as this particular facet is rarely discussed, at least in the context of CdTe photovoltaic devices. Applying external electrical bias directly modulates the space-charge fields in ways which can be predicted reasonably well using modeling. Therefore, field effects in a TRPL measurement can be directly probed with this bias modulation; results and discussion of this novel measurement are presented in this chapter.

To better understand and explain the results, a sophisticated modeling tool was developed to simulate TRPL measurements under electrical bias, and this modeling was applied to a typical CdTe cell structure with a wide range of material parameter values. This model is described in detail, and its key findings are elucidated. Agreement between the simulations and experiments is very good, and the modeling allows extrapolation to conditions which would be difficult to achieve experimentally.

3.1 TRPL System

All measurements were performed using the TRPL system at the National Renewable Energy Lab (NREL). While this author had no part in the design and assembly of the system, all reported measurements were performed by the author, and a detailed description of the system operation is provided for completeness. This system utilizes an optical parametric amplifier seeded by a regeneratively-amplified Yb:KGW (ytterbium-doped potassium gadolinium tungstate) laser as the excitation source. Luminescence photons pass through an optical bandpass

filter to eliminate scattered laser light before being detected by an avalanche photodiode (APD) and counted by timing electronics.

3.1.1 Oscillator

The process of producing excitation light for the TRPL measurement begins with the oscillator [87]. Here, a diode-laser-pumped Yb:KGW (ytterbium-doped potassium gadolinium tungstate) crystal produces coherent 1030-nm radiation. Mode-locking in the optical cavity generates ~90-fs pulses at a rate of 76 MHz. Pulses are stretched using a transmission diffraction grating to reduce peak power during the subsequent amplification. Roughly every one in seventy pulses is injected into the regenerative amplifier (RA) using a Pockels cell. Within the RA, the pulse makes many passes on a second diode-laser-pumped Yb:KGW crystal, before the Pockels cell releases the amplified pulse, which is subsequently compressed back down to ~300 fs. The repetition rate of amplified pulses is 1.1 MHz, but a second “pulse picker” Pockels cell can be used to reduce this rate in multiples of 2, allowing coarse control of laser repetition rate during a TRPL measurement. The powerful 1030-nm beam from the oscillator is then used to seed the optical parametric amplifier.

3.1.2 Optical Parametric Amplifier

The excitation light used in the TRPL measurement is generated by the optical parametric amplifier (OPA) [88]. Within the OPA, the high energy 1030-nm pulsed seed beam from the oscillator is first split in two: most of the beam is frequency-doubled to 515 nm with a second harmonic generation crystal while a small portion is used to generate white light using a sapphire white light continuum generation substrate. Both second harmonic and supercontinuum generation are nonlinear optical processes, requiring very high optical intensity from the seed

beam. The 515-nm beam is used as a pump source for the subsequent pre-amplifier and power amplifier.

The white light is then focused onto a nonlinear optics crystal along with the 515-nm pump beam in the preamplifier. Two mirrors with motor-controllable separation act as a delay stage for the white light, allowing pre-amplification of a specific wavelength within the white light through precise timing of both beams' incidence on the crystal. The selected amplified wavelength, called the "signal" is then directed to another nonlinear optics crystal along with the 515-nm pump beam for parametric power amplification. In this process, the signal is amplified by converting pump beam photons into photons at the signal wavelength within the crystal. Conservation of momentum dictates that another, lower energy photon beam is created in the process, called the "idler":

$$\frac{1}{\lambda_{pump}} = \frac{1}{\lambda_{signal}} + \frac{1}{\lambda_{idler}} \quad (26)$$

The signal and idler beams both emerge from the OPA with opposite polarization. The desired beam wavelength is then selected by a polarizer. For single-photon excitation TRPL, usually the signal is desired, while the longer-wavelength idler is often used for two-photon measurements. Conservation of momentum dictates that neither the signal nor the idler can have a higher energy than the pump. Therefore, to attain wavelengths shorter than 515 nm, the signal beam can undergo second harmonic generation via another nonlinear crystal.

Though complexity is very high, the optical parametric amplifier allows precise wavelength tuning over a large range, allowing many types of measurements on different materials to be performed. For typical one-photon measurements on CdTe, 640 nm light was

used at a repetition rate of 1.1 MHz, though very long lifetimes discussed in Chapter 4 necessitated a lower repetition rate.

3.1.3 Time-Correlated Single Photon Counting

The emitted luminescence passes through a bandpass filter which only allows transmission of photons with energy near the bandgap of the measured material. Fluorescence decay lifetimes of CdTe-based photovoltaic samples can vary widely, from <1 ns to >6 μ s, though are generally on the order of tens to hundreds of nanoseconds in modern, state of the art cells. Measurement of such short timescales with high enough resolution to perform multi-exponential fitting necessitates detection using time-correlated single photon counting (TCSPC). In this method, individual photons are detected and precision timing electronics assign each photon to a time “bin” in a histogram. Accumulated counts over many millions of pulses are used to assemble a decay curve.

Many electronic components are necessary for this process. In the NREL TRPL system, photons are detected by a silicon avalanche photodiode (APD), which is cooled with a Peltier stage to reduce thermal noise. The output of the APD is binary as the avalanche breakdown is actively quenched, corresponding to signal registry – if a photomultiplier tube is used, the fluctuating output must be converted into a binary signal by a constant fraction discriminator (CFD). To assign photons, the time to amplitude converter (TAC) begins linearly ramping voltage with the laser synchronization signal and stops with the photon detection signal, yielding a voltage proportional to the elapsed time between signals. Next the analog to digital converter (ADC) converts this voltage into the digital timing value required by the histogrammer. The PicoQuant TCSPC system utilized is more sophisticated and has different components which

combine several of the above-mentioned operations into one, but the operating principle is the same.

Temporal accuracy of the TCSPS system is determined by the instrument response function (IRF). This is essentially the measured decay of scattered excitation light; an ideal system with infinite accuracy would yield an infinitely narrow IRF. The three main sources of IRF broadening are timing uncertainty in the detector's conversion of a photon into an electrical signal, inaccuracy in the laser pulse timing reference, and timing jitter of electronic components by RF interference [89]. The IRF in the NREL TRPL system is narrow enough that lifetimes as low as ~ 0.1 ns can be extracted from TRPL tails. Lifetimes down to ~ 20 ps can be extracted from deconvolution of the measured decay with the IRF using software, if need be.

APDs have a "cool-down" time after each detection, during which incident photons will not be detected. This is mostly a function of an intentional post-detection hold-off time to prevent afterpulsing, a false detection after a true detection resulting from detrapping of carriers in the diode's depletion layer, a phenomenon which is exacerbated by low temperature [90]. Significant amounts of missed photons will distort the shape of the decay, so to ensure accurate reproduction, single-photon statistics must be maintained. To achieve this, the optical signal is attenuated by neutral density filters before it reaches the APD until only about 2% of laser pulses yield a detected photon. This signal attenuation effectively limits the detection sensitivity of this technique to three or at most four orders of magnitude, no matter how bright the luminescence is. It is for this reason that TCSPC starts to become impractical as the lifetime of the material exceeds ~ 1 μ s, as the time required for data collection while preserving signal-to-noise ratio becomes longer as lifetime increases. In the μ s timescale and beyond when there are ample luminescence photons, it is much simpler to simply process ADP or PMT output with an

oscilloscope in binning mode, capturing the entire decay trace after each pulse [91]. Summing millions of traces can yield a smooth decay curve in seconds.

3.2 Decay Fitting

Time-resolved measurements are inherently dynamic, and the resulting transients represent different forms of recombination over different timescales, depending on what is being measured. As such, a TRPL decay can have a complex shape (ex. see Figure 13). Typically there is an initial faster decay followed by a slower decay at later times. Such a shape can be loosely approximated by a double-exponential fit, yielding a faster τ_1 lifetime and a slower τ_2 lifetime [92], [93]:

$$I(t) = A_1 e^{-\frac{t}{\tau_1}} + A_2 e^{-\frac{t}{\tau_2}} \quad (27)$$

where I is the luminescence intensity and A_1 and A_2 are weighting factors. Alternatively τ_1 and τ_2 can be attained from single exponential fits limited to the fastest or slowest part of the decay, respectively. τ_1 is often attributed to nontrivial fast carrier dynamics with particular influence from laser excitation [94], [95] and recombination at the front interface [96], [97]. In the most widely-used interpretation, τ_2 is often the only desired value, and is synonymous with the reported “lifetime” of the material. It is understood to reflect the density of defects in the bulk with some influence from defects at the interfaces [98], [99]. However, this is only a generalization; τ_1 and τ_2 can easily represent different phenomena depending on the characteristics of the solar cell and the conditions of the TRPL measurement.

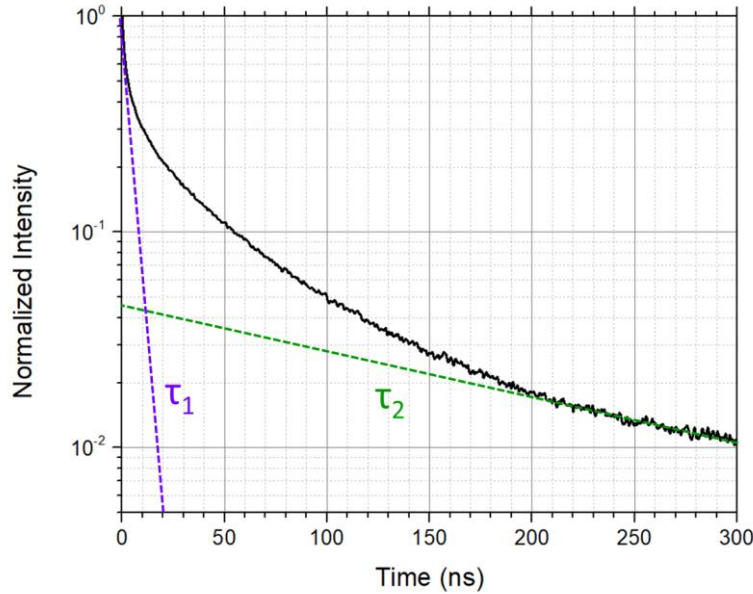


Figure 13. Example of a measured TRPL decay. Slopes corresponding to manual τ_1 and τ_2 fits are indicated.

While the double-exponential approximation is useful, there is not much physical basis for it, and it is often preferable to deliberately choose the timescale(s) over which fitting is performed. Proper TRPL fitting is not prescriptive – extraction of lifetime(s) is best done on an individual decay-by-decay basis with an experienced eye. Typically, the decay rate will reach a steady-state minimum after enough time has passed, at which point there are the fewest complicating factors influencing recombination. Determining this decay rate with a single-exponential fit is the best way to report the “lifetime” of the sample, and this is the method which is employed to attain τ_2 in the measured and simulated decays in this chapter. As the modeling reveals, even this rate by no means has a universal interpretation and can be fraught with complications. Keeping with established convention, the “ τ_1 ” and “ τ_2 ” terminology will be used

in this chapter, but it must be emphasized that it is a naming convention only, and these values do not come from double-exponential fitting.

3.3 TRPL Modeling

To truly understand what a TRPL measurement is representing, it is important to develop a model to compare with measured data. Designing and executing experiments to comprehensively investigate behavior under a broad range of specific conditions is infeasible to impossible. With simulations however, a wide parameter space can easily and quickly be explored. In order to observe carrier behavior during TRPL to best explain measurement results, a simulation tool was developed which reproduces luminescence over time after a configurable injection of carriers into a material with user-specified potential gradients. These potential gradients are a function of the cell structure and external applied bias; this tool therefore enables simulation of biased measurements of any absorber with any doping in any cell configuration at any excitation intensity and wavelength (limited only by difficulty with numerical convergence).

3.3.1 Fundamental Equations

Simulation of TRPL of CdTe cells under bias were performed with a MATLAB script based on *Weiss et al.* [100]. This script uses MATLAB's solver for systems of partial differential equations to solve transport equations for electrons and holes to calculate the concentration of each at each mesh position within a semiconductor absorber layer at each timestep.

Photoluminescence at each timestep is calculated as the product of excess electrons and holes integrated across the absorber thickness:

$$PL(t) = B \int_0^L [n(x,t)p(x,t) - n_0(x)p_0(x)]dx \quad (28)$$

where B is the radiative recombination coefficient (units cm^3/s), L is the absorber thickness, n and p are the electron and hole concentrations, and n_0 and p_0 are the equilibrium (dark) concentrations. Photoluminescence at time t is thus equivalent to the total amount of radiative recombination within the absorber at t . It is therefore assumed that radiatively emitted photons are not reabsorbed; since photon recycling effects only become significant in radiative recombination-limited materials, this modeling simplification is acceptable in SRH-limited CdTe [101], [102]. $PL(t)$ has units of photons/s/cm², but absolute quantities are not relevant for TRPL; only values relative to each other over the decay are (normalized to the maximum).

Each transport equation contains terms corresponding to generation due to laser injection, recombination due to deep-level traps and radiative processes, and movement due to **drift** driven by electric fields and **diffusion** driven by carrier concentration gradients. The transport equations are given below [103]:

$$\frac{\partial n}{\partial t} = \frac{\partial}{\partial x} \left(D_n \frac{\partial n}{\partial x} + \mu_n n E_n \right) - R_n + G \quad (29)$$

$$\frac{\partial p}{\partial t} = \frac{\partial}{\partial x} \left(D_p \frac{\partial p}{\partial x} - \mu_p p E_p \right) - R_p + G \quad (30)$$

where n and p are the concentrations of electrons and holes, respectively. Each carrier type can have its own diffusion coefficient D (units cm^2/s) and mobility μ , and be subject to its own field E . The $\frac{\partial}{\partial x} (\quad)$ term represents the motion of carriers; $D \frac{\partial \rho}{\partial x}$ describes diffusion and $\mu \rho E$ describes drift. The diffusion coefficient is closely related to carrier mobility by the Einstein relation [104]:

$$D = V_T \mu \quad (31)$$

where V_T is the “thermal voltage:”

$$V_T = \frac{kT}{q} \quad (32)$$

where q is the elementary charge, k is the Boltzmann constant, and T is the temperature. At 300 K, $V_T \approx 25.85$ mV. As the potential difference across the absorber of a cell is generally much higher than this in the dark, drift is typically the driving mechanism where there are no large concentration gradients. $qD \frac{\partial \rho}{\partial x}$ and $q\mu\rho E$ are called the diffusion and drift current densities, respectively.

The recombination term R (units $\text{cm}^{-3}\text{s}^{-1}$) contains radiative recombination as well as capture and emission from a midgap trap state:

$$R_n = B(np - n_0p_0) + C_n - E_n \quad (33)$$

$$R_p = B(np - n_0p_0) + C_p - E_p \quad (34)$$

where (E_n, C_n) and (E_p, C_p) are the emission and capture rates of electrons and holes into and out of the trap. The capture rate of electrons from the conduction band into the trap is [105]:

$$C_n = n(N_{trap} - n_{trap})\sigma v_{th} \quad (35)$$

The emission rate of electrons from the trap into the conduction band is:

$$E_n = n_{trap}N_C e^{-\frac{E_G - E_{trap}}{kT}} \sigma v_{th} \quad (36)$$

The capture rate of holes from the valence band into the trap is:

$$C_p = pn_{trap}\sigma v_{th} \quad (37)$$

And the emission rate of holes from the trap into the valence band is:

$$E_p = (N_{trap} - n_{trap})N_V e^{-\frac{E_{trap}}{kT}} \sigma v_{th} \quad (38)$$

N_{trap} is the trap density, σ is the trap cross-section, v_{th} is the thermal velocity of carriers, n_{trap} is the concentration of carriers in the trap, and E_{trap} is the trap energy, measured from the conduction band. N_C and N_V are the density of states in the conduction and valence bands,

respectively. In principle these parameters can be different and can vary with temperature, but all simulations presented here are at room temperature and assume symmetric bands, with $N_C = N_V$.

The script allows up to three distinct traps, each with its own C_n , E_n , C_p , and E_p . The recombination terms R therefore nominally include two additional capture and emission rates each corresponding to these additional traps. However, only a single trap was used in this application, with energy at midgap to represent the most comprehensive, deleterious circumstances. This should be a sufficient approximation for investigating the effects of nonradiative recombination. In CdTe technology in particular, there is no specific motivation for adding other trap states; for example, there is no widely-held knowledge of ubiquitous traps which always appear at specific energy levels, nor a commonly-observed Stokes shift, etc.

E_{trap} is the trap energy, measured from the conduction band. As mentioned, in all applications the trap energy is set to $\frac{E_G}{2}$. Bulk lifetime due to defects is described by the Shockley-Read-Hall lifetime:

$$\tau_{SRH} = \frac{1}{\sigma N_{trap} v_{th}} \quad (39)$$

where σ is the defect cross-section, N_{trap} is the defect density, and v_{th} is the thermal velocity of carriers [106]. The defect cross-section is held constant at 10^{-11} cm² and N_{trap} is varied to attain the desired bulk lifetime.

The generation term G is a normal distribution in the time domain and a decaying exponential in the position domain:

$$G(x, t) = I_{inj} \alpha e^{-\alpha x} * \frac{1}{w\sqrt{\pi/2}} e^{-\frac{2(t-\mu)^2}{w^2}} \quad (40)$$

where I_{inj} is the injection intensity, α is the absorption coefficient of the absorber material at the desired laser wavelength, w is the width of the pulse and μ is the pulse center (*not* mobility here). The depth of penetration is determined by α ; simulating two-photon excitation would be accomplished by changing this parameter. The width of the Gaussian pulse is set to 100 ps by numerical necessity. Pulses utilized in the TRPL measurement are on the order of 300 femtoseconds, but this is smaller than the timestep used in the simulation. Since observable dynamics happen on the scale of nanoseconds, the artificially long pulse lengths are not a source of meaningful error. Additionally, the width of the instrument response function is ~ 0.5 ns, so dynamics on the femtosecond timescale are unobservable in the measurement anyways. The pulse is centered at 1 ns, though as $t = 0$ is arbitrary, this is only relevant insofar as to allow numerical convergence, and has no physical significance.

The remaining equations describe the occupation of the trap states themselves, n_{trap} , following the general form:

$$\frac{\partial n_{trap}}{\partial t} = C_n - E_n - C_p + E_p \quad (41)$$

Once again, the script allows up to three traps, adding three equations of the above form to the system of equations. Only one trap is used in this application, however.

3.3.2 Adding Fields

A vital addition to the script beyond the version in *Weiss et al.* [100] is the inclusion of electrostatic coupling. Equations (29) and (30) alone work well when simulating bulk absorber material or double heterostructures at low injection, when there are no (or weak) internal fields and thus the concentrations of carriers are relatively uniform within the material. However, in

completed cells with p-n junctions, strong internal fields separate carriers from each other, creating a heavy concentration of electrons at the front and holes at the back. These large charge density gradients create their own fields which the basic transport equations do not account for. The field term E in equations (29) and (30) must accordingly itself be a variable, not a constant. Therefore, in addition to the transport equations above, the Poisson equation [107] must be solved for electrons and holes, adding two more equations of the following form to the system:

$$\frac{\partial^2 V}{\partial x^2} = \frac{q}{\epsilon} (p - n - N_A^+ + N_D^-) \quad (42)$$

where V is the potential felt by the carriers (the field $E = \frac{\partial V}{\partial x}$), q is the elementary charge, ϵ is the permittivity of the absorber material, and N_A^+ and N_D^- are the concentrations of ionized acceptors and donors, respectively. Since only the p-type absorber is modeled, N_A^+ is assumed to be equal to the intrinsic doping concentration, while N_D^- is assumed to be zero everywhere. As electrons and holes may experience different potentials in the case of graded bandgap absorbers, two variables (V_n and V_p) are used, and equation (42) is implemented twice. All applications discussed here use a single-material absorber, so $V_p(x) = V_n(x) - E_G$ for all x .

The potential V variable is equivalent to the position of the bands. Thus, the Poisson equation effectively solves for the dynamic adjustment of band bending in response to the introduction and movement of excess carriers within the material. The Poisson equation increases numerical complexity considerably as it adds two elliptic PDEs to a system of otherwise parabolic PDEs, necessitating careful adjustment of error tolerances to produce a solution. The boundary conditions for the potential are crucial for accurately reflecting experimental conditions. The focus of this chapter is on biased measurements; in this situation the potential at the contacts is fixed by the external power supply. Therefore, the boundary

conditions used in the modeling specify that $V(t)|_{x=0,d} = V_{initial}|_{x=0,d}$. Traditional TRPL measurements are performed at open circuit, where this potential restriction does not apply. To model an open circuit measurement, at least one absorber interface must be free from boundary conditions. The MATLAB script utilized here requires boundary conditions of a certain form to be specified at *both* contacts, so it is unable to accurately model open circuit measurements on p-n junction structures. Open circuit can be approximated by forward bias, as the band-flattening effects of injection functionally reduce the potential difference between the contacts, but to truly model open-circuit TRPL of a solar cell a more advanced modeling tool is needed. Since the interest here is in modeling biased measurements however, the MATLAB script is adequate.

Trap-mediated recombination at the interfaces of the absorber are implemented as carrier density boundary conditions:

$$D_n \left. \frac{\partial n}{\partial x} \right|_{x=0,L} + \mu_n E_n n \Big|_{x=0,L} = -S_{front,back} \left. \frac{np - n_0 p_0}{n + p} \right|_{x=0,L} \quad (43)$$

where $x = 0$ and S_{front} correspond to the front interface and $x = L$ and S_{back} correspond to the back interface (L is the thickness of the absorber). Many of the variables which were scalars in the original script have been converted into vectors to allow variation across the absorber.

Particularly useful is the lifetime parameter, as it was found that interface recombination is more effectively and realistically implemented by reducing the lifetime for some depth into the bulk at the interfaces (either graded or abrupt) rather than simply relying on the boundary conditions in equation (43). An interpretation of this finding is that “interface” effects are rarely confined to just the interface – lattice mismatch and misfit dislocations propagate strain over some distance, producing three-dimensional defective *volumes* at the edges of the absorber bulk. Interface

recombination is not a focus of this work, but this modeling tool can be used to evaluate its effects on TRPL in the future.

Lastly, the model does not include photon recycling (as mentioned) or Auger recombination. Neither of these mechanisms are currently significant in CdTe devices, as lifetimes and doping are too low.

3.3.3 Simulating Biased TRPL of a Solar Cell

To simulate TRPL on solar cell structures, the modified script requires band diagrams and carrier concentration profiles within the absorber material in dark equilibrium. SCAPS 1D is a free tool developed at the University of Ghent [108] which performs this task well, but other semiconductor device modeling packages (Sentaurus TCAD, COMSOL Multiphysics) would work as well. The SCAPS outputs are the initial conditions of the PDE solver, and subsequent evolution is determined by the solutions to the system of equations at each timestep. Device parameters used in SCAPS are based on previous modeling [109] and are reported in Table 1.

Table 1. Parameters for TRPL modeling.

Quantity	Symbol	Value
temperature	T	300 K
electron mobility	μ_e	1 – 25 $\text{cm}^2\text{V}^{-1}\text{s}^{-1}$
hole mobility	μ_h	0.2 – 5 $\text{cm}^2\text{V}^{-1}\text{s}^{-1}$
bulk lifetime	τ_{bulk}	1 – 500 ns
absorption coefficient	α	$6 \times 10^4 \text{ cm}^{-1}$
radiative recombination coefficient	B	$1 \times 10^{-10} \text{ cm}^3\text{s}^{-1}$
relative permittivity	κ	9.4
carrier thermal velocity	v_{th}	10^7 cm s^{-1}
effective density of states	DOS_{eff}	$8 \times 10^{17} \text{ cm}^{-3}$
absorber thickness	L	2 μm
carrier concentration	N_A	$10^{14} - 10^{16} \text{ cm}^{-3}$
bandgap	E_G	1.5 eV
front interface recombination velocity	S_{front}	10^0 cm s^{-1}
back interface recombination velocity	S_{back}	10^0 cm s^{-1}
excitation power	-	$10^{11} - 10^{13} \text{ photons/pulse/cm}^2$
pulse width	-	100 ps

3.4 TRPL Modeling Results

An idealized 2- μm single-absorber cell structure was simulated in SCAPS, and its dark equilibrium band diagram and carrier concentration profiles at a range of biases from -0.75 V to +1 V were calculated, shown in Figure 14. It is clear that forward bias flattens the bands and reduces the junction fields, while reverse bias does the opposite. The parameters used in the simulation are given in Table 1.

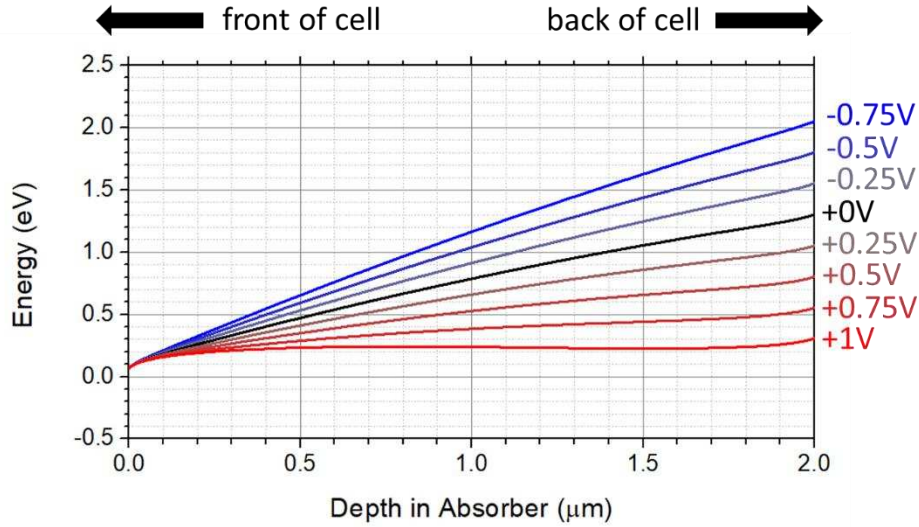


Figure 14. Simulated conduction band profile within the modeled CdTe absorber at a range of biases. Forward bias decreases the potential difference between the ends of the absorber, weakening fields. Reverse bias does the opposite. The valence band is omitted for clarity of presentation; as this is an ungraded absorber the valence band tracks the conduction band at 1.5-eV lower energy everywhere.

The bulk material lifetime in the MATLAB model was then varied from 1 ns to 500 ns, and decay curves were simulated at each bias and bulk lifetime. τ_2 fits were extracted from the curves, and the comparison of τ_2 with the true bulk lifetime for each curve is shown in Figure 15a. The dashed line with unity slope indicates where the measured decay times would be equal to the true absorber lifetimes. In this cell configuration, this plot shows that when bulk lifetime is low (<5 ns), τ_2 from TRPL closely matches the true lifetime, and bias has very little effect. When bulk lifetime is high (>5 ns), however, τ_2 becomes increasingly bias dependent. The simulations reveal that at higher lifetimes, τ_2 will underestimate the true bulk lifetime at most biases, and when bulk lifetime is very high (>100 ns), τ_2 becomes nearly completely independent of τ_{bulk} . Note that the simulated cell here has ideal interfaces with $S_{front} = S_{back} = 1$ cm/s, so that measured lifetime reduction below that of the bulk is purely due to field effects.

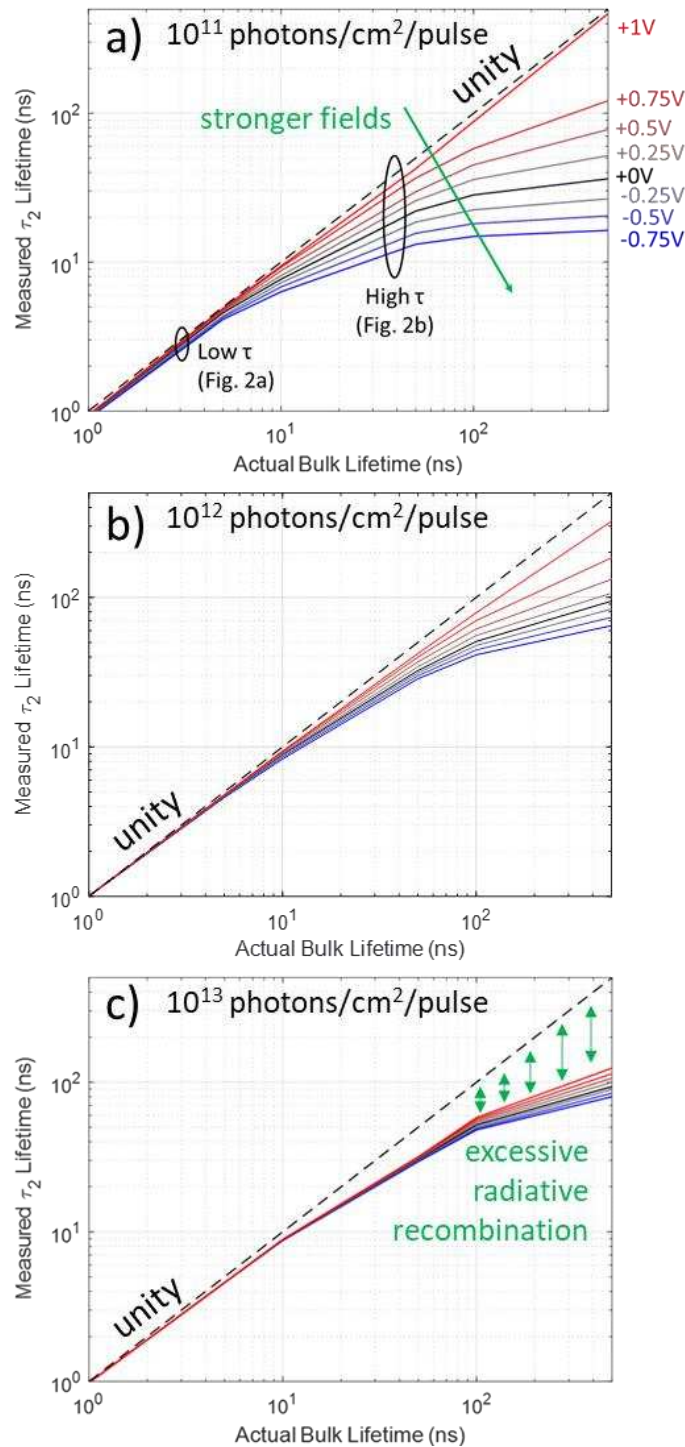


Figure 15. Extracted τ_2 lifetime from decay tail vs specified bulk lifetime parameter for many simulated TRPL decays at a range of biases. Dashed lines indicate where a decay's τ_2 would be equal to the bulk lifetime. Simulations performed with a) 10^{11} , b) 10^{12} , and c) 10^{13} photons/cm²/pulse excitation. Approximately 150 simulated TRPL decays are represented in this figure.

Luminescence decay over time can be influenced by many mechanisms, the rates (or inverse time constants) of which are additive [98], [110]:

$$\frac{1}{\tau_{eff}} = \frac{1}{\tau_{bulk}} + \frac{1}{\tau_{drift}} + \frac{1}{\tau_{int}} + \frac{1}{\tau_{rad}} + \dots \quad (44)$$

where τ_{eff} is the effective, measured lifetime over a given timescale and τ_{bulk} , τ_{drift} , τ_{int} , τ_{rad} , etc. represent lifetimes due to various relevant luminescence decay processes over that timescale. Namely, these mechanisms include SRH recombination in the bulk and at interfaces, radiative recombination in the absorber, and carrier separation due to drift. There could be others, but these are the most relevant in a CdTe cell. The trends observed in Figure 15a are explained by the competition between Shockley-Read-Hall recombination in the bulk and drift represented in equation (44). At a given bias, as τ_{bulk} increases the SRH recombination rate decreases while the carrier drift rate is unchanged. In this example, when $\tau_{bulk} < 5$ ns, the bulk SRH recombination rate is dominant. Around $\tau_{bulk} = 5$ ns, these two rates become close enough that both influence τ_2 , reducing τ_2 below τ_{bulk} . As τ_{bulk} increases further, the relative influence of drift becomes larger, until at a high enough τ_{bulk} the recombination rate effectively no longer influences the decay. As drift becomes dominant, the luminescence reduction with time no longer represents a reduction in the number of excess carriers, but instead represents a reduction in the ability of carriers to recombine because they are separated from each other. There is overall more deviation from the true lifetime as the field strength increases in reverse bias.

Figure 15b shows the same set of simulations as Figure 15a at ten times higher excitation power. Differences between biases are reduced, and this is true over the entire range of bulk lifetimes. The local field-suppressing effects of injection are therefore stronger than the field-manipulating effects of bias, and high injection can be a suitable way to suppress fields [111],

[112] and accurately measure bulk SRH lifetime. However, high excitation power increases the radiative recombination rate $\frac{1}{\tau_{rad}}$ which can reduce the measured lifetime [82], [92], [94], [110], particularly as τ_{bulk} increases. This is demonstrated in Figure 15c with a hundred times higher excitation power. Bias no longer has a significant effect, meaning that the fields are nearly entirely suppressed. However, the deviation of τ_2 from τ_{bulk} is now substantial when τ_{bulk} is high, due to increased radiative recombination from the higher carrier injection. As this is not a field effect, forward bias does not suppress it.

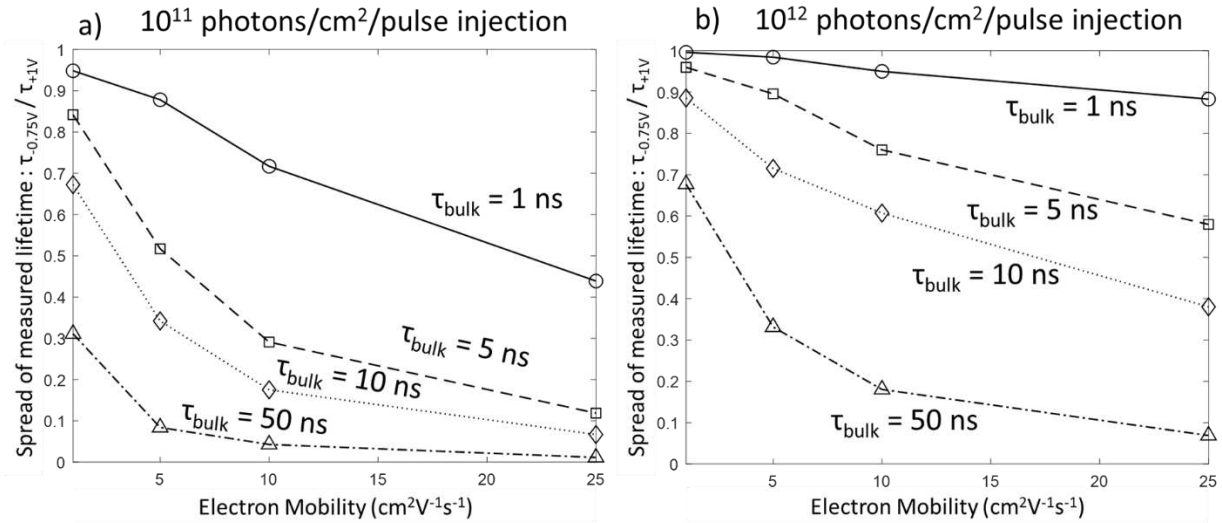


Figure 16. Spread of measured lifetime over the entire bias range ($\frac{\tau_{-0.75V}}{\tau_{+1V}}$) vs carrier (electron) mobility for four bulk lifetime values. This y-axis ratio semi-quantitatively describes how much influence fields have on a TRPL measurement: a ratio of 1 signifies no effect, while smaller values indicate increased interference. Simulations at a) 10^{11} and b) 10^{12} photons/cm²/pulse injection shown. These plots show that fields have a larger effect at higher mobility, higher lifetime, and lower injection.

The drift rate in equation (44) can be generally expressed via unit analysis as $\frac{1}{\tau_{drift}} \approx \frac{\mu E}{d}$,

where μ is carrier mobility, E is field strength, and d is some lengthscale over which carriers move – the depletion width is an appropriate quantity. Mobility is therefore an important

parameter; higher mobility increases the drift rate for a given field, effectively magnifying the influence of fields on TRPL. Mobility is difficult to measure and control in physical cells, but it is worthwhile to explore with simulation to shed light on potential effects. The simulation set from Figure 15 was repeated with three higher carrier mobility values and the results are summarized in Figure 16. In both plots, the y axis is the ratio of τ_2 at -0.75 V bias to τ_2 at +1 V bias. This quantity semi-quantitatively represents the spread of measured lifetime with bias: when the ratio equals 1, bias has no effect on lifetime, while lower ratios indicate increasing lifetime reduction in reverse bias. The x axis represents electron mobility μ_e (hole mobility is held at $\mu_h = 0.2\mu_e$). The plots indicate that the variation of τ_2 with bias increases as mobility increases, as the field exerts a stronger influence. In addition, this plot reiterates the findings in Figure 15 that the variation with bias is greater at higher bulk lifetime. This is important, as it suggests high-performing cells with high lifetime and mobility are most likely to yield misleading results from TRPL if field effects are not considered. Figure 16a and Figure 16b utilize 10^{11} and 10^{12} photons/cm²/pulse excitation power, respectively. The similar decrease in the bias effect at higher injection shown in Figure 15 is also observed here, and holds for all mobilities tested. The same simulation set was attempted at 10^{13} photons/cm²/pulse excitation, but the solver is particularly prone to convergence failure when combining high injection with high mobility, so the resulting data set is very incomplete, and is not shown here. Nevertheless, the qualitative trend of diminishing bias dependence with increasing injection is expected to hold, regardless of mobility.

In the idealized simulated structure, +1 V bias represents a voltage in which there is minimal potential difference between the contacts. With equipotential contacts, internal fields are nearly completely suppressed, all but eliminating the drift rate term in equation (44). This

engenders good agreement between measured τ_2 and true τ_{bulk} over the entire range of τ_{bulk} , independent of mobility, provided the excitation power is low enough to not introduce radiative recombination rate effects (see the +1 V line in Figure 15). Taken as a whole, Figure 15 is a clear illustration that bulk lifetime is most accurately extracted from TRPL at low excitation power under forward bias. In physical cells, however, even under these conditions, extracted lifetime will still be influenced by interface recombination.

3.5 Cell Fabrication

To validate the model's findings it is necessary to perform biased TRPL measurements on physical cells. Complete solar cells are fabricated at CSU using a variety of deposition methods for the layers within. The structure of a "traditional" cell is as follows. The superstrate configuration cells begin with commercial TEC10, which is soda-lime glass with a layer of fluorine-doped tin oxide (FTO), an n-type highly-conductive transparent front contact. Next, the n-type emitter layer is typically 80-100 nm of magnesium zinc oxide (MgZnO) deposited by RF sputtering [113]. This material does not have the parasitic absorption of cadmium sulfide (CdS) emitter layers from CdTe's past, and forms a well-passivated interface with CdTe-based absorber materials. Next, one or more absorber materials are deposited by close-space sublimation (CSS) [114]. The most basic configuration involves a single layer of CdTe. More recently, selenium-containing alloys are typically incorporated, often as a CdSeTe/CdTe bilayer. A passivation treatment follows, depositing CdCl₂ by CSS and subsequently annealing to distribute the chlorine throughout the absorber and remove stacking faults [115]. Chlorine accumulates at CdTe grain boundaries and passivates defects in the grain boundary band gap [116] (see Section 2.6). The absorber materials then undergo a copper doping treatment, also with CSS, to increase p-type carrier concentration to form a junction with the MgZnO emitter layer. A 40-nm layer of

tellurium deposited by evaporation, in conjunction with heavier copper doping at the back of the absorber, helps mitigate the deleterious effects of the Schottky barrier which forms between the CdTe and metal back contact [117]. The final layer is the nickel back contact, which utilizes a spray-deposited colloidal suspension of nickel with a polymer binder in methyl ethyl ketone. Each completed 3.1" × 3.6" substrate is then delineated into 25 individual ~0.6 cm² cells by sandblasting through a mask. Incomplete or irregular sandblasting yields intermittent and poor quality conduction to the FTO, so a grid of indium is soldered around each cell to cover these gaps and provide a good electrical connection to the front contact for measurement purposes.

3.6 TRPL Measurement Results

3.6.1 Low and High Lifetime

The contrast between low and high lifetime absorbers was investigated with two sets of solar cells manufactured at Colorado State University (CSU), following the procedure described in Section 3.5. The only significant difference between the two is in the composition of the 2- μ m absorbers: one uses CdTe as the absorber material, with associated low bulk lifetime, while the other utilizes a bilayer absorber incorporating a 0.5- μ m CdSeTe alloy layer at the front, which improves the bulk lifetime. Both cells were fabricated on the same day. These CdTe and CdSeTe/CdTe cells had conversion efficiencies of 14.2% and 15.6%, respectively.

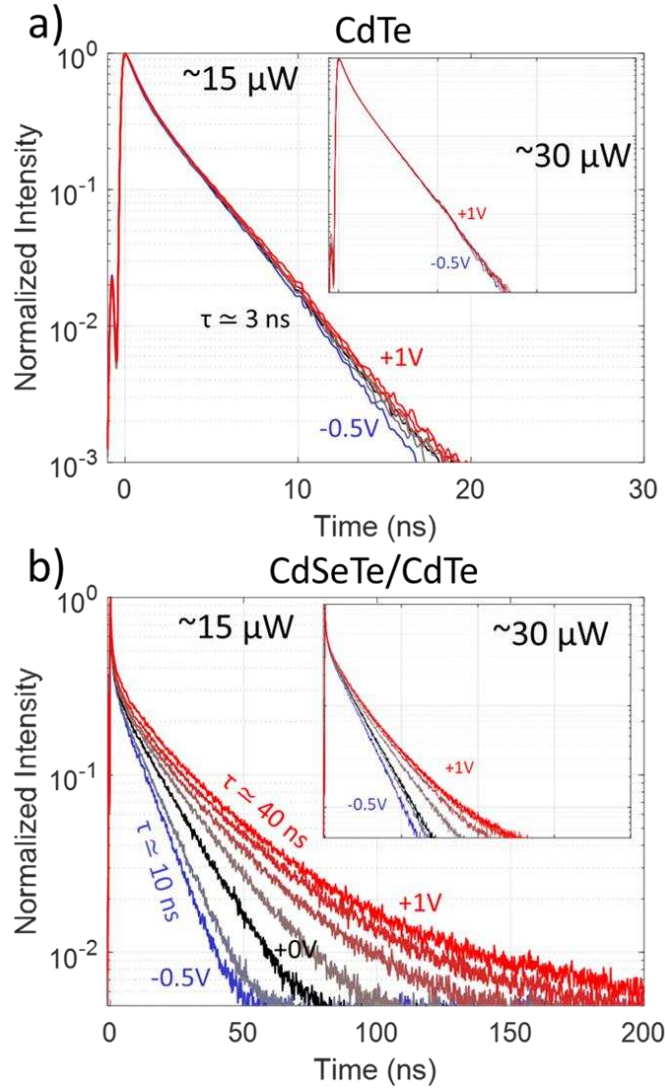


Figure 17. TRPL measurements of a) CdTe-only and b) CdSeTe/CdTe bilayer absorbers at a range of external biases. Bias has little effect on the low-lifetime CdTe cell but a substantial effect on the bilayer absorber. Insets show the same measurements at higher excitation power, demonstrating reduced influence of bias.

Figure 17a shows the effect of external bias on measured TRPL decays of the cell with the CdTe-only absorber at 15 μW ($\sim 10^{12}$ photons/pulse/cm² fluence) injection. Measurements reveal very little difference over the -0.5 V to +1 V bias range, with nearly identical single-exponential decays yielding a lifetime of ~3 ns. Although even less bias dependence is observed by increasing the injection to 30 μW (Figure 17a inset), the difference is very minor. Taken

together, as neither field manipulation with bias nor injection influence the measured lifetime, it is clear that internal fields are having a negligible effect on the measured decays. In this cell, photogenerated carriers during the TRPL measurement mostly recombine before the fields drive any significant electron-hole separation, meaning that SRH recombination is the dominant decay mechanism in this measurement, as is usually assumed.

Alloying CdTe with selenium has been shown to reduce the prevalence of bulk defects [118] and, combined with a favorable band gap and conduction band offset with CdTe, improve cell performance [119], [120]. The larger lifetime is readily visible in Figure 17b, showing the measured decays over the same range of biases for the CdSeTe/CdTe cell at low injection. In this case, a clear bi-exponential decay shape is visible, as front interface recombination at early times is no longer masked by the much faster overall decay in Figure 17a (revisited in Section 3.6.2). In addition to increased lifetime with the selenium alloy, this cell exhibits a substantial dependence on apparent lifetime with bias, with τ_2 ranging from ~10 ns to ~40 ns. As bulk material properties do not change with electrical bias, it is clear that these TRPL measurements are not solely measuring bulk material properties, but are altered by carrier dynamics. The same effect has been reported with fully-depleted Cu(In,Ga)Se₂ cells [121]. As seen in the modeling (Figure 15 and Figure 16), increasing injection power (Figure 17b inset) pushes the cell farther into forward bias locally and reduces the influence of external bias and the spread of measured lifetimes. The diode fields weakened by the higher injection are less effective at separating the carriers – further evidence that these TRPL decays are influenced significantly by field effects. As nearly identical trends are observed in both the experiment and the modeling in Section 3.4, the explanations derived from this modeling are most likely describing the observed behavior in the measured cells.

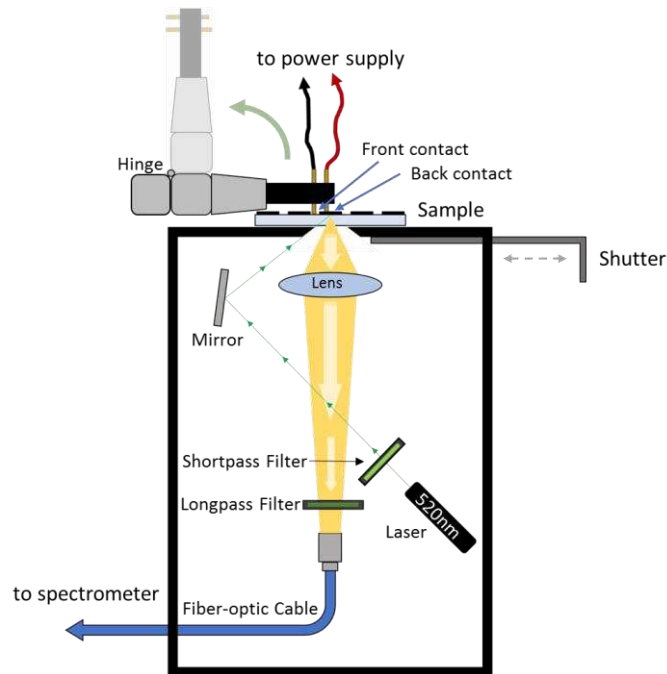


Figure 18. Schematic of steady-state photoluminescence system developed at CSU.

Spectrally-resolved steady-state photoluminescence (PL) was performed using a system designed and built at CSU for this project. A schematic of the measurement tool is shown in Figure 18. The system was designed for simplicity and low cost. To this end, the laser diode used is continuous wave, necessitating the utilized geometry with the excitation beam incident on the sample at an oblique angle. In this way, no timing electronics of any kind are required, only a simple spectrometer for signal measurement. A drawback of this design is that the sample must be at a precise height for proper focusing of the signal into the optical fiber. In practice, this means that materials must be deposited on glass of a specific thickness, which generally is not an issue when all samples are fabricated in the same lab. The short- and long-pass filters indicated have a gap of several tens of nm between their attenuation cutoffs, ensuring that no reflected signal from the laser reaches the spectrometer. To easily and quickly apply bias, a hinged arm with contact pins designed to accommodate cells fabricated at CSU can be used.

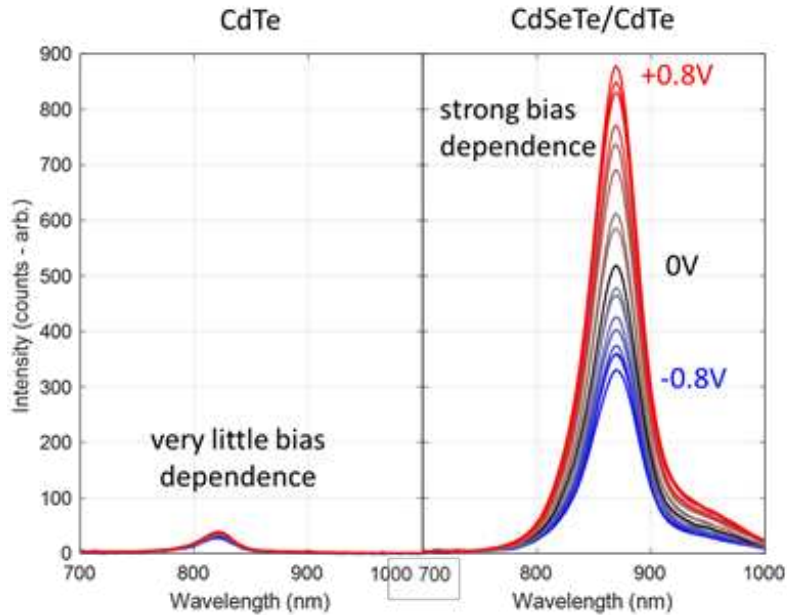


Figure 19. Steady-state photoluminescence measurements on the same cells as Figure 17. Trends in luminescence intensity seen here match trends in lifetime seen in Figure 17 very well.

Spectrally-resolved PL performed under bias on the same cell structures is shown in Figure 19. The CdTe cell has a low luminescence signal which varies very little with bias. In contrast, the CdSeTe/CdTe bilayer absorber cell has a much brighter signal which is highly bias-dependent, stronger in forward bias and weaker in reverse bias, similar to the results reported by *Shvydka et al.* [122]. The agreement in general trends between the steady-state and time-resolved measurements is very strong. This agreement is useful as it indicates that field influence can still be probed by much faster and more accessible steady-state luminescence measurements in the absence of TRPL availability.

The CdSeTe alloy used replaces ~20% of the tellurium atoms with selenium. While CdSe has a bandgap of ~1.75 eV and CdTe ~1.5 eV, the intermediate ternary CdSe_{0.2}Te_{0.8} alloy has a bandgap ~1.4 eV [123], lower than both binary materials. The CdTe cell's PL peak is at ~825 nm

while the CdSeTe/CdTe cell's peak is at ~ 875 nm, corresponding perfectly to the CdTe and CdSe_{0.2}Te_{0.8} bandgaps. This peak shift is strong evidence that the majority of detected luminescence is from the very front of the absorber, as the CdSeTe layer is only 0.5 μm thick.

Placing a cell in forward bias will introduce electroluminescence, ostensibly detectable in a measurement. In TRPL, this simply manifests as background. In spectrally-resolved steady-state PL however, the electroluminescence signal is identical to the photoluminescence signal and the two add, potentially complicating interpretation. In practice however, this effect is very small in these conditions. Electroluminescence can be evaluated by simply measuring the cell under bias without the laser excitation, and under modest forward bias ($< \sim 1$ V) the electroluminescence signal is orders of magnitude weaker than the photoluminescence signal. Electroluminescence in both samples in Figure 19 was virtually undetectable even at +0.8 V bias, so increasing PL signal with bias can be confidently attributed solely to band-flattening effects.

3.6.2 Low and High Doping

In addition to higher absorber lifetimes with the selenium alloy, recent advances in absorber doping with group-V elements both in single crystal [39], [124] and thin-film [125]–[127] materials, as well as concurrent improvement in emitter layer doping [128], [129], reflect a possible trajectory of CdTe-based photovoltaics for the future. One consequence of higher carrier density is faster carrier separation, a characteristic which is highly relevant to TRPL [85]. Carrier density therefore represents a fourth significant parameter in addition to the three discussed above (lifetime, mobility, injection), with important but less direct effects.

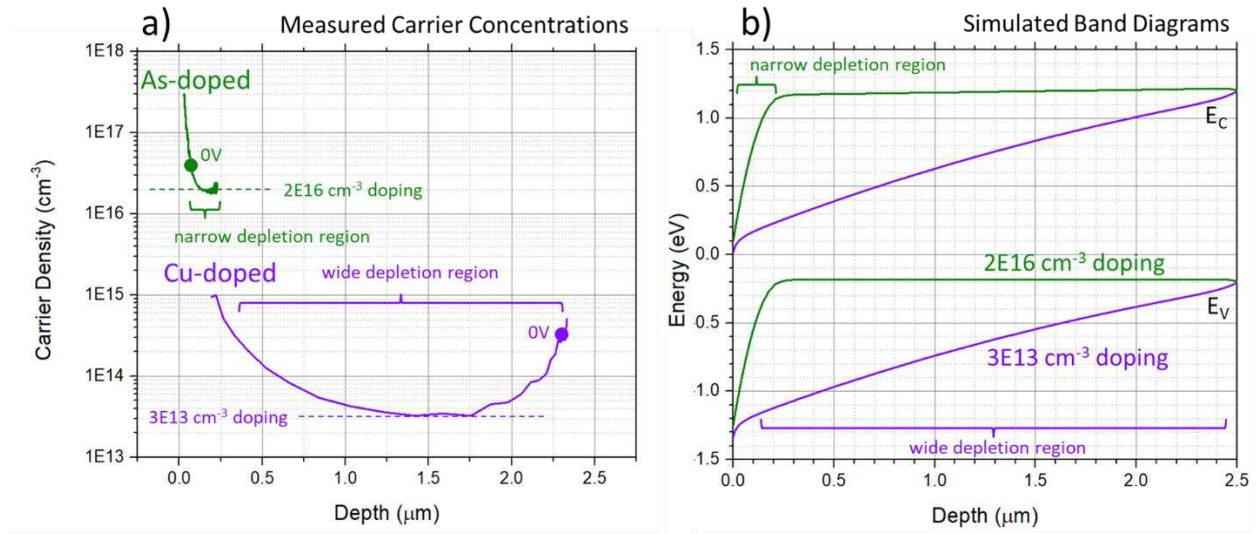


Figure 20. a) Capacitance/voltage measurements of copper- and arsenic-doped cells indicating much higher carrier concentration with arsenic doping. b) Simulated band diagrams of absorbers with the measured carrier concentrations in a p-n junction cell, indicating dramatically different depletion widths.

To investigate the influence of absorber carrier density on TRPL, biased measurements were performed on two thin-film cells with graded CdSeTe/CdTe bilayer absorbers, fabricated by First Solar Inc. Both cell structures are largely similar with high bulk lifetimes from the selenium alloying, with the crucial distinction being that one cell utilizes the traditional dopant copper, while the other is doped with arsenic for higher carrier concentration. Figure 20a shows carrier concentration profiles from capacitance-voltage (C-V) measurements of both cells, with corresponding band diagrams simulated with SCAPS in Figure 20b. From C-V, the copper-containing cell has a concentration of $\sim 3 \times 10^{13} \text{ cm}^{-3}$ and the depletion region of the cell therefore extends throughout the absorber. The arsenic-doped cell has a much higher concentration of $\sim 2 \times 10^{16} \text{ cm}^{-3}$, yielding a much narrower depletion region. The simulated band diagrams reflect this dichotomy: when carrier concentration is low and the depletion region is wide, relatively

weak fields are present throughout the absorber. Conversely, when concentration is high, very strong fields are confined to the front of the absorber while the remainder is nearly field-free.

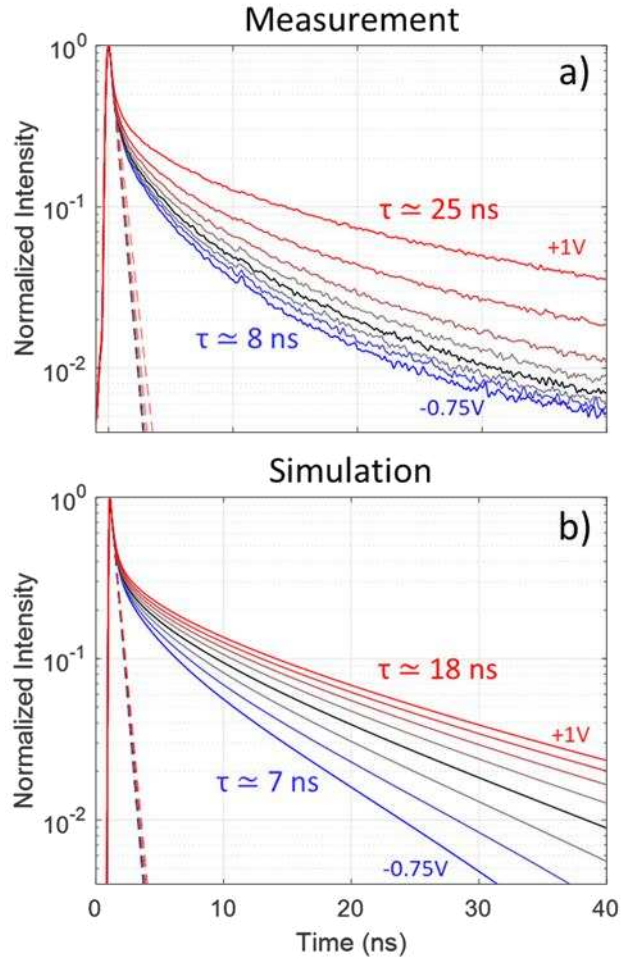


Figure 21. Early-time decay behavior in a) measured and b) simulated cells with low absorber carrier concentration. The dashed line indicates τ_1 fits, which are not affected by bias. Variation with bias appears only at later times.

Measurement and simulation for Cu-doped solar cells are discussed first. Figure 21 shows the first 40 ns of both measured and simulated TRPL decays of the lower carrier-concentration cell at a range of biases at low injection ($\sim 10^{12}$ photons/pulse/cm² fluence). The agreement between the measurement and simulation is good, and the decay times are similar to

the bilayer CSU cell in Figure 17b. Within this timescale, there are two distinct decay regions: an initial fast, bias-independent decay (indicated by dashed-line fits, lifetime τ_1) and a subsequent slower, bias-dependent decay (with lifetime τ_2). If the framework of equation (44) is applied to τ_1 , the insensitivity to bias indicates that the drift rate is insignificant over this timescale. To replicate this behavior in the simulation, the first 60 nm of the absorber (chosen somewhat arbitrarily) was given a significantly lower lifetime (0.3 ns), emulating poorer-quality material near the interface. Therefore, the short τ_1 lifetimes are attributed to increased recombination at the front interface where lattice mismatch between CdSeTe and the front buffer can create additional trap state defects [130]–[132]. Within the τ_1 decay region, the interface-associated recombination rate is much faster than all others, rendering the drift rate and bulk recombination rate inconsequential. In the simulated cell, $\tau_1 \approx 0.3$ ns for all biases, which corresponds to the 0.3-ns lifetime at the front of the absorber. In this case, the minimal bias dependence of τ_1 enables accurate determination of lifetime at the front of the cell, and therefore of front interface recombination velocity, estimated to be $S_{front} \approx 10^4$ cm/s in this cell.

The bias-dependent τ_2 decay is attributed to carriers separating in the relatively weak fields, analogous to the CSU-fabricated CdSeTe/CdTe cell described in Section 3.6.1. After carriers at the front recombine quickly, the relative lack of carriers near the interface dramatically reduces the interface recombination rate, increasing the relative influence of the drift rate at later times (>2 ns), introducing bias dependence. No τ_2 fully reaches the absorber's bulk lifetime of 30 ns in the simulated cell, indicating that some interface recombination remains in the “steady-state” decay component, also reported in simulations by *Kanevce et al.* [133]. The +1 V bias τ_2 lifetime of 25 ns in the measured cell is therefore interpreted as a close lower bound of the bulk lifetime.

Once again, mobility is an important consideration. Higher mobility will result in faster carrier separation, so drift effects will appear earlier in the decay. Under simulation conditions with high mobility CdTe ($\mu_e = 80 \text{ cm}^2/\text{Vs}$ and $\mu_h = 10 \text{ cm}^2/\text{Vs}$), *Kanevce et al.* [133] consistently attributed the first TRPL decay component (τ_1) to rapid charge separation effects while the second (τ_2) was dominated by recombination. Modeling here with much lower mobility ($\mu_e = 1 \text{ cm}^2/\text{Vs}$ and $\mu_h = 0.2 \text{ cm}^2/\text{Vs}$ in Figure 21b) essentially shows the opposite. That τ_1 in the measured copper-doped cell has no bias dependence is strong evidence that this component of the bi-exponential decay is not caused by charge separation, and therefore the effective mobility in this cell is much closer to $\sim 1 \text{ cm}^2/\text{Vs}$ than $80 \text{ cm}^2/\text{Vs}$. Analysis of biased TRPL measurements performed on Cu(In,Ga)Se₂ has revealed mobilities of $\sim 3 \text{ cm}^2/\text{Vs}$ [121] and $\sim 20 \text{ cm}^2/\text{Vs}$ [134], with similar bias dependence of τ_2 . Mobility of CSS-deposited polycrystalline CdTe has been measured in the range of 0.1-10 cm^2/Vs by both lateral Hall effect [135], [136] and longitudinal time-of-flight [137] measurements, so the similar TRPL behavior under bias observed in Cu(In,Ga)Se₂ and copper-doped CdTe is attributed to similar lifetime, mobility, and band bending in the two technologies. Note that much higher mobilities greater than $100 \text{ cm}^2/\text{Vs}$ have been measured with light-induced transient grating in single-crystal CdTe [138] and polycrystalline CdSeTe double-heterostructures [83], so there is potential for large mobility improvement in completed cells, which would yield different TRPL behavior. It should be noted that higher mobilities are more likely to cause the script to fail.

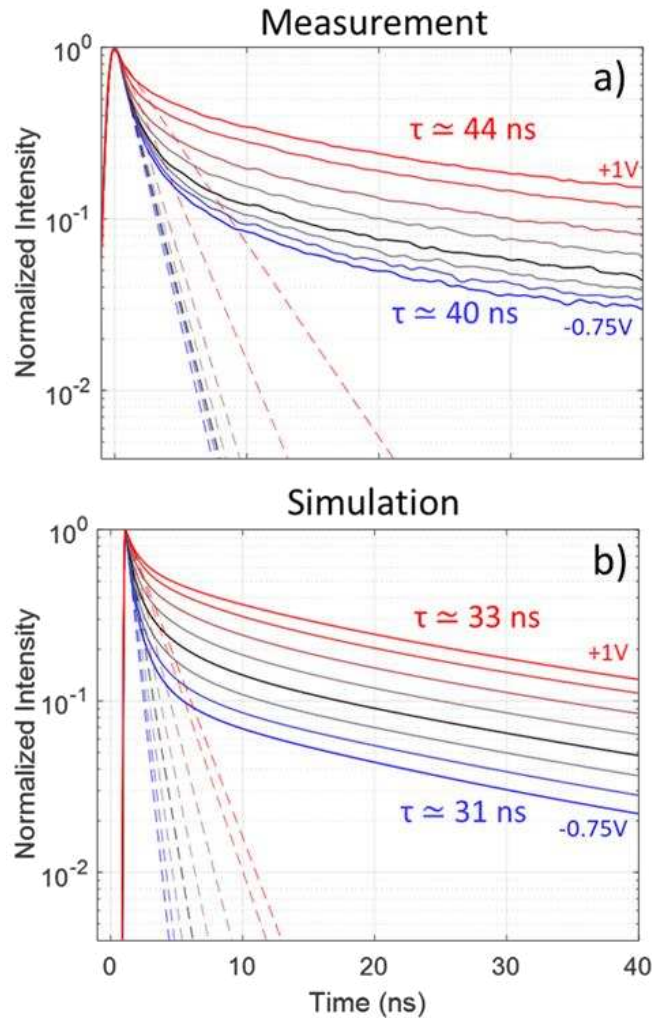


Figure 22. Early-time decay behavior in a) measured and b) simulated cells with high absorber carrier concentration. The dashed line indicates τ_1 fits, which are affected strongly by bias. At later times there is little variation with bias.

Figure 22 shows the same set of measurements and corresponding simulations for the much higher-carrier-concentration arsenic-doped cell. Stronger electric fields increase the drift rate and shift the charge separation effects to earlier decay times. As before, the 40-ns timescale contains two distinct decay rates. However, in contrast with the copper-doped cell, the initial fast decay (dashed-line fits) is bias-dependent and the slower decay component is essentially bias-independent. For a given mobility, whereas carrier separation due to drift is a fairly slow process

when carrier density is low, this process happens much more quickly when the diode field is stronger. Applying the framework of equation (44), the much faster drift rate and the interface recombination rate now both influence τ_1 . Therefore, interface recombination velocity cannot easily be derived from τ_1 in this cell. As before, this decay lifetime is shortest when fields are strongest in reverse bias. Note that τ_1 lifetimes are altogether longer in Figure 22 compared to Figure 21, indicating reduced front interfacial recombination in the absence of copper (the lifetime in the “defective region” of the simulated cell was raised to 1 ns to account for this). As the depletion region is significantly narrower when carrier concentration is high, a not-insignificant number of photoinjected carriers are generated past the depletion region, deeper within the absorber where there are no (or very weak) fields. These carriers recombine with minimal charge separation influence, resulting in minimal bias dependence in τ_2 over the timescale in Figure 22.

Although the simulation parameters used may not represent precise, unique solutions to the measured decays of both cells, it is significant that the primary decay behaviors observed in the First Solar cells are replicated by changing carrier density in the simulation. The timescale over which field effects influence TRPL decays is important information for making appropriate analysis, and carrier density is a vital determinant of this timescale.

3.6.3 Charge Storage Effect

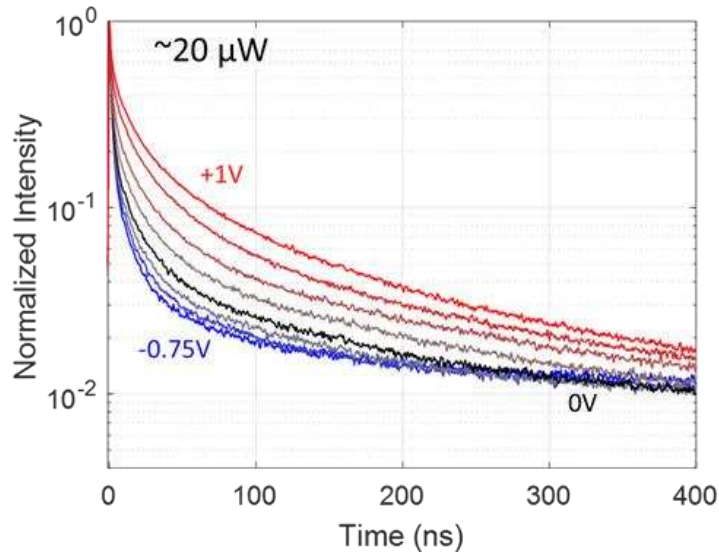


Figure 23. Same measurement as Figure 22a but over a much longer timescale. Shown this way, the tail decay rate is larger in forward bias and smaller in reverse bias, which is the opposite from what has been reported in this chapter so far. This indicates “charge storage,” a different field effect.

The time range in Figure 21 and Figure 22 was chosen to display the decay information which can be reliably accounted for with the simulation. At later decay times deviations between the experiment and the simulation appear. Measured decays of the arsenic-doped cell exhibit very long tail lifetimes (Figure 23) which do not appear the same way in the simulation. These long tails are likely explained by charge segregation where photogenerated carriers are swept apart by junction fields and eventually reach a new equilibrium where electrons are heavily concentrated near the front of the cell and holes are concentrated towards the back. In this new equilibrium, the remaining carriers recombine very slowly due to their physical separation, yielding a time constant well in excess of the bulk lifetime. This process is referred to as “charge storage” in *Maiberg and Scheer* [111], and simulations exhibiting this behavior are described in that manuscript.

How charge storage is manifested is very sensitive to simulation conditions. *Maiberg and Scheer* [111] assert that it would be undetectable during measurements because the amount of luminescence is too low. Simulations presented in this chapter, however, found that charge storage could be made visible (i.e. within three orders of magnitude of luminescence intensity) when fields were weakened with large enough forward bias, but were less visible when fields were stronger, as more effective carrier separation yielded less (and ultimately undetectable) radiative recombination at the final equilibrium. *Moseley et al.* [139] were able to repeatedly demonstrate detectable charge storage effects, particularly at low excitation intensities. In agreement with the modeling presented here, *Moseley et al.* [139] demonstrate that charge storage is more prevalent when absorber doping is high, though it can still be observed with lower doping if other conditions are met. As charge separation and storage effects on TRPL have only recently started to be explored with simulation, many questions remain, particularly regarding its applicability to measured data.

Unlike the single pulse dynamics which are modeled in the simulation, the decay shape of an actual TRPL measurement combines measured recombination photons from millions of laser pulses. This difference can lead to substantial deviation in late-time decays between measurement and simulation. In particular, incomplete recombination between pulses effectively amplifies the tail decay signal and reduces the dynamic range of the measurement, as in Figure 23. Remedying this discrepancy by simulating multi-pulsing over a large enough number of pulses to approximate experimental conditions is prohibitively computationally expensive, so replicating the charge-storage effect in detail with modeling remains difficult. Charge storage can be mitigated experimentally to some degree by employing lower laser repetition rates, allowing more time for carriers to recombine between pulses and better aligning simulation and

experiment. However, the repetition rate can only be reduced so far before it becomes infeasible. Charge storage can therefore exert significant influence on long tail lifetimes of measured decays, and using modeling to decouple its contribution presents a challenge.

3.7 Conclusion

In conclusion, modeling and measurements incorporating electrical bias have revealed that time-resolved photoluminescence is a powerful tool which is affected by many processes. As a dynamic measurement, TRPL is sensitive to fields and allows different recombination pathways which operate under different timescales to be visible. While this potentially allows access to a wide range of valuable information about cell components in isolation through intelligent analysis and experiment design, it also makes interpretation much more difficult, as care must be taken to deconvolute the different contributors. Interpretation of TRPL performed on completed cells is especially fraught, and unfortunately the same cell attributes which lead to good performance (high lifetime, high mobility, high doping) are the same which complicate interpretation.

It is possible, however, to eliminate field effects from the measurement. Measuring with a higher excitation power introduces more carrier pairs which locally flattens the bands and reduces or even eliminates completely the field contributions, as demonstrated in Section 3.4. However, while this method is simple and effective, increased photogenerated carrier density increases the rate of radiative recombination, which introduces an additional recombination contribution which can skew the results, also demonstrated in Section 3.4. A more difficult but superior method is measuring under forward electrical bias, which can entirely suppress fields in a more controllable and predictable way *without* introducing other errors.

In addition to identifying some significant measurement challenges and describing methods to address these challenges, the main goal of this work is to inform the CdTe community that simple τ_2 extraction of TRPL data is no longer sufficient. CdTe technology has reached a state of maturity whereby TRPL measurements are affected by much more than just SRH recombination in the bulk, and results should be carefully interpreted and verified by other measurements.

CHAPTER 4. N-I-P STRUCTURE TO IMPROVE VOLTAGE

As the previous chapter has hopefully made clear, luminescence measurements such as TRPL, while potentially difficult to perform and interpret, can provide critically important information that cannot be accessed any other way. Recombination kinetics are fundamental to photovoltaic operation, so understanding these processes in the devices and materials under study is critical. The ability to perform measurements on incomplete cells is extremely valuable, as recombination can be assessed at every step in the fabrication process, potentially revealing that one or several particular treatments or depositions are detrimental, though they may be necessary in the employed cell design.

This chapter begins with reports of luminescence measurements performed by others which indicate that open-circuit voltages exceeding 1 V are possible with polycrystalline materials which already exist. If this potential were realized, it would represent a paradigm shift in the CdTe community, overcoming a stubborn, >50 year-old performance limitation. A new cell architecture is proposed which aims to leverage these materials, enabling high selectivity without compromising their impressive luminescence characteristics. Extensive modeling is performed to both prove the new structure's feasibility and identify the most important parameters and corresponding values required for maximizing performance. Preliminary experimental results are presented, and promising research directions for the future are identified.

4.1 ERE Measurement, and Potential of CdSeTe

This section presents an overview of recent work performed by other researchers which motivates the investigations in this chapter; the measurements and derivations in this section are referenced to their respective sources.

External radiative efficiency (ERE) is a variation of the steady-state photoluminescence measurement which is used to quantify non-radiative recombination losses [140]. As a photoluminescence technique, an ERE measurement involves injection of light into a photovoltaic material and detection of the emitted photons from the illuminated surface. Though there are details which make the execution less trivial, the concept of the measurement is quite simple: ERE is essentially a ratio of the number of radiatively-emitted photons to the number of injected excitation photons. This essentially gives the proportion of radiative to nonradiative recombination occurring inside the material. From Würfel's expansion of the Planck law to non-thermal radiation [141], a relationship between this quantity and the quasi-Fermi level splitting (QFLS, see Section 2.3) can be derived [142], [143]. This relationship is more conveniently described with a useful parameter called the **implied voltage** iV_{OC} , which is directly related to the QFLS by [143]:

$$QFLS = q * iV_{OC} \quad (45)$$

The relationship between iV_{OC} and radiative efficiency is given by:

$$iV_{OC} = V_{OC,ideal} + \frac{kT}{q} \ln(ERE) \quad (46)$$

where $V_{OC,ideal}$ is the maximum attainable voltage of the absorber material, chiefly a function of its bandgap. This theoretical voltage limit determined by detailed balance analysis is given by [142]:

$$V_{OC,ideal} = \frac{kT}{q} \ln \left(\frac{\int \alpha(\lambda) \phi_{exc}(\lambda) d\lambda}{\int \alpha(\lambda) \phi_{BB}(\lambda, T) d\lambda} + 1 \right) \quad (47)$$

where α is the sample's absorptance, ϕ_{exc} is the excitation photon current, and ϕ_{BB} is the photon flux of a black body at temperature T [144]. At standard conditions ϕ_{exc} is the AM1.5 spectrum and ϕ_{BB} is the photon current of a black body at 300 K, both independent of the absorber

material's properties. $V_{OC,ideal}$ therefore is functionally dependent only on the absorptance of the material. Chiefly this means the material's bandgap, but $V_{OC,ideal}$ can also be influenced particularly strongly by sub-bandgap absorption and band tails [145].

Implied voltage represents the V_{OC} which would be attained in a cell utilizing the measured materials with perfect selectivity; as such, iV_{OC} essentially describes the voltage capabilities of the materials. The ERE measurement is incredibly useful as it quantifies voltage losses into two distinct, important categories. A cell's voltage deficit is determined by radiative efficiency and selectivity, and ERE handily separates these two factors. The difference between the $V_{OC,ideal}$ and iV_{OC} are losses due to nonradiative recombination, while the difference between iV_{OC} and measured V_{OC} are losses due to imperfect selectivity. This turns out to be a very useful distinction. Recombination losses are largely an issue of material quality, while selectivity losses are largely an issue of cell design. Determining which is limiting voltage is crucial for making informed research decisions.

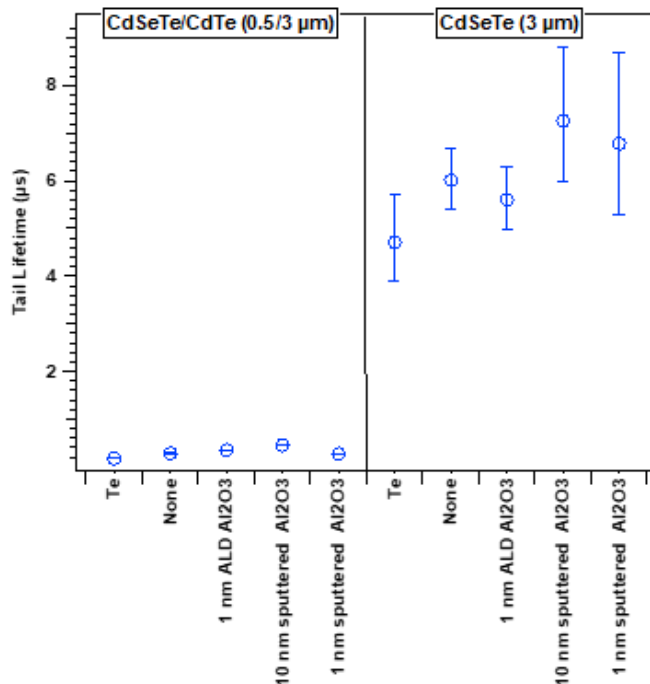


Figure 24. Measured lifetimes of several CdSeTe and bilayer CdSeTe/CdTe absorbers with different back layers. Lifetimes are approximately an order of magnitude higher with the CdSeTe-only absorber, and are much higher than lifetimes typically measured in polycrystalline CdSeTe/CdTe cells. Taken from [146].

Recent measurements at the National Renewable Energy Lab and Arizona State University on cells and absorbers fabricated at Colorado State University have revealed very high lifetimes and EREs of CdSeTe absorbers deposited by close-space sublimation, particularly the CdSe_{0.4}Te_{0.6} alloy [146]. Figure 24 demonstrates tail lifetimes from TRPL in excess of 5 μs for CdSeTe films with various back contact layers. While Al₂O₃ provides the best interface passivation, even a bare CdSeTe interface has been sufficient for >6 μs, orders of magnitude higher than what is observed in typical CdTe cells. Note that these structures have no p-n junction, so no charge storage field effects are artificially increasing the measured lifetime. Similar samples incorporating a CdSeTe/CdTe bilayer absorber exhibit much lower lifetimes of <500 ns, on par with the highest lifetimes measured in state-of-the-art cells. Clearly, the CdTe

layer is responsible for large amounts of nonradiative recombination and is greatly detrimental to the absorber’s luminescence efficiency. Selenium has been demonstrated to passivate or prevent the formation of bulk defects in CdTe [147], and these results demonstrate just how significant this effect can be.

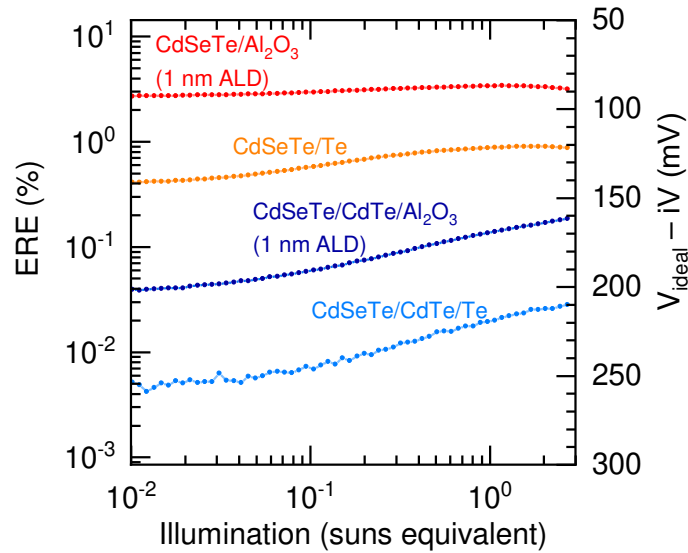


Figure 25. Measured ERE yielding $V_{OC,ideal} - iV_{OC}$ for several CdSeTe and bilayer CdSeTe/CdTe absorbers with different back layers. CdSeTe ERE is ~2 orders of magnitude higher than with CdSeTe/Te, corresponding to ~115 mV higher implied voltage. Taken from [146].

ERE measurements performed on these same samples reveal radiative efficiencies approaching 3% in the best cases, shown in Figure 25. This is a very high number for polycrystalline materials. For context, this is superior to nearly all other photovoltaic technologies, exceeded only by GaAs and on par with InGaP, crystalline Si, and some recent perovskites [148]–[150]. Much of this luminescence comes from sub-bandgap radiation – examples are shown in *Onno et al.* [142] but this phenomenon is observed very consistently in CdSeTe [147]. The source of this low-energy radiation needs to be investigated, as there are no

definitive explanations as of this writing. However, even taking the associated reduction of $V_{OC,ideal}$ into account, these measurements indicate an iV_{OC} greater than 1 V. Once again, the deleterious effects of CdTe are easily observed, reducing ERE by nearly two orders of magnitude.

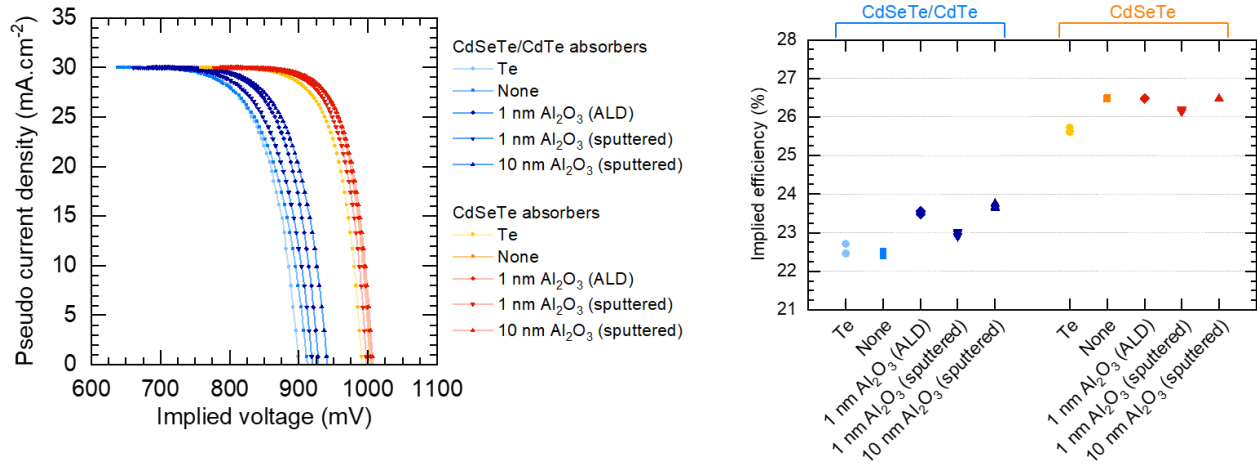


Figure 26. SunsERE measurement showing implied J-V curves and corresponding implied efficiencies for CdSeTe and bilayer CdSeTe/CdTe absorbers with different back layers. CdSeTe-only absorbers have significantly higher implied efficiencies than CdSeTe/CdTe bilayers. Taken from [146].

By modulating excitation light intensity and measuring ERE as a function of that, it is possible to create a pseudo J-V curve which gives a hypothetical cell's performance based only on its material properties, a process known as SunsERE [145]. Implied J-V curves and corresponding efficiencies for the aforementioned cells are shown in Figure 26. These results indicate that the CdSeTe absorber material is of sufficient quality to attain >26% conversion efficiency, a huge improvement in CdTe technology if realized. The presence of CdTe is again shown to reduce the potential performance by several percent absolute.

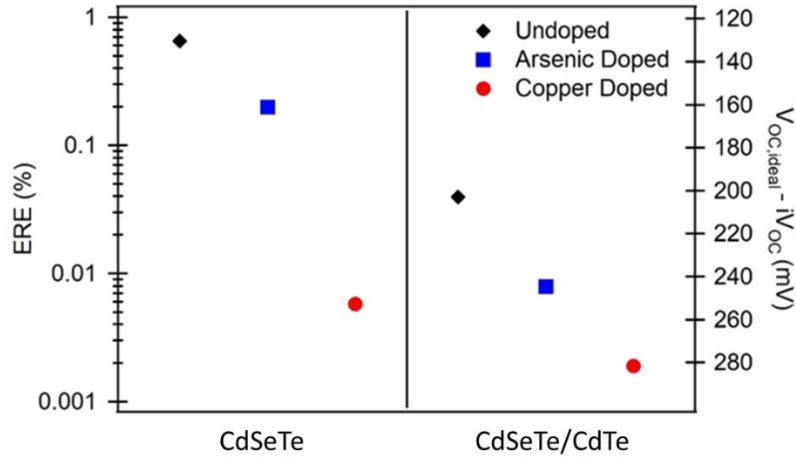


Figure 27. Measured ERE yielding $V_{OC,ideal} - iV_{OC}$ for several cells with CdSeTe and bilayer CdSeTe/CdTe absorbers with Cu doping, As doping, and no doping. Undoped CdSeTe has the highest implied voltage, over 150 mV higher than the traditional Cu-doped CdSeTe/CdTe absorber structure. Taken from [146].

The highest ERE measurements on CdSeTe samples have come from undoped material. This is intuitive, as achieving 100% dopant activation is virtually impossible, and any un-activated dopant atoms will become defects [39]. Figure 27 reports ERE measurements performed on a set of complete cell structures, with MgZnO as the front contact and Te as the back contact for each [146]. These do not represent champion ERE values by any means, but these six data points clearly and concisely communicate the main conclusions of the recent work on ERE measurements of CdTe-based materials. CdSeTe is universally better than CdSeTe/CdTe and especially CdTe. Higher-activation arsenic doping is better than copper doping, and undoped material is the best of all. In terms of ERE, traditional state-of-the-art Cu-doped CdSeTe/CdTe absorbers are nearly three orders of magnitude behind undoped CdSeTe, with a corresponding reduction of over 150 mV in iV_{OC} . Of course, the undoped CdSeTe cell shown here was not a

functioning photovoltaic device as determined by measured performance, but the J-V curve by itself hides the enormous potential revealed by the ERE measurement.

This groundbreaking body of work clearly identifies an important research path for CdTe photovoltaics. Traditionally, selectivity has been achieved through p-type doping of the absorber – separation of carriers at the p-n junction and preferential conduction of holes through the absorber’s bulk is reasonably effective at keeping electrons away from the back contact. While this strategy has yielded very low selectivity losses, it has come with a severe penalty to radiative efficiency, limiting voltage to the ~860 mV limit which has persisted for so long. Improvements in dopant activation may nudge this limit marginally higher with great effort, but this cell architecture is fundamentally recombination limited [151] and incapable of significant gains. A different approach is needed. Since ERE directly determines iV_{OC} , and a cell’s V_{OC} can never exceed its iV_{OC} , it seems apparent that the direction of future research should focus on absorber materials with the highest measured ERE. A fundamental rethink of cell architecture which aims to leverage the enormous potential of these undoped materials is the way forward. The challenge is to achieve high selectivity while preserving lifetime.

4.2 n-i-p Structure Overview

A targeted approach to achieve high selectivity with an undoped absorber is with an n-i-p cell architecture. In such a structure, a thicker intrinsic absorber layer is sandwiched between two thinner n- and p-type contact layers. A schematic of this structure and associated band diagram are given in Figure 28 and Figure 29. The n- and p-type materials induce junction fields within the absorber, helping to separate photoinjected carriers. The absorber is therefore inherently fully depleted. This depiction intentionally utilizes two heterojunctions, as strategic band offsets are

invaluable for achieving high selectivity in this configuration [50], as will be demonstrated in this chapter.

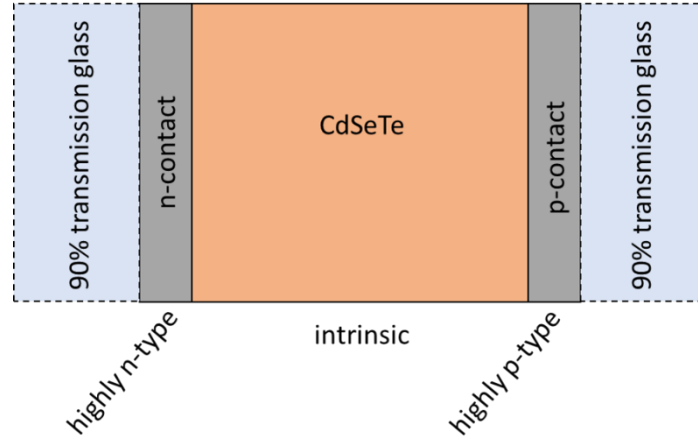


Figure 28. Structure of n-i-p cell utilizing a CdSeTe absorber. This is the simplest, ideal configuration, whereby the n- and p-contacts are comprised of single transparent materials, allowing for bifaciality. In practice, the n-contact is likely to be a bilayer of a transparent conducting oxide contact and a wide-bandgap n-type passivating buffer layer, while the p-contact may be a bilayer of a wide-bandgap p-type material and a metal.

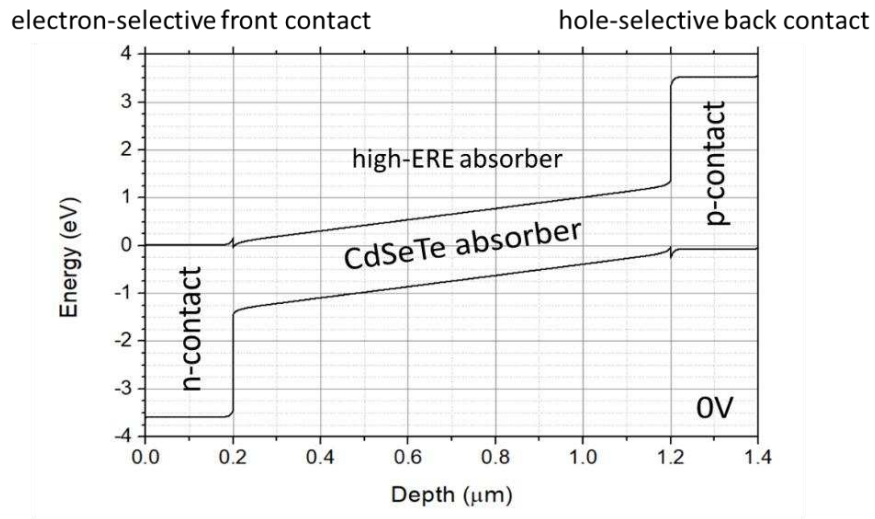


Figure 29. Band diagram of ideal n-i-p cell utilizing a CdSeTe absorber at 0 V bias. The n-contact forms a perfectly selective electron contact while the p-contact forms a perfectly selective hole contact. The potential difference between the contacts at 0 V helps push the carriers towards their correct contact within the absorber, improving selectivity. The thin absorber minimizes voltage loss. This is the basic structure used in all modeling discussed here.

Relying on a p-type absorber for selectivity is problematic for reasons in addition to the reduction of implied voltage. The requirements of this layer are numerous: the material must have strong absorption of light, must have good transport characteristics, must be of high quality to limit recombination, must have high p-type doping to create diode fields of sufficient strength, and must be robust to several subsequent depositions and treatments in the cell fabrication process. Satisfying all of these conditions simultaneously is nearly impossible, as the fulfillment of some directly negatively impacts others (in particular, high doping and high lifetime [69]). In an n-i-p structure, tasks are better compartmentalized, and important cell requirements are distributed between multiple materials, lessening the burden on each.

A p-i-n diode is of course not a new concept. It was invented in 1950 [152] with the intention of improving sensitivity to longer wavelengths by increasing the depletion region width. As such this architecture has applications in radio frequency and microwave photodetectors, switches and attenuators; it is also the standard configuration for thin-film amorphous silicon solar cells [153], [154]. The structure is even familiar to CdTe as it is often used in radiation detectors [155], though photovoltaic applications are almost nonexistent (see Section 4.5.2). Modeling studies have reported excellent photovoltaic performance using ideal, nonspecific materials [50]. The aim of this work is to assess feasibility with CdTe-based materials in particular, and to discern what exactly is necessary to achieve $>1 \text{ V } V_{OC}$ with this architecture.

The three components of this cell structure are designated the **n-contact**, **absorber**, and **p-contact**. The absorber is responsible only for conversion of solar photons into electron-hole pairs and for allowing high QFLS by means of low nonradiative recombination. The n- and p-contacts are responsible only for being highly conductive and selective to electrons and holes,

respectively. High transparency to solar radiation is preferable in these contact layers as the minority carrier concentration stays very low even under illumination [50], virtually eliminating recombination in these materials and improving selectivity. Additionally, with transparent contact and electrode layers, the symmetry of the structure and fully depleted absorber naturally allows for a high degree of bifaciality.

Rather fortuitously, the standard $\text{SnO}_2\text{:F/MgZnO}$ front contact used in most cells fabricated at CSU already appears ideal for this application, with high transparency afforded by the $>3\text{-eV}$ bandgaps, excellent electron-selective band alignment, and formation of a highly-passivated interface with CdSeTe [113], [145]. In fact, all $>1\ \mu\text{s}$ lifetimes and $>1\%$ ERE reported in the previous section are CdSeTe deposited on $\text{SnO}_2\text{:F/MgZnO}$ [146]. The front contact in the simulated structure is therefore implemented as $\text{SnO}_2\text{:F}$ for all simulations in this chapter. The MgZnO layer is not included for simplicity, but since its purpose appears to primarily be interface passivation, the simulated structure essentially represents $\text{SnO}_2\text{:F/MgZnO}$, as interface recombination is not included in the model. The absorber is implemented as CdSeTe, with variation of a few significant parameters to both guide cell design and determine which CdSeTe material properties are most important. As the p-contact represents an as-yet unidentified material, its explorable parameter space is the largest. The aim with this layer is to identify a suitable material based on the important characteristics identified in the modeling.

4.3 Absorber Requirements

To evaluate which parameter values are necessary for maximizing performance, a cell structure utilizing an “ideal” p-contact is used. What constitutes an ideal p-contact is discussed in Section 4.4. As the absorber material under consideration is $\text{CdSe}_{0.4}\text{Te}_{0.6}$, it is appropriate to constrain some simulation parameters to match this material. This includes functionally

immutable properties such as the bandgap, electron affinity and absorption coefficient. Parameters which are potentially variable or manipulatable include lifetime, carrier mobility, thickness, and carrier concentration. As undoped material yields the highest lifetime experimentally, an intrinsic absorber was modeled with small and equal concentrations of both carrier types. As most carriers are generated at the very front of the absorber and the n-contact is at the front, electrons have on average a very small distance to travel; as such, electron mobility was found to have relatively little effect, and so will not be further discussed. All fixed parameter values used in the modeling are given in Table 2. This leaves lifetime, hole mobility, and thickness, all three of which have significant effects on performance and some degree of interdependence.

Table 2. Fixed parameter values for the modeled CdSeTe absorber.

Fixed CdSeTe absorber modeling parameters		
Quantity	Symbol	Value
bandgap	E_G	1.4 eV
electron affinity	χ	4.3 eV
relative permittivity	κ	9.4
carrier thermal velocity	v_{th}	10^7 cm s^{-1}
electron mobility	μ_e	$10 \text{ cm}^2 \text{V}^{-1} \text{s}^{-1}$
donor density	N_D	10^{13} cm^{-3}
acceptor density	N_A	10^{13} cm^{-3}
defect cross-section	σ	10^{-11} cm^2
surface recombination velocity	$S_{front} ; S_{back}$	10^0 cm s^{-1}

4.3.1 Lifetime

As the absorber is a conduit in which carriers move to their respective contacts for collection, recombination in this material is expected to be vitally important. Figure 30 shows simulated J-V curves of the n-i-p structure over a wide range of absorber lifetimes, with hole

mobility $1 \text{ cm}^2/\text{Vs}$ and absorber thickness $1 \text{ }\mu\text{m}$. J_{SC} is generally unaffected, until it suffers heavily at very low lifetime; this effect is explored in Section 4.3.3 below. The impact of lifetime on voltage is predictable and straightforward, losing approximately $115 \text{ mV } V_{\text{OC}}$ for each order of magnitude lifetime reduction. As indicated by equation (16) in Section 2.3, QFLS depends on $\ln(np)$. As equilibrium concentrations of both carrier types are very low in the undoped absorber, n and p both directly represent the concentrations of photoinjected carriers nearly everywhere in the absorber. Therefore, a $10\times$ reduction in lifetime applies to *both* carriers, leading to a $100\times$ reduction in the np product. The voltage loss therefore is:

$$\Delta iV_{\text{OC}} = \frac{kT}{q} \ln(100) \approx 119 \text{ mV} \quad (48)$$

Figure 31 shows the band diagrams at V_{OC} corresponding to the J-V curves. The approximately 0.1-eV difference in QFLS between each $10\times$ increase in lifetime is clearly visible.

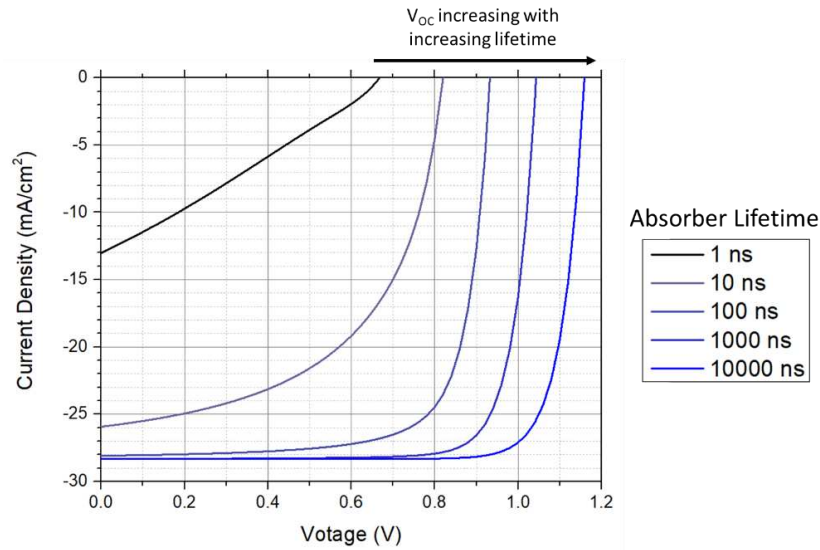


Figure 30. Simulated J-V curves of n-i-p structure over a large range of absorber lifetimes.

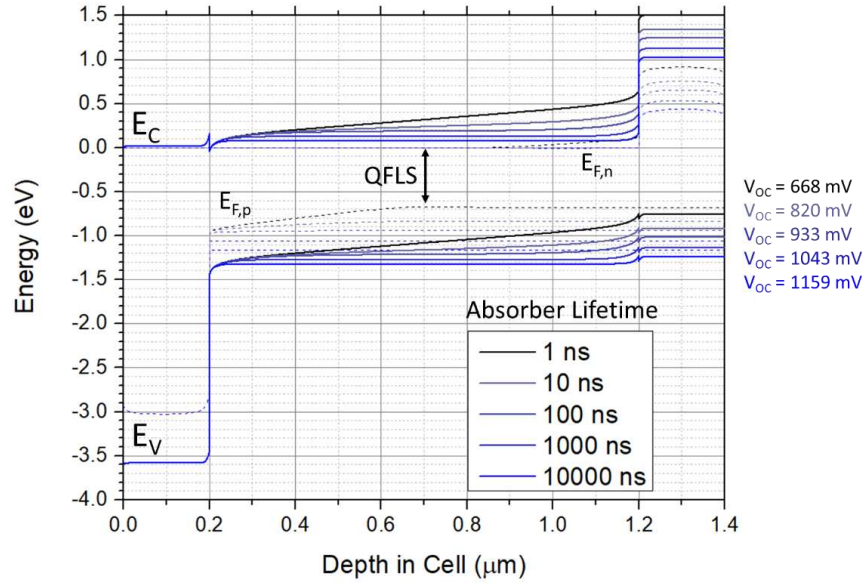


Figure 31. Band diagrams at V_{OC} of n-i-p structure over a large range of absorber lifetimes. The increase of QFLS with lifetime is clearly visible. V_{OC} corresponding to each curve is indicated; ~110-120 mV V_{OC} is gained for each order of magnitude increase in lifetime.

Figure 30 effectively demonstrates this architecture’s reliance on high lifetime. The 1-ns absorber lifetime shown here attains only ~2% conversion efficiency with 668 mV V_{OC} . p-doped CdTe cells decades ago could achieve nearly 850 mV V_{OC} with lifetimes this low [95]. This is in large part due to the QFLS in this structure being determined entirely by lifetime; in a sufficiently p-type absorber, the equilibrium hole concentration would be larger than the photoinjected hole concentration at most places within the absorber, so a 10x reduction in lifetime would cause only $\Delta iV_{OC} = \frac{kT}{q} \ln(10) \approx 60$ mV voltage loss. Unsurprisingly then, the modeling shows that lifetime is a decisive parameter in this cell architecture, and the higher the lifetime the better. It is worth emphasizing however that lifetimes do not need to be unrealistically high to attain record-breaking performance; Figure 30 indicates the potential for >24% efficiency using material parameters which have already been measured experimentally.

A note on how lifetime is implemented in this application. As with the TRPL modeling in Chapter 3, SRH recombination is implemented with a single midgap defect. The defect cross-section is held constant at 10^{-11} cm^2 and the defect density is varied to attain the desired bulk lifetime (see equation (39)). Although SCAPS can include recombination from many pathways, lifetime was deliberately specified with trap-mediated Shockley-Read-Hall (SRH) recombination only, with no interface recombination and especially no radiative recombination ($B = 0$). This simplification ensures that the lifetime used in the model corresponds most directly with whatever would be measured in an experiment. Radiative recombination lifetime is given by:

$$\tau_{rad} = \frac{1}{(1 - \gamma)B(n_0 + n_{exc})} \quad (49)$$

where B is radiative recombination coefficient, n_0 and n_{exc} are the equilibrium and photoexcited carrier concentrations, and γ is photon recycling factor [156], [157]. As the radiative lifetime is dependent on illumination intensity (and varies throughout the absorber as absorption is not uniform), it is impossible to give one single number. However, assuming an excited carrier concentration of 10^{15} cm^{-3} with much lower doping concentration (nominally 10^{13} cm^{-3}) and no photon recycling, CdTe (and by extension CdSeTe)'s radiative recombination coefficient of $10^{-10} \text{ cm}^3\text{s}^{-1}$ [82] yields a radiative lifetime $\sim 10 \mu\text{s}$, which is used here as the upper bound of attainable lifetime in this material under 1-sun illumination.

Without radiative recombination, the SRH lifetime in the model can be increased indefinitely and the simulation will continue to output higher and higher V_{OC} far above the Shockley-Queisser limit. However, if $10 \mu\text{s}$ is considered the rough upper bound of acceptable lifetime in the parameter space, the model still represents a good approximation of reality. A $10\text{-}\mu\text{s}$ SRH lifetime *without* radiative recombination is more or less equivalent to an infinitely high SRH lifetime *with* radiative recombination (simulated performance is very similar). However, as

radiative lifetime is dependent on excess carrier concentration and SRH lifetime is not, behavior near this “radiative limit” starts to become unreliable – for this reason, voltages indicated in Figure 30 and Figure 31 at 10 μs lifetime are likely slightly too high. A measured lifetime in a physical material will have contributions from all potential recombination pathways, conveniently weighted by whichever pathways are most important. Without deeper analysis, such a measurement will provide no indication of what τ_{SRH} is in the bulk specifically, for instance, but this information is actually not particularly useful in the context of determining QFLS. Therefore, implementing SRH lifetime as a proxy for measured lifetime arguably makes the model more useful, as long as interpretation at or near the radiative limit is done with appropriate skepticism.

One final note: the rate of radiative recombination itself does not actually influence iV_{OC} , only the relative proportion of nonradiative to radiative recombination does. The $\sim 10 \mu\text{s}$ radiative lifetime is significant only in the context of the values used for the density of states of the valence and conduction bands; it merely represents the radiative recombination limit when iV_{OC} is maximized for *this particular material*. The radiative recombination coefficient is determined using detailed balance for each specific configuration, but a general expression for an absorber in a solar cell with a perfect backside mirror is [157]:

$$B = \frac{2\pi}{n_i^2 h^3 c^2} \int_{E_G}^{\infty} E^2 \alpha(E) \exp\left(-\frac{E}{kT}\right) dE \quad (50)$$

Functionally then, B is a function of absorption α and the intrinsic carrier concentration n_i , which is itself a function of the density of states [36], [157]:

$$n_i^2 = N_C N_V \exp\left(-\frac{E_G}{kT}\right) \quad (51)$$

τ_{rad} and QFLS are *both* then dependent on N_C and N_V (see equation (16)), so a material with a fast radiative lifetime will necessarily have larger QFLS for a given np product – they are inextricably linked. In general, τ_{rad} itself says nothing about radiative losses or suitability as a semiconductor. In fact, some optoelectronic applications *require* materials with high radiative efficiencies and very short radiative lifetimes [158], [159].

4.3.2 Hole Mobility

As holes excited mainly near the front interface must travel the entire length of the absorber before reaching their designated contact, hole mobility is expected to be important. Figure 32 shows simulated J-V curves of the same structure over a wide range of hole mobilities, with lifetime 1 μ s and absorber thickness 1 μ m. While there are trends, there are no clear definitive relationships comparable to the consistent voltage loss observed in Figure 30. Smaller mobilities appear to correspond with reduced fill factors, though there is little difference between 1 cm^2/Vs and 10 cm^2/Vs . V_{OC} and J_{SC} appear generally unaffected by mobility, except in the extreme case of 0.01 cm^2/Vs where the fill factor is so low the diode behavior almost disappears. Mobility clearly has some significance, but no directly attributable consistent effects on its own; it is thus better analyzed in the context of a different parameter.

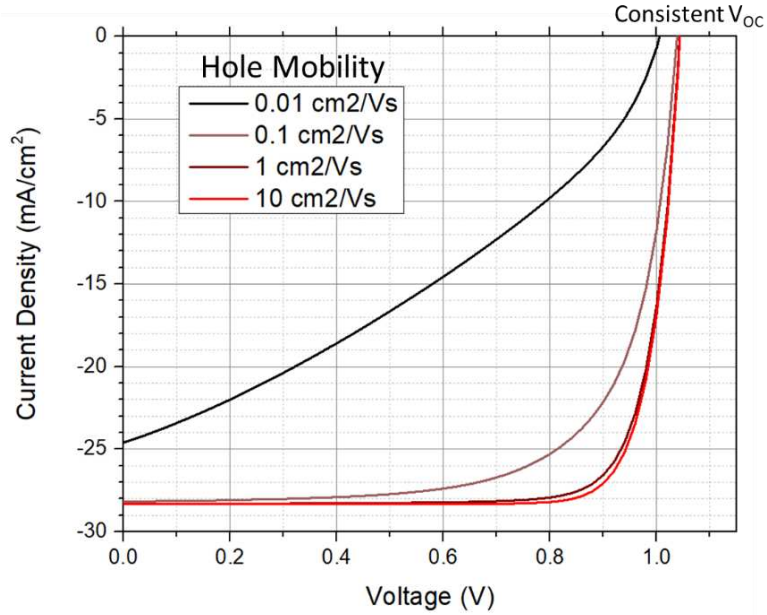


Figure 32. Simulated J-V curves of n-i-p structure over a large range of absorber hole mobilities.

4.3.3 Diffusion Length

Mobility is effectively a “velocity.” A far more useful parameter would be a lengthscale, which can handily be derived from mobility and lifetime. An appropriate parameter is the so-called hole **diffusion length**:

$$L_{D,h} = \sqrt{D_h \tau} \quad (52)$$

where τ is the lifetime and D_h is the hole diffusion coefficient, based on hole mobility (see Section 3.3.1). The diffusion length represents the average distance a carrier (hole) moves before it recombines. Hereafter the diffusion length will simply be referred to as L_D , with the implicit understanding that it is referring to holes.

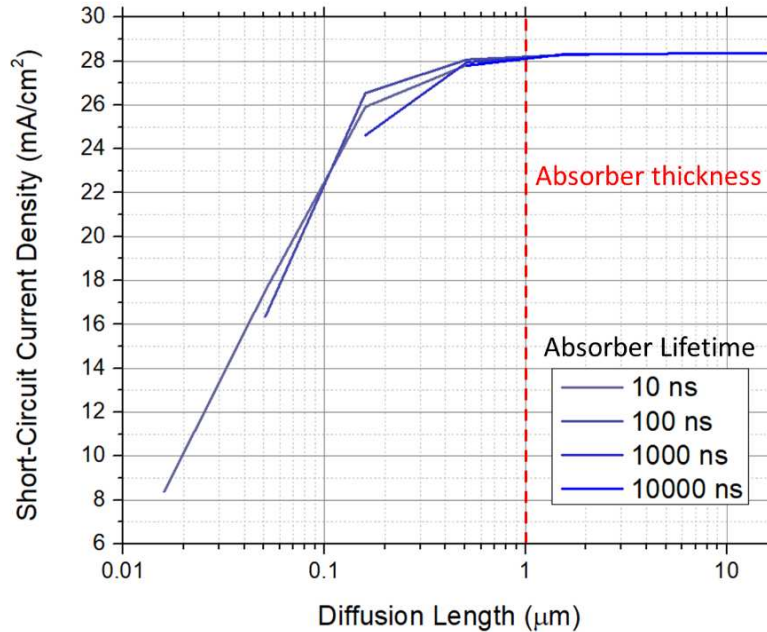


Figure 33. Short-circuit current density as a function of hole diffusion length for simulated 1- μm -absorber n-i-p structure. A wide range of absorber lifetimes is necessary to cover the wide range of diffusion lengths, indicated with different shades of blue. When $L_D \geq L$, current is maximized. When $L_D < L$, current decreases.

Figure 33 shows simulated short-circuit current density as a function of diffusion length. Lifetimes ranging from 10 ns to 10 μs are used to cover the large range of diffusion lengths represented; curves utilizing the different lifetimes are represented with different colors. The fact that these curves overlap quite well is a good indication that diffusion length as a parameter has special significance in this context. This plot clearly indicates that maximum short-circuit current is attained when $L_D \geq L$ (L is absorber thickness, 1 μm in this illustration). When $L_D < L$, current collection is increasingly impeded. There is an intuitive explanation for this result: when $L_D \geq L$, the vast majority of holes are statistically expected to travel the entire distance of the absorber and be collected at the back contact. When $L_D < L$, many holes are expected to recombine before they reach the back contact, at which point they do not contribute to current.

This relationship can be explained more rigorously using the description of J_{SC} from Würfel [36]. At the radiative limit, the short-circuit current is determined by the total excitation photon current absorbed within the diffusion length or the absorber thickness, whichever is shorter [36]. This can be quasi-quantifiably represented by:

$$J_{SC} = -q \int_0^{L, L_D} \int_0^\infty A(\lambda, x) \phi_{exc}(\lambda) d\lambda dx \quad (53)$$

where ϕ_{exc} is the excitation photon current and A is the absorption of the material; $A(\lambda, x)$ takes the form $\alpha(\lambda)e^{-\alpha(\lambda)x}$ where $\alpha(\lambda)$ is the material's absorption coefficient at photon wavelength λ (see equation (10)). The bounds of the first integral signify absorption within L_D or L , whichever is smaller. Essentially, only the photons which are absorbed within the diffusion length contribute to J_{SC} , so as the diffusion length shrinks, J_{SC} shrinks along with it. This is why J_{SC} loss starts out quite small when L_D is slightly less than L : absorption drops exponentially from the front interface, so there are comparatively few photons to lose near the back interface.

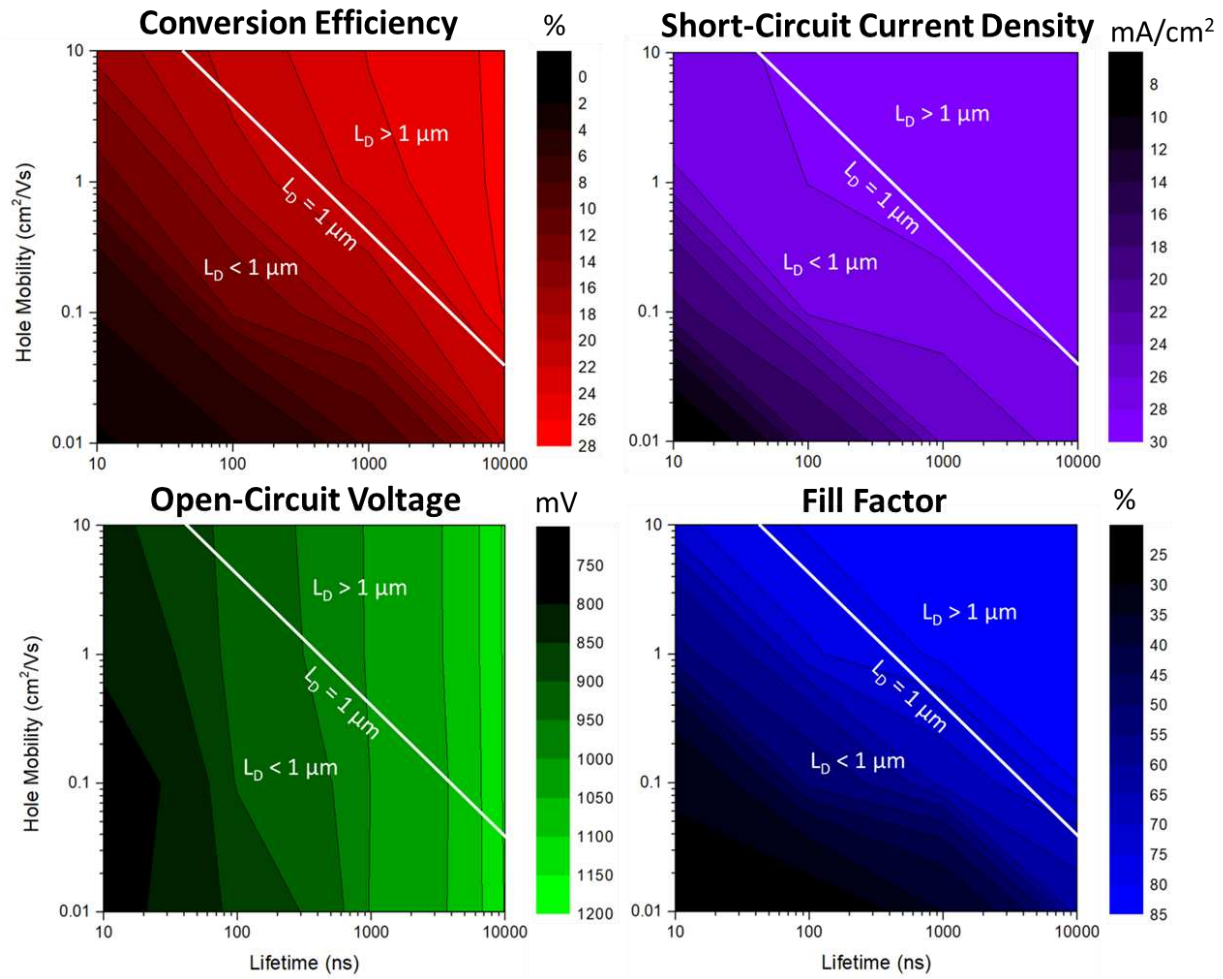


Figure 34. Contour plots indicating simulated efficiency, open-circuit voltage, short-circuit current density, and fill factor as a function of absorber lifetime and hole mobility. $L_D = L$, $L_D > L$, and $L_D < L$ are indicated.

The complete range of simulated lifetimes and mobilities are summarized as contour plots in Figure 34. The frontier representing $L_D = L = 1 \mu\text{m}$ is indicated on each. The main conclusions from the previous three sections are clearly illustrated here. Open-circuit voltage is independent of hole mobility, save for the bottom-left quadrant in which low fill factor distorts the result. Short-circuit current is directly dependent on diffusion length – slope of constant J_{SC} on the contour plot is equal to the slope of constant L_D – and is maximized when $L_D \geq L$. Fill

factor follows a similar trend as J_{SC} . Conversion efficiency is generally higher with greater L_D , with lifetime weighted more favorably due to increased voltage. A lifetime of 1 μ s is sufficient for ~24% conversion efficiency with only 1 cm^2/Vs hole mobility.

The mobilities investigated in this section would typically all be considered quite low, with those less than 1 cm^2/Vs considered very low, even in polycrystalline materials. Normally, this would suggest that hole mobility would not be a point of concern. However, there is some evidence that hole mobilities in the CdSeTe alloy deposited at CSU are in fact very low due to sub-bandgap hole traps from which most of the very high-lifetime luminescence is emitted. Therefore most of the long-lived carriers producing high implied voltages would be essentially stationary and therefore not collected [145]. As will be demonstrated in the next section, reducing absorber thickness allows substantially higher performance with low mobility. In addition, Section 4.5.2 describes a physical cell with high current collection utilizing a CdSeTe-only absorber, demonstrating that the potential problem of low mobility is not insurmountable. The challenge may be to achieve good carrier conduction without penalizing ERE, potentially through absorber deposition process optimization, overpressure anneals, heat treatments, etc.

4.3.4 Thickness

All simulation results presented in this chapter thus far have used an absorber thickness of 1 μ m. As the separation of the contacts directly dictates the strength of the junction field in this structure as well as the distance photoexcited holes must travel, this distance is important. Figure 35 shows the effect of absorber thickness on conversion efficiency at four hole mobility values using a lifetime of 1 μ s. In general, performance peaks near 1 μ m and decreases with deviation in either direction (performance at 0.01 cm^2/Vs is quite low no matter the thickness). The rate of performance reduction as thickness increases is strongly dependent on hole mobility.

This behavior can be explained and characterized by looking at V_{OC} , J_{SC} , and fill factor individually.

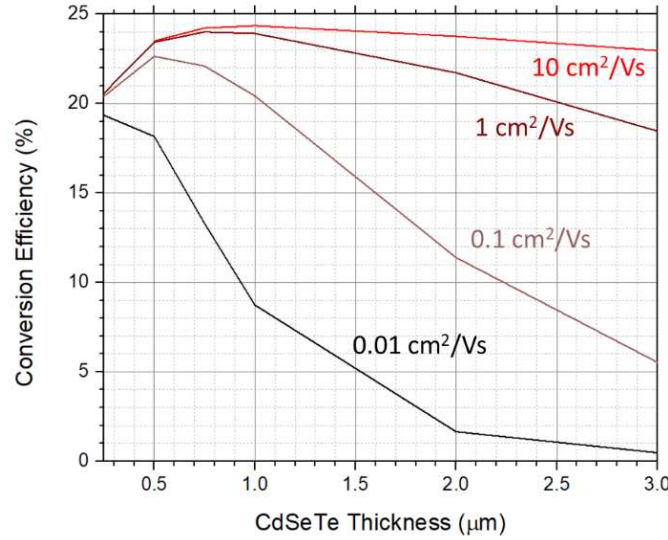


Figure 35. Efficiency as a function of absorber thickness for simulated n-i-p structure at four hole mobilities.

The effect of thickness on voltage is shown in Figure 36. Voltage is highest when the absorber is thinnest and decreases monotonically as thickness increases. Voltage is the same for the highest mobilities and generally the same for all curves with very thin absorbers, indicating independence from mobility when $L_D > L$. Thickness dependence on V_{OC} is well known, and thinner absorbers are variously described as reducing the recombination flux j_0 [160] or reducing the entropy per absorbed photon allowing more work to be done [161], both of which increase V_{OC} . When recombination is low and J_{SC} is independent of thickness ($J_{SC} \gg j_0$ and $L_D \gg L$):

$$\frac{dV_{OC}}{dL} = -\frac{kT}{q} \frac{1}{L} \quad (54)$$

where L is the thickness of the absorber [161]. This change therefore is independent of lifetime and mobility, and is always negative. This relationship agrees with Figure 36 very well for 1

cm²/Vs and 10 cm²/Vs mobility: ~25 mV is lost between 1 μm and 2 μm, ~50 mV is lost between 0.5 μm and 1 μm, etc. The analysis breaks down as $L_D \ll L$, so voltage loss increasingly deviates with 0.1 cm²/Vs and 0.01 cm²/Vs mobility. Suffice to say, very low fill factors are skewing the results due deterioration of diode behavior, and these mobilities are too low.

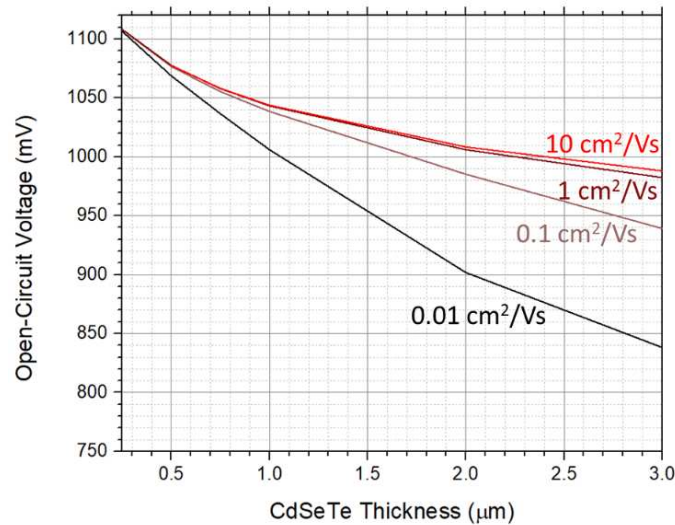


Figure 36. Open-circuit voltage as a function of absorber thickness for simulated n-i-p structure at four hole mobilities.

The effect of thickness on J_{SC} is shown in Figure 37. Behavior can be classified into two categories. When the absorber is very thin, current loss is simply due to incomplete absorption of photons, particularly of low energy. The thinner the absorber, the fewer carriers are generated, reducing current. Note how this effect is entirely independent from diffusion length: current loss in the ultra-thin absorber region in Figure 37 is the same for all L_D . Current loss with thicker absorbers is explained as in Section 4.3.3. When the diffusion length is on the same scale as the absorber thickness (i.e. the $L_D = 1.6 \mu\text{m}$ and $L_D = 5.1 \mu\text{m}$ curves), current is maximized. Note that although 1.6 μm is less than 3 μm, most of the current is still collected – there is a fair amount of leniency at short circuit as the holes are pushed by the strong diode fields. When the

diffusion length is significantly less than the absorber thickness (i.e. the $L_D = 0.51 \mu\text{m}$ and $L_D = 0.16 \mu\text{m}$ curves), substantial current losses appear as holes recombine before they can travel the length of the absorber and be collected at the back contact. Current decreases as the absorber becomes thicker, as there are more opportunities for carriers to recombine.

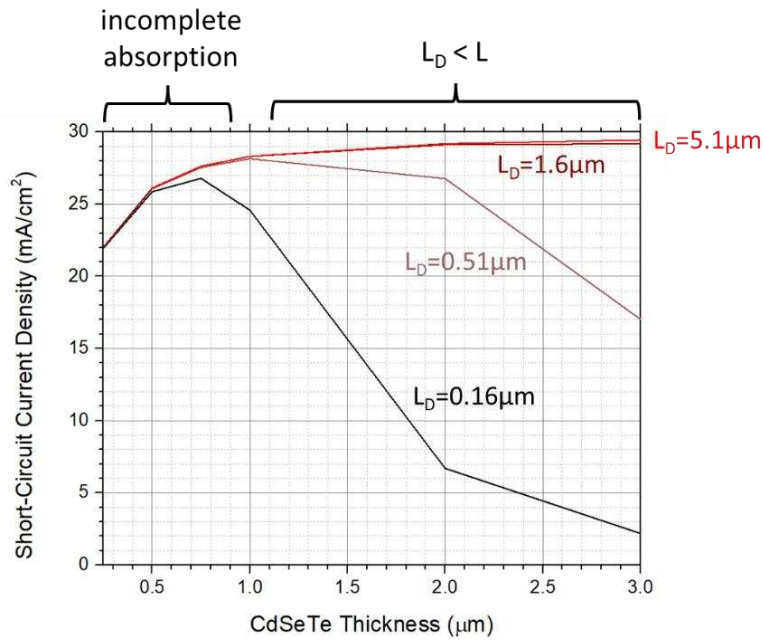


Figure 37. Short-circuit current density as a function of absorber thickness for simulated n-i-p structure at four hole mobilities – diffusion length is indicated. At very low thickness, current loss is due to incomplete absorption. At larger thickness, current loss occurs when diffusion length is substantially less than the thickness.

Fill factor is shown in Figure 38 to decrease with thickness; this decrease is more severe with smaller L_D . Fill factor is harder to quantify than V_{OC} and J_{SC} , but a qualitative explanation should suffice. As the cell is placed farther into forward bias, the fields which drive carrier movement become weaker. Fields which are sufficient to drive carriers across the absorber at J_{SC} may no longer be sufficient in forward bias. Reduced current collection as voltage increases results in reduced fill factor. This effect becomes more pronounced as the absorber thickness

increases because carriers are less likely to be collected when they have farther to travel. Similarly, lower mobility carriers are more reliant on fields to push them to their respective contacts. Fill factor is therefore the most sensitive parameter to mobility. Notice how fill factor is the only parameter differentiating the performance at $10 \text{ cm}^2/\text{Vs}$ and $1 \text{ cm}^2/\text{Vs}$ mobilities: identical QFLS at open circuit and strong fields at short circuit render these parameters essentially independent of mobility, but reduced current collection with weaker fields in forward bias penalizes the lower mobility with thicker absorbers.

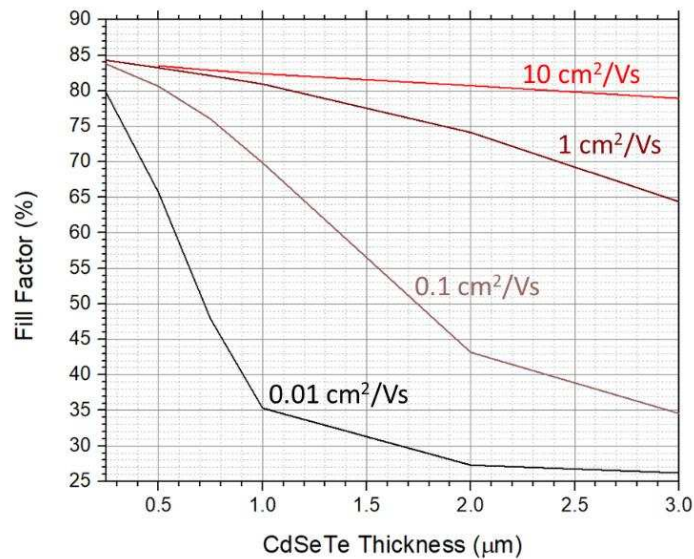


Figure 38. Fill factor as a function of absorber thickness for simulated n-i-p structure at four hole mobilities.

The modeling in this section suggests a strong benefit of thin absorbers in the architecture shown in Figure 29, substantially thinner than in typical cell designs. In physical cells, back interface recombination becomes more important as the cell becomes thinner [162], [163]. The closer the back interface is to the excitation region of the absorber, the more opportunities there are for recombination. Ideally, both interfaces would be well passivated. However, while back

interface recombination is generally not as impactful as at the front, a defective back interface which may be benign and even go unnoticed in a different architecture with a thicker absorber would become more problematic with a thinner absorber. Therefore, in addition to absorber lifetime, the n-i-p structure is also particularly sensitive to interface recombination at *both* interfaces. This may present a challenge to the achievement of high efficiencies with this cell design.

In conclusion, the absorber should be as thin as possible before incomplete absorption noticeably reduces current. Given CdSeTe's excellent absorptivity, this ideal thickness is $\sim 1 \mu\text{m}$. Optical management in the form of a reflective back surface is a way to increase the depth available for current collection while preserving voltage benefits of a thinner absorber, potentially enabling increased performance from even thinner absorbers. An additional benefit of thin absorbers is reduced usage of materials. Even a small reduction in CdTe content per module can lead to massive cost savings as deployment is scaled up. Additionally, as tellurium is a relatively rare material in Earth's crust, the amount of CdTe used per Watt generated is clearly an important parameter in determining CdTe's feasibility for large-scale adoption. A successful n-i-p structure can therefore potentially see improved performance simultaneously with reduced cost and more efficient usage of limited materials.

4.4 p-contact Requirements

As with the absorber, when evaluating the p-contact it is best to do so in a cell configuration in which all other components are optimal. Unless specified otherwise, all modeling in this section uses a $1\text{-}\mu\text{m}$ thick CdSeTe absorber with $1 \mu\text{s}$ lifetime and $1 \text{ cm}^2/\text{Vs}$ mobility. Although a slight performance boost could be gained from higher lifetime and

mobility, this selection allows the p-contact's effects to be easily discerned while representing comfortably realistic, currently-attainable absorber material.

Many parameters for the p-contact material were investigated. A few key parameters each capable of significantly affecting cell performance on their own were identified, and these parameters will be discussed in this section. In addition, several other parameters were found to have negligible effects. In ideal conditions, the lifetime in the p-contact material has no effect at all. This is because other components of the cell design prevent electrons from reaching this layer, so there are no opportunities for recombination, no matter the defect density. Likewise, as there are no electrons, electron mobility is irrelevant. Hole mobility was found to have minimal effect until it was reduced to unreasonably low values, $\leq 10^{-4}$ cm²/Vs. Contact thickness also had little effect, even beyond unreasonably high values of several microns. As only front-side illumination is considered, the absorption coefficient is also irrelevant.

Some of these parameters *did* begin to exert some influence on performance as the cell structure deviated significantly from ideal. For example, in a highly contrived situation where a substantial number of electrons enter the p-contact, adjusting lifetime in this material *does* have a small effect. However, in this situation the performance is already substantially reduced due to loss of selectivity, so it is not a useful parameter space to explore, and the small effect of lifetime is totally irrelevant. These unimportant parameters only exhibit their comparatively small influence when the key parameters are poor; as such they are “dependent” on the true important “independent” parameters, which are always relevant. No plots for these inconsequential parameters are shown, and they will not be discussed further. Values for fixed p-contact parameters are shown in Table 3.

Table 3. Fixed parameter values for the modeled p-contact.

Fixed p-contact modeling parameters		
Quantity	Symbol	Value
thickness	L	0.2 μm
relative permittivity	κ	9
carrier thermal velocity	v_{th}	10^7 cm s^{-1}
electron mobility	μ_e	$100 \text{ cm}^2\text{V}^{-1}\text{s}^{-1}$
hole mobility	μ_h	$1 \text{ cm}^2\text{V}^{-1}\text{s}^{-1}$
donor density	N_D	0 cm^{-3}
bulk lifetime	τ_{bulk}	10 ns
surface recombination velocity	$S_{\text{front}} ; S_{\text{back}}$	10^0 cm s^{-1}

The most important parameters were determined to be the p-type carrier concentration and the relative band positions between the absorber and the p-contact, quantified as the **valence band offset (VBO)** and **conduction band offset (CBO)**. A negative offset is defined as a p-contact band edge at a *lower* energy than the absorber’s corresponding band edge, while a positive offset has a p-contact band position at *higher* energy than the absorber’s, shown in Figure 39. The same convention is applied to both the valence and conduction bands.

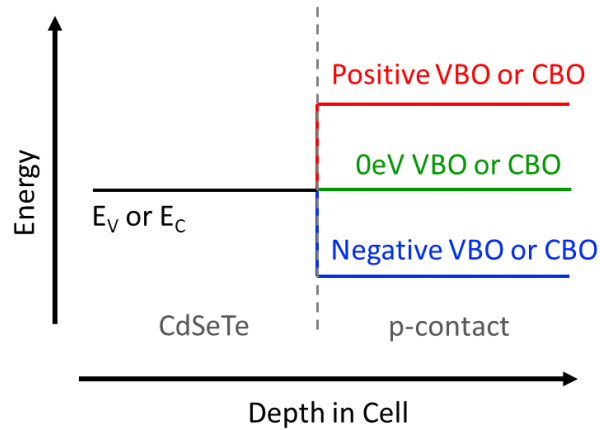


Figure 39. Schematic illustrating the “positive” and “negative” band offset naming convention. The offset in question always refers to the interface between the CdSeTe absorber and the p-contact material behind it. The same convention is applied to both the valence and conduction bands.

4.4.1 CdSeTe/p-contact Valence Band Offset

As the p-contact is meant to be hole-selective, the valence band shape must allow unimpeded flow of holes. Figure 40 shows the effect on conversion efficiency of valence band offset at three p-contact doping levels. An “ideal” CBO of 0.6 eV is used for all simulations. As expected, the optimal situation is a VBO of 0 eV, allowing maximally unimpeded hole travel through the interface. Deviating in either direction results in loss of performance, but the mechanisms at play are completely different with positive and negative VBO, evidenced by the different behaviors on either side of 0 eV in Figure 40. Note the lower efficiency at 10^{14} cm^{-3} hole concentration, representing insufficient doping.

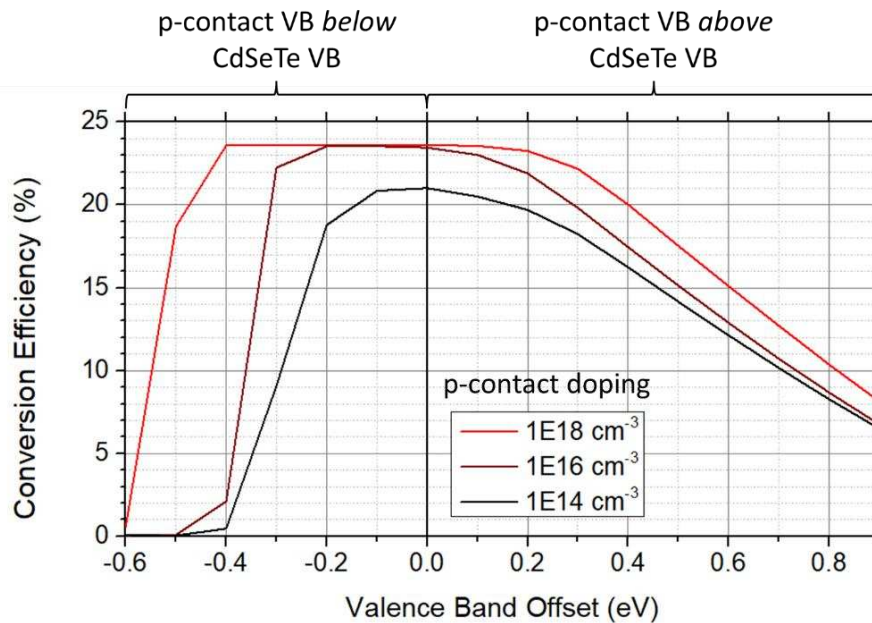


Figure 40. Conversion efficiency of simulated cell as a function of valence band offset between the CdSeTe absorber and p-contact, for three p-contact doping levels. Performance is highest at 0 eV VBO, and drops off in either direction. Reductions in performance on either side of 0 eV manifest differently, as they are caused by different mechanisms. High p-contact doping mitigates the performance reduction and allows for the best performance.

With a negative valence band offset, the valence band of the p-contact is below that of the absorber. This creates a hole barrier, impeding the flow of holes at the back of the cell. At a critical barrier height, the movement of holes out of the back contact is impossible and no current is collected, leading to a complete loss of cell functionality. Figure 40 indicates that this transition is quite abrupt. With low carrier concentration, this hole barrier is wide, shown in black in Figure 41. This structure is very effective at blocking holes, preventing current collection at small barrier heights. With higher p-contact carrier concentration, the bands within the p-contact bend upward towards the p-contact Fermi level, narrowing the barrier width, as shown in red in Figure 41. With a sufficiently narrow barrier, holes are able to tunnel through it and escape through the back contact, preserving the cell's current density. Higher p-contact doping can ensure a thin-enough barrier at higher VBOs, allowing more leniency in VBO deviation before current is impeded, shown in Figure 40. As precisely tailoring the valence band of materials is not likely to be possible, this result indicates that low to moderate negative valence band offsets can be tolerated if high doping of the p-contact can be attained. However, at sufficiently negative VBO, current collection becomes impossible no matter the doping of the p-contact.

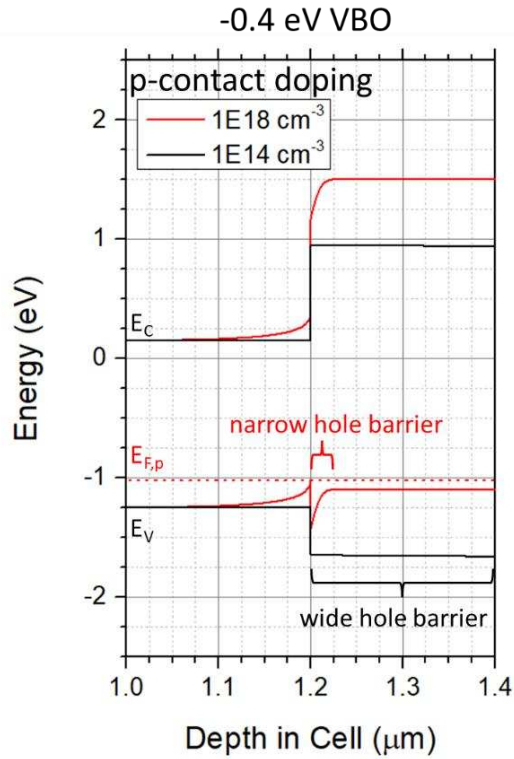


Figure 41. Comparison of a -0.4-eV valence band offset between the CdSeTe absorber and the p-contact at low (10^{14} cm^{-3}) and high (10^{18} cm^{-3}) p-contact doping, shown at V_{OC} . At low doping, a wide hole barrier in the valence band completely blocks the flow of holes, preventing current collection. At high doping, band bending in the p-contact results in a much narrower hole barrier “spike.” This barrier is narrow enough to allow holes to tunnel through, preserving current despite the large negative VBO.

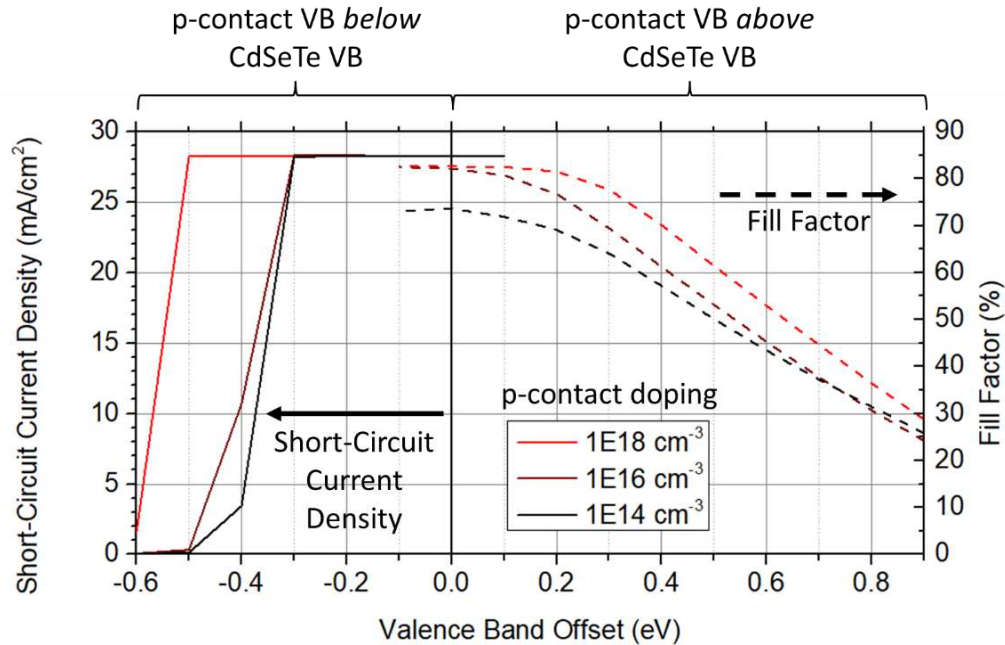


Figure 42. Short-circuit current density and fill factor as a function of valence band offset between the CdSeTe absorber and p-contact, for three p-contact doping levels, shown only under their relevant respective ranges. Open-circuit voltage is unchanged over entire range, so it is not shown. A negative VBO impacts short-circuit current density, while a positive VBO affects fill factor.

With a positive valence band offset, the valence band of the p-contact is above that of the absorber. While this band structure would not seem problematic when viewed at dark equilibrium in isolation, there are less-obvious detrimental effects of a positive VBO. The conduction and valence band positions of the n- and p-contacts are determined by their bandgaps, work functions, and Fermi levels following Anderson's rule [164], [165]. At a given p-contact doping, maintaining a positive VBO between the absorber and p-contact reduces the upward band bending in the absorber, mildly weakening the internal fields at 0 V (dark). There is a much more serious problem, however. As the cell moves into forward bias, the bands at the back of the absorber are forced to bend downwards to maintain VBO (Figure 43), similar to a Schottky barrier. This downward band bending creates a hole barrier which increases in height as

the cell is placed farther into forward bias. This increasingly large impediment to current in forward bias results in a reduced fill factor. This fill factor penalty is made worse as the VBO becomes more positive, and according to Figure 42, the effect is rather linear. Unlike with a negative VBO, reduction in performance is rather gradual. As higher p-contact doping moves the p-contact's bands upwards slightly, increasing the valence band energy of the absorber at the back, detrimental downward band bending begins to occur at a *slightly* higher voltage, improving fill factor. However, there is very little additional band energy to be gained from even unrealistically large gains in doping, so this mitigating effect is very small. Note the relatively small differences in performance between the p-contact doping levels in Figure 40 at positive VBO. The amount of positive VBO has a much stronger influence than the amount of doping.

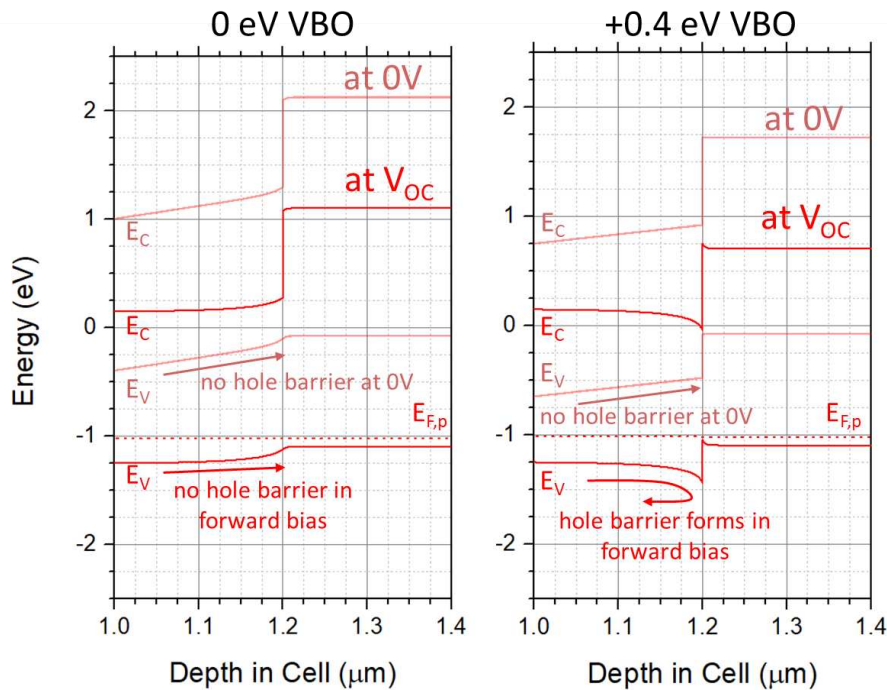


Figure 43. Comparison between 0-eV VBO and +0.4-eV VBO of bands at the back interface at short circuit and open circuit. With a 0-eV VBO, holes can freely traverse the interface at short circuit and open circuit and every bias in between, yielding high fill factor. With a +0.4-eV VBO, while holes can freely traverse the interface at short circuit, a hole barrier forms in forward bias, reducing fill factor.

4.4.2 CdSeTe/p-contact Conduction Band Offset

The energy of the p-contact conduction band is also important, though modeling shows that it is not as decisive as the valence band energy. As with the valence band, a negative conduction band offset (CBO) is defined with the p-contact conduction band lower than the CdSeTe's conduction band, and a positive CBO is when it is higher, shown in Figure 39. The effects of CBO on performance for the same simulated structure are shown in Figure 44. An ideal VBO of 0 eV is used in all simulations. Below a 0-eV CBO, performance is mostly the same; this region simply represents the lack of an electron reflector, and all electrons are free to traverse the interface. With a positive CBO, some performance gains are realized as some electrons are now blocked at the interface. As the CBO becomes more positive, the height of the electron barrier increases, increasing performance until a barrier height of about 0.4 to 0.5 eV, at which point increases in the barrier height no longer yield higher performance. It can therefore be concluded that this barrier height is sufficient to block all electrons. Improvements in performance are caused entirely by improvements in open-circuit voltage, shown in Figure 45, as the electron barrier improves hole selectivity at the back contact.

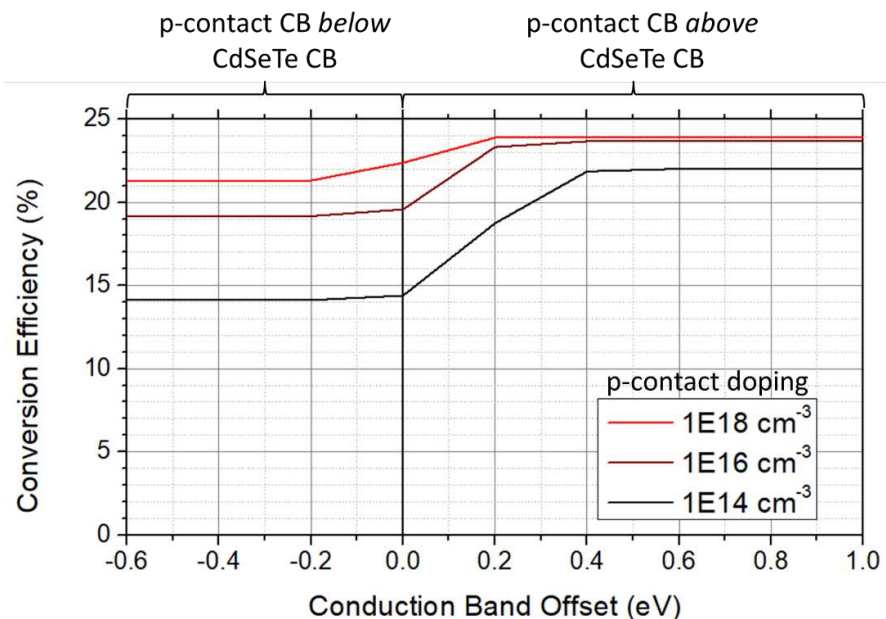


Figure 44. Conversion efficiency of simulated cell as a function of conduction band offset between the CdSeTe absorber and p-contact, for three p-contact doping levels. In this example, electron mobility within the absorber is high ($100 \text{ cm}^2/\text{Vs}$) to accentuate the differences. Performance is highest when $\text{CBO} > \sim 0.4 \text{ eV}$, and lowest when $\text{CBO} \leq 0 \text{ eV}$. High p-contact doping mitigates the performance reduction and allows for the best performance.

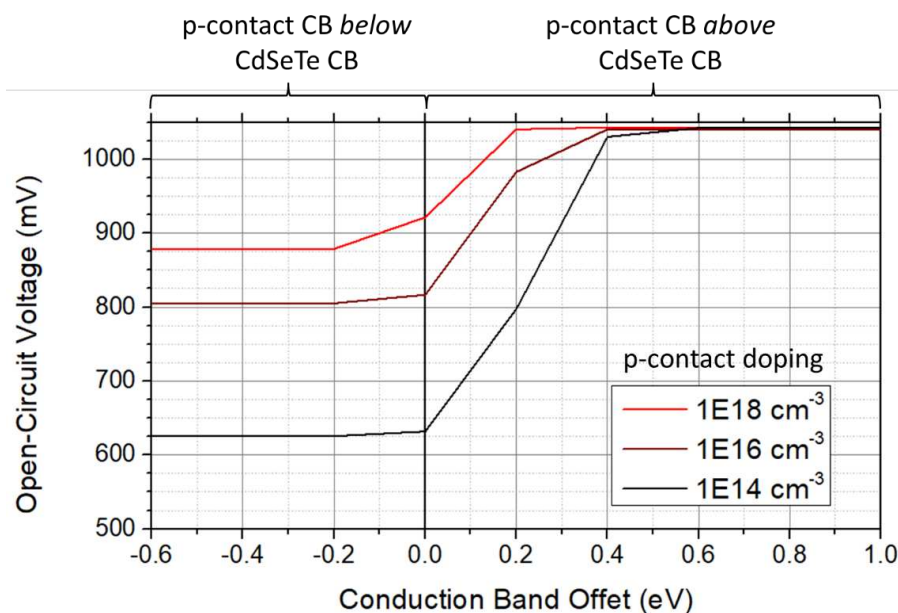


Figure 45. Open-circuit voltage as a function of conduction band offset between the CdSeTe absorber and p-contact, for three p-contact doping levels. Current density is unchanged over entire range, so it is not shown. Fill factor is affected only by the changing voltage, so it also is not shown. Electron barrier height affects carrier selectivity, which directly affects voltage.

Figure 44 indicates that lower doping of the p-contact results in a larger performance loss when the electron barrier is removed at $\text{CBO} < 0 \text{ eV}$. At higher (10^{18} cm^{-3}) doping, the p-contact Fermi level's proximity to the valence band edge causes the bands in the CdSeTe to bend upwards slightly at the back of the absorber, acting as a mild electron reflector even when there is no conduction band energy barrier. This allows for better selectivity and higher voltage. This effect does not occur when the p-contact doping is lower, reducing voltage. This band bending is clearly visible in Figure 46, which compares the back interface for 10^{14} cm^{-3} and 10^{18} cm^{-3} doping of the p-contact.

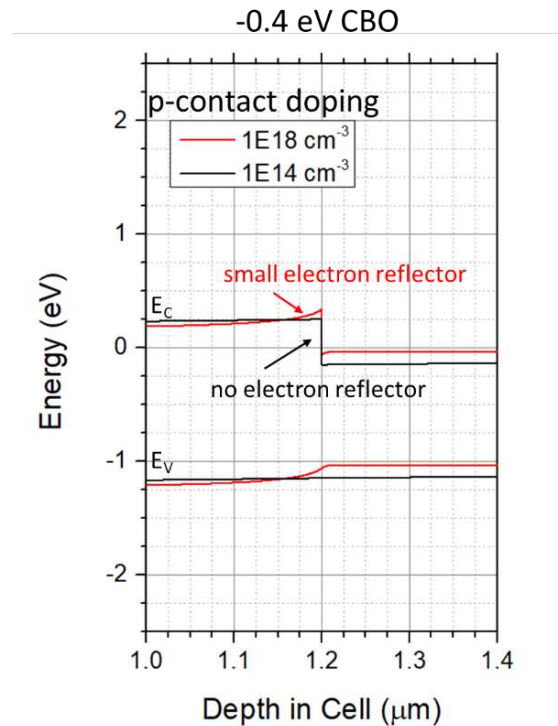


Figure 46. Comparison of a -0.4-eV conduction band offset between the CdSeTe absorber and the p-contact at low (10^{14} cm^{-3}) and high (10^{18} cm^{-3}) p-contact doping, shown at V_{oc} . High doping creates some band bending at the back of the absorber which acts as a small electron barrier, improving voltage. This feature is absent when doping is low.

To accentuate the effects of CBO, the trends displayed in Figure 44 and Figure 45 utilize 1- μm -thick CdSeTe absorbers with a higher electron mobility of $100 \text{ cm}^2/\text{Vs}$. With these parameters, electrons are more likely to reach the back interface, so the electron barrier is more important. With a thicker absorber and/or a lower electron mobility, the performance with a sufficiently high electron barrier is the same but there is less voltage reduction as the barrier height is reduced, as fewer electrons are reaching the barrier. Determining electron and hole mobilities individually – particularly the mobility of the faster particle – is not trivial. As electron and hole mobilities in principle may be very different, it is best to design the cell assuming a high electron mobility; a sufficiently large electron barrier at the back therefore should be sought.

In conclusion, the band structure of the p-contact material is crucial. The valence band position in particular may be the single most important parameter, with very little leniency before a significant reduction in performance. There is far more tolerance in the conduction band position, with only a loose lower bound to ensure maximal performance. All performance parameters can be affected by improper band position, depending on the deficiency. A negative VBO penalizes current, a positive VBO penalizes fill factor (and ultimately current when VBO is very large), and an insufficiently large positive CBO penalizes voltage. All three effects are demonstrated clearly in Figure 42 and Figure 45. Some amount of p-type doping is necessary to form the n-i-p junction and preferentially conduct holes through the back, and higher doping beyond this is useful for minimizing deleterious effects from all potential improper band alignments. This is useful as p-type doping level is likely engineerable to a certain degree in a candidate material, while band positions are likely not.

4.4.3 Interface Recombination

Note that all modeling presented in this chapter assumes perfect interfaces with no additional interface recombination. This is a reasonable simplification to make when trying to determine what is necessary to achieve optimal performance. In physical cells some amount of interface recombination will be present which inhibits performance. However, this is less of an issue than it seems. As mentioned previously, the CdSeTe/p-contact interface is the only potentially problematic one, as the MgZnO/CdSeTe interface is well passivated. Recombination at the back interface is inherently less problematic than the front in non-bifacial cells as the population of electrons at the back is much lower than the population of holes at the front, although this becomes less true with thinner absorbers. Most importantly however, interface recombination is readily revealed by ERE and TRPL measurements. If a sample is measured with >1 V iV_{OC} , that *includes* the effects of interface recombination. While the modeling has implemented lifetime as due to only bulk defects, an equivalent measured lifetime on a physical cell would be expected to have similar performance potential, no matter what combination of bulk and interface defects contributed to that measured lifetime. The challenge remains to design a cell structure which provides excellent selectivity without penalizing luminescence. Thankfully, the degree to which both of these conditions are satisfied is easily determined by existing measurement techniques.

4.5 n-i-p Experiments

A relatively small number of cells in an n-i-p configuration were fabricated with CdSeTe absorbers and a small selection of p-contact materials. While no fabricated cells yielded stellar performance, results were encouraging, as some important conditions were met and useful information was learned indicating strategies for improvement.

An ideal configuration essentially replicates the front contact at the back of the cell, using a hole-selective p-type transparent layer. In contrast to n-type materials, p-type transparent conductive oxides (TCOs) are relatively rare [166], [167], so the candidate material pool is small. As hole selectivity is the most important aspect, materials which did not fulfill the transparency requirement were also considered. Functionality is more important than bifaciality.

4.5.1 NiO

Nickel oxide (NiO) is one of the earliest known p-type TCOs. Intrinsic NiO is quite resistive, but it can be readily doped with copper which substantially improves conductivity and can allow for hole concentrations upwards of 10^{20} cm^{-3} [168]. This is more than sufficient for use as a p-contact. NiO has occasionally been incorporated into CdTe devices; while it has not been shown to meaningfully improve performance, it has not proven detrimental [169]. This result says little about its efficacy as a p-contact in an n-i-p structure utilizing a CdSeTe absorber, but it does indicate that it forms a relatively defect-free interface with CdTe-based materials, which is at least *one* important prerequisite.

To investigate this material, NiO films were deposited using RF sputtering from a 4-in diameter ceramic target at 60 W power in a 15-mTorr Ar ambient. The resulting nearly-transparent films were very resistive, as expected, with resistivities too high to measure using a multimeter. Following the procedure outlined by others [168], [170], small chips of 99.9% pure Cu were placed in the racetrack of the sputter target during deposition in an attempt to dope the films. This procedure produced far more opaque films with a dark bronze color, but resistivity was still too high to measure. Hall measurements were not performed on these films, but the very low conductivities indicate insufficiently low p-type doping. These results could indicate very low activation of copper as a dopant. As copper is generally preferentially sputtered over nickel

[171], it could also indicate a proclivity for the formation of copper oxides, which can be very resistive depending on the oxygen content [172]. In either situation, it is unknown why this doping method did not yield the same results reported in the literature.

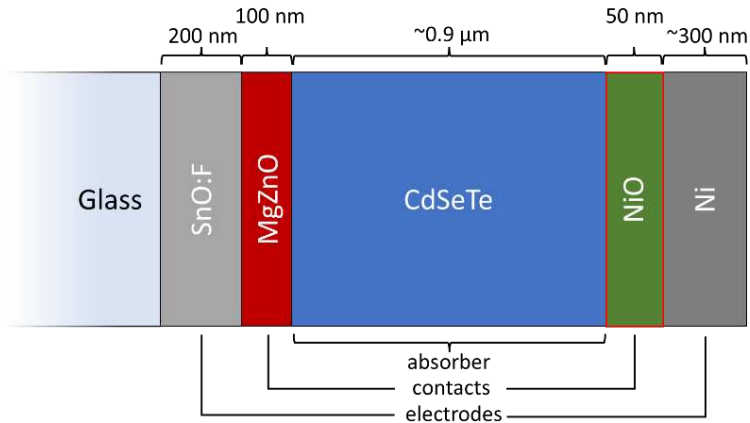


Figure 47. Structure of fabricated n-i-p cells with NiO p-contact.

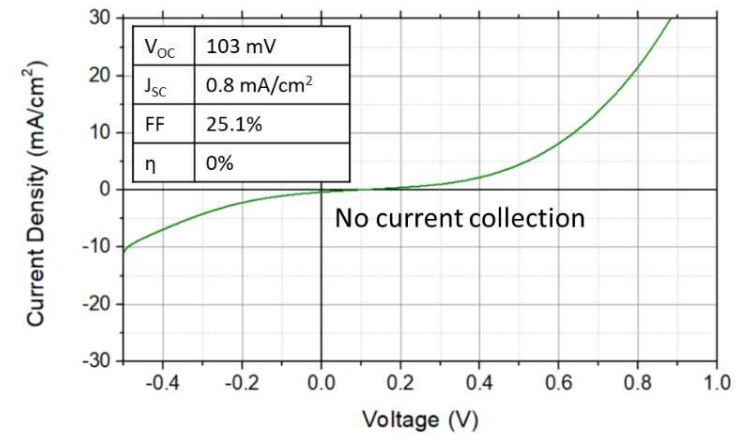


Figure 48. J-V measurement of n-i-p cell with NiO p-contact. Behavior indicates a substantial hole barrier at the back of the cell.

Though the material appeared unsuitable for the desired purposes, complete cells utilizing NiO were nevertheless fabricated. These cells had the simple structure TEC10 / MgZnO (100nm)

/ CdSeTe (1 μm) / NiO (50 nm) / Ni (~300 nm), illustrated in Figure 47. CdSeTe was deposited by close-space sublimation, MgZnO and NiO was deposited by RF sputtering, and the Ni electrode was deposited by DC sputtering. The CdSeTe underwent a CdCl₂ passivation treatment, but no intentional doping treatment. Cells with intrinsic NiO and NiO sputtered with various amounts of Cu chips were fabricated, but all cells produced J-V curves similar to Figure 48. The complete lack of current collection and strongly kinked J-V behavior are both indications of a substantial barrier – this almost certainly represents a barrier to holes at the back of the cell. While the lack of sufficient p-type doping and very low conductivity are probably enough to explain this result, NiO as a material has another serious issue which likely renders it unsuitable for this application. While NiO's wide bandgap of >3.6 eV [168] forms an excellent electron reflector, between CdTe and NiO is a valence band offset of approximately +0.5 eV [169] (this would be the same with CdSeTe). As the modeling in Section 4.4 has demonstrated, even with otherwise ideal material, NiO's large positive VBO with CdSeTe would be expected to have severe detrimental effects on fill factor, making it an unsuitable material choice.

4.5.2 ZnTe

As the modeling suggests that valence band alignment with CdSeTe is the single most important requirement of the p-contact material, the material search was focused on this specific characteristic. ZnTe is a II-VI semiconductor with a VBO with CdTe of 0.0 [173], [174] to 0.1 eV [175], and its wider bandgap of ~1.7-2.3 eV [176] results in a sufficiently large CBO to create an effective electron barrier. It can be made highly p-type with a variety of dopants. Although its opacity makes it unsuitable for bifacial cells, its ideal band structure and p-type dopability make it a very promising material to use as a p-contact in this configuration.

ZnTe's potential suitability as a back contact for CdTe has been known for decades. The ~0-eV valence band offset with CdTe is often quoted as facilitating good hole transport. However, few sources provide a compelling explanation for its use, with reduction of interface recombination or prevention of Schottky barriers often cited with little elaboration. Most applications simply add a layer of ZnTe to the back of "traditional" device structures [162], [176]–[179], which has little positive effect, if any. Some have actually used ZnTe:Cu to *introduce* Cu into the CdTe absorber [180], [181], which again yields no obvious benefit. Only a small number of sources use intentionally undoped CdTe [182], [183].

Reporting by *Meyers* [183]–[186] of an Ametek, Inc. design from the late 1980's are the only sources known to the author which explicitly describe a CdTe n-i-p heterojunction photovoltaic structure, with ZnTe and CdS as the contact layers (some follow-up is reported in [187] and [188]). The rationales given in these sources are still very relevant: CdTe's tendency to self-compensate as well as the difficulty in achieving low-resistance contacts with p-type CdTe are listed as motivation for leaving it intrinsic, to "accommodate its innate properties." The band alignments of CdS and ZnTe with CdTe are described as being beneficial for selective carrier conduction, with the intention of utilizing *rectifying* contacts explicitly stated. This near-forgotten work from over three decades ago provides the most compelling justification for the application of ZnTe available. Unfortunately, realization of this idea was likely restricted by the material limitations of the time. CdS has been largely supplanted due to its parasitic absorption and poor interface quality [130], and CdTe does not support the lifetimes necessary to extract high performance from this architecture. However, with modern material advancements in the form of MgZnO and CdSeTe, along with more advanced characterization and modeling proving the viability of the concept, it is worth pursuing again.

To evaluate this material, ~1- μm films were sputtered from a 4-in diameter ZnTe target onto TCO-free TEC SB glass for Hall measurements. Sputter power was 60 W in an 18 mTorr Ar ambient. The resulting films were fairly opaque with a dark brown color. Square samples of approximately 1 cm^2 were cut, and a small dab of indium solder was deposited at each corner to function as contacts. Four-point Hall measurements were carried out with an Ecopia HMS-3000; measurements were performed in both magnetic field orientations to verify carrier type, as well as across both diagonals of the sample and averaged in order to eliminate errors from imperfect square sample geometry. Unsurprisingly, the films exhibited negligibly low p-type doping, with hole concentrations $\sim 5 \times 10^{11}\text{ cm}^{-3}$ and resistivities $\sim 5 \times 10^5\ \Omega\text{cm}$.

While as-deposited ZnTe is essentially intrinsic, as with CdTe it can be made p-type by doping with Cu [177], [179]–[182], [189], [190]. ~1- μm films of ZnTe:Cu were sputtered from a 4-in diameter $\text{Zn}_{0.47}\text{Te}_{0.47}\text{Cu}_{0.06}$ target. Sputter power was 60 W in an 18-mTorr Ar ambient. Depositions at room temperature produced films with unmeasurably high resistivity. To remedy this, following previously reported work [177], depositions were carried out at a substrate temperature of $250\text{ }^\circ\text{C}$ and the films were subsequently annealed for 20 minutes at $250\text{ }^\circ\text{C}$ in an 18-mTorr Ar ambient. 1-cm^2 square samples were prepared and Hall measurements were performed as before. Typical hole concentrations of $\sim 1 \times 10^{16}\text{ cm}^{-3}$ were attained, with resistivities as low as $\sim 1.2\ \Omega\text{cm}$. Films sputtered with additional 99.9% pure Cu chips in the target's racetrack yielded slightly higher hole concentrations of $\sim 2 \times 10^{16}\text{ cm}^{-3}$.

As ZnTe:Cu was determined to have sufficiently high p-type doping, cells of the simple structure TEC10 / MgZnO (100nm) / CdSeTe (1 μm) / ZnTe:Cu (50 nm) / Ni ($\sim 300\text{ nm}$), illustrated in Figure 49, were fabricated using the deposition methods discussed in Section 4.5.1.

As with the samples for Hall measurements, ZnTe:Cu was sputtered at a substrate temperature of 250 °C and subsequently annealed for 20 minutes under the deposition conditions.

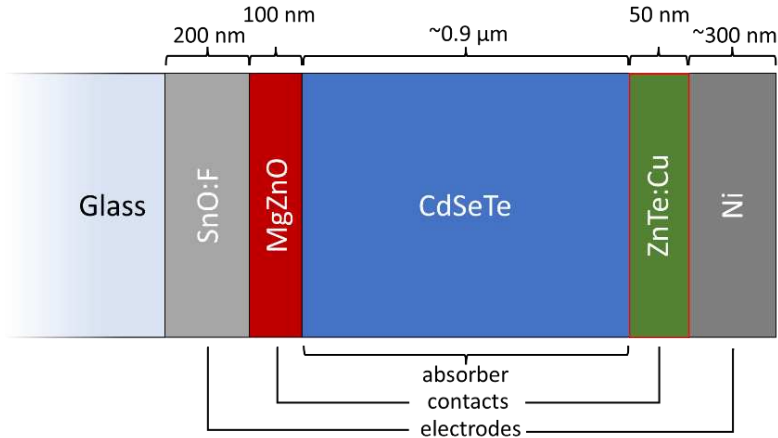


Figure 49. Structure of fabricated n-i-p cells with ZnTe:Cu p-contact.

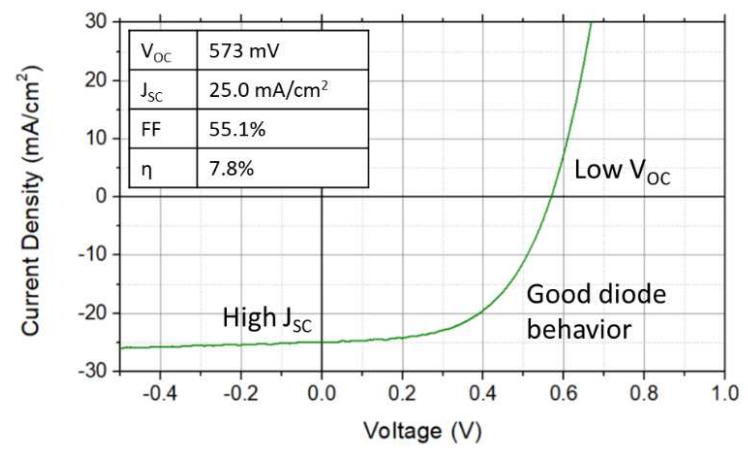


Figure 50. J-V measurement of n-i-p cell with ZnTe:Cu p-contact. Good current collection and diode shape indicate the absence of a hole barrier. Voltage is quite low, however.

The J-V curve for the best-performing cell is shown in Figure 50, although it should be noted that most cells had very similar performance parameters, and this example is not an outlier. While the open-circuit voltage is unusually low, this result is very encouraging, especially as this

is the first known functioning cell with a nominally-undoped CdSeTe-only absorber. Current density of 25 mA/cm^2 is not far below the $\sim 28 \text{ mA/cm}^2$ typical of the best-performing CdSeTe/CdTe cells without antireflective coatings fabricated at CSU [119]. This current is even more impressive when considering that the thickness of the CdSeTe absorber was only $\sim 900 \text{ nm}$, potentially introducing losses due to incomplete absorption. While the fill factor is only mediocre, the diode characteristics are well-behaved; there is no evidence of kinking and only very small amounts of voltage-dependent current collection are present. The low fill factor is therefore largely a function of the low voltage. The good current collection and diode behavior are both suggestive of favorable band alignment at the back of the cell, allowing unimpeded hole collection.

There are several possible explanations for the low voltage of this cell, but low lifetime in the absorber seems the most significant. Figure 51 shows steady-state photoluminescence measurements of the cell before and after ZnTe:Cu deposition measured from the glass side and the film side. Luminescence of the passivated absorber is quite high, and the shoulder above 950 nm indicates the presence of a large sub-bandgap peak which the silicon photodetector was unable to see. However, after the deposition of ZnTe:Cu and subsequent anneal, a nearly 10x reduction in luminescence intensity is observed. The reduction is also significant from the film side, indicating that the problem is arising from the ZnTe:Cu layer. This luminescence reduction could be due to Cu diffusion from the ZnTe:Cu into the CdSeTe absorber, where the resulting Cu-related defects [191]–[193] significantly diminish the absorber's lifetime and external radiative efficiency. Cu is known to be highly mobile in CdTe-based materials [194], and has been shown to diffuse from ZnTe:Cu into CdTe specifically [180], [181]. As the significant

reduction in ERE would be expected to reduce voltage while preserving current and fill factor, this is a likely explanation.

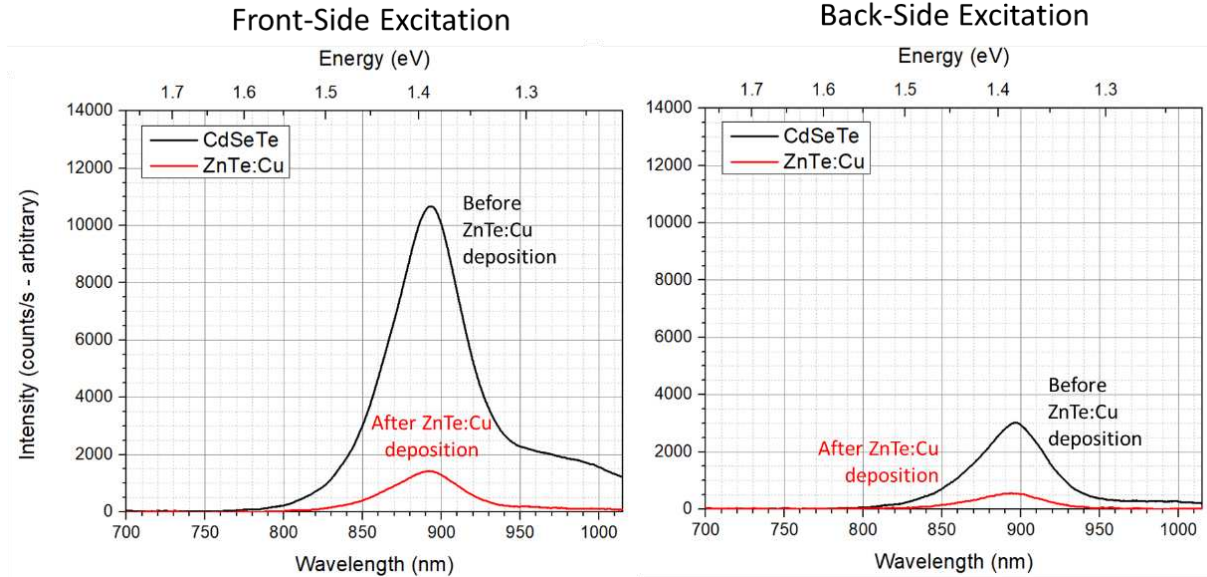


Figure 51. Measured steady-state photoluminescence before and after ZnTe:Cu deposition from the glass side and film side. The 10x reduction from the glass side after ZnTe:Cu represents dramatically increased recombination in the bulk, indicating copper diffusion from ZnTe:Cu into CdSeTe.

Depositing a material layer between the absorber and the ZnTe:Cu p-contact may prevent copper from diffusing. The choice of this barrier material is rather limited, however; for it to not impair the performance of the cell, it has the same band structure requirements as the p-contact outlined above. A non-ideal band structure may be acceptable if the layer were thin enough to allow tunneling (on the order of a few nm), but such a thin layer is likely to be less effective at blocking Cu. For these reasons, undoped ZnTe is a natural choice. To investigate this hypothesis, cells were fabricated with the structure TEC10 / MgZnO (100nm) / CdSeTe (1 μm) / ZnTe (50 nm) / ZnTe:Cu (50 nm) / Ni (~300 nm). Both ZnTe and ZnTe:Cu layers were deposited at 250 $^{\circ}\text{C}$ with 20-minute anneals after each. The J-V performance of these cells is not interesting as

there was a large amount of shunt conductance, likely from pinholes in the CdSeTe absorber. However, steady-state photoluminescence measurements are revealing, shown in Figure 52. Even with the ZnTe “barrier” layer, there is a $\sim 10\times$ reduction in luminescence after deposition of ZnTe:Cu compared to the passivated absorber. This is identical to the result without the ZnTe layer (Figure 51), indicating that ZnTe is completely ineffective as a barrier, and Cu appears to easily diffuse through it. While it may be possible to find a material which prevents copper diffusion while not impeding hole transport, it is probably better to pursue an entirely Cu-free structure. Fortunately, ZnTe is readily doped highly p-type by group V elements such as As [178], Sb [195], and especially N [162], [174], [176].

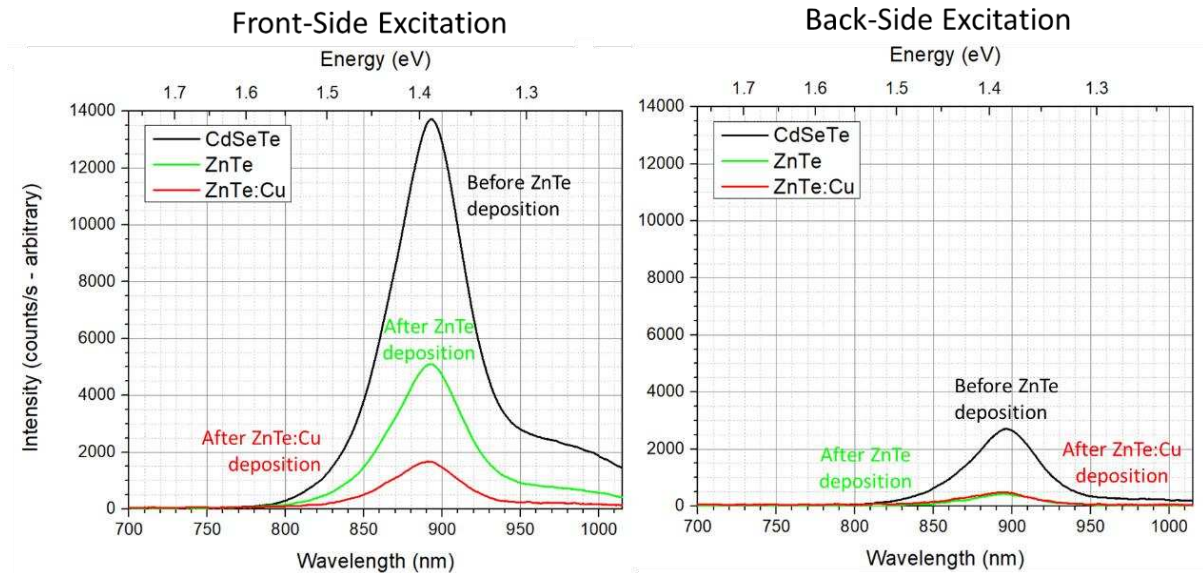


Figure 52. Measured steady-state photoluminescence before ZnTe deposition, after ZnTe deposition, and after ZnTe:Cu deposition from the glass side and film side. The $10\times$ reduction from the glass side after ZnTe:Cu indicates that the ZnTe is not an effective barrier to copper diffusion. The identical luminescence from the film side after ZnTe and ZnTe:Cu compared with the $\sim 2.5\times$ difference from the front is further evidence that Cu diffusion is occurring.

Figure 52 reveals another interesting result: deposition of the undoped ZnTe layer results in a ~3x reduction in photoluminescence intensity from the glass side, indicating a fairly defective CdSeTe/ZnTe interface. CdTe has a lattice constant ~6.4-6.5 Å [196], while CdSe has a lattice constant of ~6.05 Å [196]. As density functional theory has shown [197] that CdSeTe alloys follow Vegard's law [198], the employed CdSe_{0.4}Te_{0.6} absorber alloy has lattice constant ~6.3 Å. ZnTe has a lattice constant of 6.05 Å [173], which is ~4% smaller than that of CdSeTe; this lattice mismatch is likely to create a relatively defective interface. While recombination at the back interface is generally less important than the front and may still allow for high-performing structures in this configuration, this interface will ultimately prevent this architecture from reaching its full potential. While passivation treatments may ameliorate these detrimental effects to some degree, the CdSeTe/ZnTe heterointerface may always prove problematic.

It is worth noting that this result also bolsters the Cu diffusion hypothesis. The difference between the green curve in Figure 52 and the red curves in Figure 51 and Figure 52 indicate that some amount of luminescence loss is attributable to the relatively poor CdSeTe/ZnTe interface and associated dislocation defects, charge accumulation, and band banding, but the additional luminescence reduction when Cu is present is most plausibly explained by the additional effect of Cu-originating defect formation. Furthermore, as this difference is only visible with front-side excitation, the presence of Cu seems to have little influence on the interface itself, and it is a bulk effect.

The ternary alloy Cd_{1-x}Zn_xTe may be useful for addressing the interface recombination issue. It can be made highly p-type without Cu – up to 10¹⁹ cm⁻³ [199], which is more than sufficient for a p-contact (although the nitrogen doping efficiency decreases as x decreases [162]). Although there are no known reported direct measurements, there are indications that the

valence band offset with CdTe is very small [200] (like ZnTe), and changes in bandgap exclusively affect the conduction band. Importantly, this alloy has been shown experimentally to closely follow Vegard's law, exhibiting a linear transition in lattice constant as $0 \leq x \leq 1$ [201]; change in bandgap is also quite linear [201], [202]. Matching the lattice constant of CdSe_{0.4}Te_{0.6} requires Cd_{0.6}Zn_{0.4}Te, which has a bandgap of ~1.7 eV; this represents a respectable ~0.3-eV CBO with CdSeTe, though a slightly larger CBO would be ideal. This bandgap can be increased by making the alloy more Zn-rich, but doing so potentially makes the CdSeTe/CdZnTe interface more defective by introducing lattice mismatch. Therefore, by varying the relative concentrations of Cd and Zn, the tradeoff between interface recombination velocity and electron barrier height can be explored and optimized.

One final point: all modeling in this chapter has assumed single-material contact layers. In the vast majority of cells fabricated at CSU, a thin (~40-nm) layer of tellurium is typically deposited after the absorber to mitigate the Schottky barrier which forms at the CdTe/metal interface [117]. While Te is helpful for this purpose, it is unsuitable as a p-contact due to its poor band alignment with CdSeTe: its ~0.4-eV VBO with CdTe [117] is too large, and its small 0.33-eV bandgap [203] does nothing to block electrons. However, Hall measurements performed at CSU have revealed $>10^{18} \text{ cm}^{-3}$ p-type carrier concentration. While a single highly-p-type material with good band alignment is preferable, if doping ZnTe or CdZnTe to sufficient levels without Cu proves truly problematic, a ZnTe/Te or CdZnTe/Te bilayer may suffice. In this configuration, p-type doping and hole selectivity would be provided by the Te and *undoped* ZnTe, respectively.

CHAPTER 5. CONCLUSIONS AND FUTURE WORK

The focus of this dissertation has been on luminescence measurements (TRPL in particular) and how to best attain and utilize the information which these measurements can provide. This final chapter will summarize the most important findings and offer lessons for the future.

5.1 Summary of Primary Conclusions

5.1.1 Field-effect Influence in TRPL

As CdTe technology improves, interpretation of TRPL data becomes more difficult. For much of CdTe's history, it was reasonable to assume that the tail lifetime of a TRPL decay reflected solely the rate of nonradiative recombination due to defects primarily in the absorber bulk. However, with recent improvements in doping and even more substantial reductions in nonradiative recombination, this is no longer the case when measurements are performed on complete cells. Decreasing recombination rates and increasing field strengths with higher doping both enable p-n junction fields to more strongly influence carrier dynamics during a measurement. As the goal of a TRPL measurement is typically to determine recombination rates, the effect of fields is to obscure and obstruct the desired information. These effects are especially pernicious as in a standard measurement there is usually no obvious indication that the result is erroneous. This fact is not necessarily widely understood by the CdTe community, and the aim here is partly to demonstrate to CdTe researchers the potential pitfalls in interpretation using tail lifetime fits when measuring complete cells. It is important to have relatively detailed knowledge of what is being measured, and to take this knowledge into consideration.

Potential field effect influence on a measurement is not straightforward or trivial, yielding measured tail lifetimes that could either be artificially lower *or* higher than the true lifetime due to bulk defects. An artificially low lifetime results when the rate of carrier separation is similar to or greater than the rate of recombination. An artificially high lifetime is the result of “charge storage” whereby field-segregated carriers are prevented from recombining due to their separation. If it appears, charge storage will always present as the slowest part of the decay. The carrier separation effect on the other hand can influence the decay rate at nearly any time within the transient, depending on the circumstances. Charge storage is more difficult to model and is therefore less-well understood, though it appears more likely to manifest when the depletion width is narrower.

5.1.2 Strategies for Assisting TRPL Interpretation

Fortunately, field effects can be directly probed by measuring TRPL at a range of external electrical biases. While this measurement can be tedious and time consuming, the information gained is valuable. The incorporation of external bias serves two purposes. First, if a significant variation with bias modulation is observed, p-n junction fields must be influencing the measurement and therefore must be considered when interpreting results. At a given point in the decay, an increase in lifetime with forward bias signifies carrier separation while a decrease represents charge storage. Second, significant forward bias is effective in suppressing junction fields, eliminating this contribution to the measured lifetime. The applied bias at which this occurs is equivalent to the potential difference between the contacts of the cell at short circuit. While this precise voltage depends on the structure of the cell, experimentally a good estimate can be attained by gradually increasing bias and observing when trends in the measurement begin to reverse.

Junction fields can also be effectively suppressed by high optical injection. While this method is much easier to employ than forward electrical bias, increasing injection increases the rate of radiative recombination. This may obscure determination of the nonradiative recombination rate if the two rates become similar. Once again, this is more likely to be a problem when the rate of nonradiative recombination is low, as has been achieved by recent advances in CdTe technology. To obtain the lifetime due to bulk and/or interface defects, TRPL is therefore best measured at low injection under forward electrical bias ($\sim +1$ V for typical CdTe cell architectures).

Conversely, while *suppressing* junction fields is necessary for accurately extracting bulk lifetime, the ability to visualize fields with TRPL is also advantageous in its own way. Manipulating fields with bias during a series of TRPL measurements can produce a sort of abstract depiction of field strength and distribution within the cell with adept interpretation (especially if bolstered by modeling), and can give a representation of how carriers are moving. While fields are typically an unwanted nuisance in a TRPL measurement, the ability to probe their effects may sometimes be useful as an advanced characterization technique.

5.1.3 n-i-p Architecture for Improved Voltages

Measuring and characterizing recombination is vitally important. Purely optical luminescence measurements such as TRPL and ERE are compatible with nearly any stage of the cell fabrication process, which has proven invaluable. This ability has revealed excellent recombination performance in materials which are not utilized in typical cell structures. High-performing polycrystalline CdTe cells always use a CdSeTe/CdTe bilayer absorber doped p-type. However, the recombination behavior of CdSeTe alone before the doping process has been shown to be far superior to that of the typical absorber. Without p-type doping and a CdTe layer

behind it, this material delivers no J-V performance in a typical cell structure. However, its very low defect density signifies enormous potential which would have gone unseen without optical luminescence measurements. Hopefully this discovery will chart a new research course in CdTe photovoltaics, one that attempts to extract the performance potential from these materials by means of a new cell architecture which accommodates and exploits their capabilities.

To this end, an n-i-p structure is a logical approach. Such a structure utilizing an intrinsic CdSeTe absorber was thoroughly explored with simulations, demonstrating feasibility with real materials and identifying important material and design considerations. All three materials, the absorber, n- and p-type contacts, have specific requirements. In an n-i-p configuration, lifetime of the intrinsic absorber is vitally important – more important than with a p-n junction. Low to moderate lifetimes yield very low performance. That being said, the relaxation of the doping requirement makes very high lifetime much easier to attain. In an optimal configuration, lifetimes of $>1 \mu\text{s}$ are sufficient to obtain record-breaking cell efficiency and approach $1 \text{ V } V_{\text{OC}}$. These lifetimes have already been routinely observed in undoped polycrystalline CdSeTe. Hole mobility is also relatively important, to the extent that the hole diffusion length must be on the order of the absorber thickness to prevent current and fill factor loss. In this vein, the absorber should be as thin as possible while keeping current loss due to incomplete absorption of photons to a minimum. Given CdSeTe's excellent absorptivity, a thickness of $\sim 1 \mu\text{m}$ appears sufficient.

The n-type contact must be transparent, well-passivated, and electron-selective. These are the same requirements as with the traditional CdTe p-n junction configuration incorporating a thin highly-doped n-type window layer and a thick p-type absorber. The $\text{SnO}_2\text{:F/MgZnO}$ front contact typically utilized in this structure appears already perfectly suited to this new n-i-p architecture, so this layer was not explored with simulation. As the p-type contact layer is a new

component, there are no obvious established, well-optimized materials available for this role, so modeling was used to try and identify the most important attributes to aid in material selection. To ensure hole selectivity, it was discovered that the most important characteristic is band alignment with the CdSeTe absorber: an ideal material would permit a 0-eV valence band offset to allow unimpeded hole conduction and a >0.4-eV conduction band offset to block electron conduction. Reasonably high p-type doping is also necessary, and higher doping helps mitigate the detrimental effects of imperfect band positioning.

Based on these findings, ZnTe was identified as a good p-type contact candidate. Several cells utilizing the general $\text{SnO}_2:\text{F}/\text{MgZnO}/\text{CdSeTe}/\text{ZnTe}/\text{Ni}$ configuration were fabricated. While this architecture has obviously not achieved record-breaking performance yet, functioning cells with this structure were attained almost immediately, which is promising considering this work is still very much in its infancy. Fabricated cells exhibited good current collection and fill factor, indicating sufficient hole transport to the back of the cell enabled by adequate hole mobility and the absence of energy barriers. These first attempts altogether serve as a successful proof of concept. There is compelling evidence that the low voltage observed is likely due to a high concentration of defects introduced after ZnTe deposition, which suggests many possible avenues for improvement in the future.

5.2 Future Work

While there is certainly much more to learn about TRPL and there are several immediately apparent ways in which the simulation tool can be improved, continuing development of CdSeTe-absorber n-i-p structures is undoubtedly much more important at this time. As this particular venture is so new, there is a very large research space to explore. Both

the absorber and the p-type contact need to be studied and optimized, and there are many potential ways to go about this.

5.2.1 Repeatability of CdSeTe Deposition

Although very high lifetimes and EREs reported in Section 4.1 have been observed numerous times with good repeatability, CdSeTe deposition itself is very inconsistent [146]. The constituent materials of this ternary alloy do not sublime at the same rate due to differing vapor pressures, leading to changing selenium concentration in the source material over time, and thus inconsistent selenium concentrations in the deposited films. Apart from the obvious impacts on the deposited material's bandgap, interactions with CdCl₂ treatment and selenium-chlorine co-passivation are affected. In addition, the hexagonal crystalline phase of this material is preferentially formed at higher selenium concentration, and even small amounts of hexagonal formation are highly detrimental. Deposition rates also change substantially with changing selenium concentration and are typically very nonlinear with depth, making film thickness difficult to control. In addition to the constantly changing selenium concentration, CdSeTe films deposited by CSS exhibit high sensitivity to deposition conditions [146]. Size and geometry of grains is strongly dependent on substrate temperature during deposition. Large columnar grains appear more likely to create pinholes when the CdSeTe layer is thin. Grain geometry likely also impacts characteristics which are more difficult to determine, such as mobility. Material composition is sometimes observed to vary within the film, with significantly different bandgaps measured from the glass and film sides. However, like much else with this material, this effect is inconsistently observed even with nominally identical deposition conditions.

Unlike CdTe, deposition of CdSeTe is not well-controlled, at least for the moment. While these inconsistencies may be benign when very thin ($\leq 0.5 \mu\text{m}$) layers are used at the front of a

bilayer configuration, they will become much more problematic when employing CdSeTe-only absorbers. Ensuring good reproducibility of depositions of this material over time is essential for studying n-i-p structures, so getting a better handle on this material should be a high priority.

Further characterization of CdSeTe materials is also needed. As mentioned in previous chapters, the nature of very long lifetimes in this material needs to be better understood. In particular, the source of very bright sub-bandgap emission and evidently associated very low mobility needs to be identified, and the extent to which these features prevent realization of ideal performance needs to be determined.

5.2.2 Removal of Copper

For the hole-selective contact, Cu-doping of the ZnTe (or p-contact material in general) is problematic. While it does effectively dope the material sufficiently p-type, copper migration into the absorber forms an abundance of deep-level trap defects which significantly increases nonradiative recombination. While there may exist a material which can block copper migration between the absorber and ZnTe while not negatively impacting carrier conduction, it is likely more worthwhile to try and dope ZnTe with an element which does not diffuse as readily and/or does not form defects within CdTe. Nitrogen is the most obvious example, though there are several other elements which can be used to dope ZnTe p-type.

5.2.3 Addressing Back Interface Recombination

Passivation of the back interface was not directly explored with modeling, but it is certain to be important. The lattice mismatch between ZnTe and CdSeTe is likely to create persistent interface defects which will ultimately limit performance. Luckily ZnTe can be alloyed with CdTe to create the ternary alloy CdZnTe, whose lattice constant can be adjusted by varying the

concentration of zinc to perfectly match that of CdSeTe. This ternary alloy has a similar band structure to ZnTe and should allow comparable hole selectivity. This material can be made p-type with the same dopants as ZnTe, enabling a copper-free cell design.

Apart from ZnTe and CdZnTe, there are other potential hole-selective materials to consider. Organic semiconductors have been used as hole transport layers in niche research applications for several decades, with far more mainstream usage in perovskite photovoltaics over the last few years. Poly[bis(4-phenyl)(2,4,6-trimethylphenyl)amine (PTAA) is a fairly common perovskite hole contact which has been shown to form a relatively well-passivated interface with CdSeTe, as well as having favorable band alignment [204]. There exist hundreds of known organic semiconductors; a quite exhaustive list is provided in [205]. Conveniently, the band edges of polymer semiconductors – referred to as the “highest occupied molecular orbital” (HOMO) and “lowest unoccupied molecular orbital” (LUMO), equivalent to the valence and conduction band edges in inorganic semiconductors – are frequently reported as if they were essential properties (this information is not always easy to find for inorganic semiconductors). This is particularly useful as band structure is the most important requirement for the p-type material. An exhaustive literature search of HOMO and LUMO values may uncover a material (or several) unknown to the CdTe community perfectly suited to this application.

In addition to p-contact material selection, incorporation of passivating layers at the back interface may be beneficial or even necessary. Fortunately, CdSeTe films left in dry air will spontaneously form a thin TeO_x layer which appears to passivate the bare surface very well and is far more effective with CdSeTe than with CdTe [145], [146]. This passivation is crucial for attaining the high lifetimes measured in CdSeTe films with both front- and back-side excitation, though it alone is insufficient to provide hole selectivity, necessitating the subsequent deposition

of a p-contact layer. It is important to note that surface passivation benefits may not necessarily persist with another material behind the passivant, since deposition of the subsequent p-type layer can significantly alter or damage it.

5.2.4 Conclusion

In conclusion, this dissertation has put forward a comprehensive proposal with detailed explanations and justifications for every decision in the proposed cell design. A plan detailing near-term actions to follow this proposal is provided. Enhancing the reproducibility of and control over deposited CdSeTe films is a critical immediate step. As high voltage is contingent on low defect density, increased incorporation of luminescence measurements, particularly ERE, at as many points within the cell fabrication process as possible is vital for characterizing recombination and assessing depositions and treatments. Suitable hole contacts must be identified, evaluated, and optimized, to ultimately allow superb hole selectivity without compromising recombination behavior.

Despite being the standard in CdTe PV for many decades, a p-n structure with a p-type absorber is not an ideal solar cell configuration by any stretch. Doping the absorber p-type is an imperfect solution to a historic limitation, allowing respectable performance from defective materials. With recent advancements in passivation however, this solution is no longer necessary, and may even be impeding advancement. CdTe is experiencing a renaissance, with increased attention yielding significant improvement after over a decade of stagnation. Despite this laudable progress however, in many ways the technology is still struggling with many of the same limitations. At this juncture, it is pertinent to re-evaluate traditional methods and consider the state of materials available today. Tweaking and optimization of current architecture will likely not produce significant gains; it will take an altogether new approach to unlock the

voltages which CdTe-based materials are capable of. While this new direction comes with a new set of challenges, if CdTe can overcome its historic limitations and match or exceed the performance of silicon while using a small fraction of the material at a much lower cost, a sustainably powered future would be even closer within reach.

REFERENCES

- [1] J. Syvitski *et al.*, “Extraordinary human energy consumption and resultant geological impacts beginning around 1950 CE initiated the proposed Anthropocene Epoch,” *Nature Communications Earth & Environment*, vol. 1, no. 32, 2020.
- [2] M. Sato, “Thermochemistry of the formation of fossil fuels,” *Fluid-Mineral Interactions: A Tribute to H. P. Eugster, special publication of The Geochemical Society*, no. 2, 1990.
- [3] K. Vohra, A. Vodonos, J. Schwartz, E. Marais, M. Sulprizio, and L. Mickley, “Global mortality from outdoor fine particle pollution generated by fossil fuel combustion: Results from GEOS-Chem,” *Environmental Research*, vol. 195, p. 110754, 2021.
- [4] D. Lüthi *et al.*, “High-resolution carbon dioxide concentration record 650,000–800,000 years before present,” *Nature*, vol. 453, pp. 379–382, 2008.
- [5] R. Alley, P. Clark, P. Huybrechts, and I. Joughin, “Ice-Sheet and Sea-Level Changes,” *Science*, vol. 310, no. 5747, pp. 456–460, 2005.
- [6] P. Stott, “How climate change affects extreme weather events,” *Science*, vol. 352, no. 6293, pp. 1517–1518, 2016.
- [7] J. Rocklöv and R. Dubrow, “Climate change: an enduring challenge for vector-borne disease prevention and control,” *Nature Immunology*, vol. 21, no. 5, pp. 479–483, 2020.
- [8] K. Hubacek, G. Baiocchi, K. Feng, R. Muñoz Castillo, L. Sun, and J. Xue, “Global carbon inequality,” *Energy, Ecology and Environment*, vol. 2, no. 6, pp. 361–369, 2017.
- [9] S. Harlan, D. Pellow, J. Roberts, S. Bell, W. Holt, and J. Nagel, “Climate Justice and Inequality,” in *Climate Change and Society: Sociological Perspectives*, Oxford University Press, 2015.
- [10] “Overview of Greenhouse Gasses,” US Environmental Protection Agency. [Online]. Available: <https://www.epa.gov/ghgemissions/overview-greenhouse-gases>
- [11] M. Jacobson *et al.*, “100% clean and renewable wind, water, and sunlight (WWS) all-sector energy roadmaps for the 50 United States,” *Energy & Environmental Science*, vol. 8, no. 7, pp. 2093–2117, 2015.
- [12] M. Perez and R. Perez, “Update 2022 – A fundamental look at supply side energy reserves for the planet,” *Solar Energy Advances*, vol. 2, p. 100014, 2022.
- [13] R. Perez *et al.*, “Achieving very high PV penetration – The need for an effective electricity remuneration framework and a central role for grid operators,” *Energy Policy*, vol. 96, pp. 27–35, 2016.
- [14] O. Coddington, J. Lean, P. Pilewskie, M. Snow, and D. Lindholm, “A Solar Irradiance Climate Data Record,” *Bulletin of the American Meteorological Society*, vol. 97, no. 7, pp. 1265–1282, 2016.

- [15] “Earth by the Numbers.” NASA. [Online]. Available: <https://solarsystem.nasa.gov/planets/earth/by-the-numbers/>
- [16] “US Energy Information Administration’s 2021 International Energy Outlook.” 2021. [Online]. Available: https://www.eia.gov/outlooks/ieo/pdf/IEO2021_ChartLibrary_Consumption.pdf
- [17] S. Basu and H. Antia, “Helioseismology and solar abundances,” *Physics Reports*, vol. 457, no. 5, pp. 217–283, 2008.
- [18] “Main Sequence Lifetime.” The SAO Encyclopedia of Astronomy. [Online]. Available: <https://astronomy.swin.edu.au/cosmos/m/main+sequence+lifetime>
- [19] “Lazard’s Levelized Cost of Energy Analysis - Version 14.0,” Lazard, 2020.
- [20] D. Chapin, C. Fuller, and G. Pearson, “A New Silicon p-n Junction Photocell for Converting Solar Radiation into Electrical Power,” *Journal of Applied Physics*, vol. 25, pp. 676–677, 1954.
- [21] “2020 Photovoltaics Report,” Fraunhofer Institute for Energy Systems, Freiburg im Breisgau, Germany, 2021. [Online]. Available: <https://www.ise.fraunhofer.de/content/dam/ise/de/documents/publications/studies/Photovoltaics-Report.pdf>
- [22] G. Wilson *et al.*, “The 2020 photovoltaic technologies roadmap,” *Journal of Physics D: Applied Physics*, vol. 53, no. 49, p. 493001, 2020.
- [23] M. Nakamura, K. Yamaguchi, Y. Kimoto, Y. Yasaki, T. Kato, and H. Sugimoto, “Cd-Free Cu(In,Ga)(Se,S)₂ Thin-Film Solar Cell With Record Efficiency of 23.35%,” *IEEE Journal of Photovoltaics*, vol. 9, no. 6, pp. 1863–1867, 2019.
- [24] M. Green, E. Dunlop, J. Hohl-Ebinger, M. Yoshita, N. Kopidakis, and X. Hao, “Solar cell efficiency tables (version 57),” *Progress in Photovoltaics: Research and Applications*, vol. 29, no. 1, pp. 3–15, 2021.
- [25] J. Geisz *et al.*, “Six-junction III–V solar cells with 47.1% conversion efficiency under 143 Suns concentration,” *Nature Energy*, vol. 5, no. 4, pp. 326–335, 2020.
- [26] N. Papež, R. DALLAEV, Ş. Țălu, and J. Kaštyl, “Overview of the Current State of Gallium Arsenide-Based Solar Cells,” *Materials*, vol. 14, no. 11, p. 3075, 2021.
- [27] H.-S. Kim *et al.*, “Lead Iodide Perovskite Sensitized All-Solid-State Submicron Thin Film Mesoscopic Solar Cell with Efficiency Exceeding 9%,” *Scientific Reports*, vol. 2, no. 1, p. 591, 2012.
- [28] J. Yoo *et al.*, “Efficient perovskite solar cells via improved carrier management,” *Nature*, vol. 590, pp. 587–593, 2021.
- [29] G. Eperon, S. Stranks, C. Menelaou, M. Johnston, L. Herz, and H. Snaith, “Formamidinium lead trihalide: a broadly tunable perovskite for efficient planar

- heterojunction solar cells,” *Energy & Environmental Science*, vol. 7, no. 3, pp. 982–988, 2014.
- [30] A. Luque and S. Hegedus, *Handbook of Photovoltaic Science and Engineering*. John Wiley & Sons, 2011.
- [31] J. Peng, L. Lu, and H. Yang, “Review on life cycle assessment of energy payback and greenhouse gas emission of solar photovoltaic systems,” *Renewable and Sustainable Energy Reviews*, vol. 19, pp. 255–274, 2013.
- [32] M. de Wild-Scholten, “Energy payback time and carbon footprint of commercial photovoltaic systems,” *Solar Energy Materials and Solar Cells*, vol. 119, pp. 296–305, 2013.
- [33] P. Sinha, A. Meader, and M. de Wild-Scholten, “Life cycle water usage in CdTe photovoltaics,” in *2012 IEEE 38th Photovoltaic Specialists Conference*, 2012, pp. 1–4.
- [34] V. Fthenakis and H. Kim, “Life-cycle uses of water in U.S. electricity generation,” *Renewable and Sustainable Energy Reviews*, vol. 14, no. 7, pp. 2039–2048, 2010.
- [35] V. Fthenakis, “Could CdTe PV modules pollute the environment?,” National Photovoltaic Environmental Health and Safety Assistance Center, Brookhaven National Laboratory, Upton, NY, 2002.
- [36] P. Würfel, *Physics of Solar Cells*. Wiley-VCH, 2005.
- [37] “Best Research-Cell Efficiency Chart,” National Renewable Energy Lab. [Online]. Available: <https://www.nrel.gov/pv/cell-efficiency.html>
- [38] *Series 6 Plus Module Datasheet*. First Solar Inc., 2021. [Online]. Available: <https://www.firstsolar.com/-/media/First-Solar/Technical-Documents/Series-6-Plus/Series-6-Plus-Datasheet.ashx?la=en>
- [39] J. Burst *et al.*, “CdTe solar cells with open-circuit voltage breaking the 1 V barrier,” *Nature Energy*, vol. 1, no. 3, p. 16015, 2016.
- [40] R. Geisthardt, M. Topič, and J. Sites, “Status and Potential of CdTe Solar-Cell Efficiency,” *IEEE Journal of Photovoltaics*, vol. 5, no. 4, pp. 1217–1221, 2015.
- [41] J. Duenow *et al.*, “Relationship of Open-Circuit Voltage to CdTe Hole Concentration and Lifetime,” *IEEE Journal of Photovoltaics*, vol. 6, no. 6, pp. 1641–1644, 2016.
- [42] J. Duenow *et al.*, “Single-crystal CdTe solar cells with V_{oc} greater than 900 mV,” *Applied Physics Letters*, vol. 105, no. 5, p. 053903, 2014.
- [43] J. Burst *et al.*, “Interface Characterization of Single-Crystal CdTe Solar Cells With $V_{oc} > 950$ mV,” *IEEE Journal of Photovoltaics*, vol. 6, no. 6, pp. 1650–1653, 2016.
- [44] Y. Zhao *et al.*, “Monocrystalline CdTe solar cells with open-circuit voltage over 1 V and efficiency of 17%,” *Nature Energy*, vol. 1, no. 6, p. 16067, 2016.

- [45] J. Blakemore, *Solid State Physics*, 2nd ed. Cambridge University Press, 1985.
- [46] M. Green, *Solar Cells: Operating Principles, Technology, and System Applications*. University of New South Wales, 1986.
- [47] S. Hubbard, “Absorption and Generation,” in *Photovoltaic Solar Energy*, John Wiley & Sons, 2016, pp. 32–38.
- [48] A. Morales-Acevedo, “Thin film CdS/CdTe solar cells: Research perspectives,” *Solar Energy*, vol. 80, no. 6, pp. 675–681, 2006.
- [49] C. Gueymard, D. Myers, and K. Emery, “Proposed reference irradiance spectra for solar energy systems testing,” *Solar Energy*, vol. 73, no. 6, pp. 443–467, 2002.
- [50] U. Würfel, A. Cuevas, and P. Würfel, “Charge Carrier Separation in Solar Cells,” *IEEE Journal of Photovoltaics*, vol. 5, no. 1, pp. 461–469, 2015.
- [51] B. Streetman and S. Banerjee, *Solid State Electronic Devices*, 7th ed. Pearson, 2016.
- [52] A. Onno, C. Chen, P. Koswatta, M. Boccard, and Z. Holman, “Passivation, conductivity, and selectivity in solar cell contacts: Concepts and simulations based on a unified partial-resistances framework,” *Journal of Applied Physics*, vol. 126, no. 18, p. 183103, 2019.
- [53] R. Hall, “Recombination processes in semiconductors,” *Proceedings of the IEE - Part B: Electronic and Communication Engineering*, vol. 106, no. 17S, pp. 923–931, 1959.
- [54] S. Hubbard, “Recombination,” in *Photovoltaic Solar Energy*, John Wiley & Sons, 2016, pp. 39–46.
- [55] W. Dumke, “Spontaneous Radiative Recombination in Semiconductors,” *Physical Review*, vol. 105, no. 1, pp. 139–144, 1957.
- [56] T. Kinsel and I. Kudman, “Carrier recombination in gallium arsenide,” *Solid-State Electronics*, vol. 8, no. 10, pp. 797–801, 1965.
- [57] A. Richter, S. Glunz, F. Werner, J. Schmidt, and A. Cuevas, “Improved quantitative description of Auger recombination in crystalline silicon,” *Physical Review B*, vol. 86, no. 16, p. 165202, 2012.
- [58] I. Lifshitz and A. Kosevich, “The dynamics of a crystal lattice with defects,” *Reports on Progress in Physics*, vol. 29, no. 1, pp. 217–254, 1966.
- [59] W. Shockley and W. Read, “Statistics of the Recombinations of Holes and Electrons,” *Physical Review*, vol. 87, no. 5, pp. 835–842, 1952.
- [60] R. Hall, “Electron-Hole Recombination in Germanium,” *Physical Review*, vol. 87, no. 2, pp. 387–387, 1952.
- [61] A. Kanevce, M. Reese, T. Barnes, S. Jensen, and W. Metzger, “The roles of carrier concentration and interface, bulk, and grain-boundary recombination for 25% efficient CdTe solar cells,” *Journal of Applied Physics*, vol. 121, no. 21, p. 214506, 2017.

- [62] J. Moseley *et al.*, “Recombination by grain-boundary type in CdTe,” *Journal of Applied Physics*, vol. 118, no. 2, p. 025702, 2015.
- [63] L. Kazmerski, “The effects of grain boundary and interface recombination on the performance of thin-film solar cells,” *Solid-State Electronics*, vol. 21, no. 11, pp. 1545–1550, 1978.
- [64] J. Werner, K. Taretto, and U. Rau, “Grain Boundary Recombination in Thin-Film Silicon Solar Cells,” *Solid State Phenomena*, vol. 80–81, pp. 299–304, 2001.
- [65] L. Yujie, M. Guoli, and J. Wanqi, “Point defects in CdTe,” *Journal of Crystal Growth*, vol. 256, no. 3, pp. 266–275, 2003.
- [66] Y. Yan, M. Al-Jassim, and T. Demuth, “Energetics and effects of planar defects in CdTe,” *Journal of Applied Physics*, vol. 90, no. 8, pp. 3952–3955, 2001.
- [67] K. Jones, “Mismatch dislocations and lattice distortion for Cd(S, Se) films grown on (111), (110) and (001) InP substrates,” *Journal of Crystal Growth*, vol. 49, no. 3, pp. 522–530, 1980.
- [68] J.-H. Yang, W.-J. Yin, J.-S. Park, J. Ma, and S.-H. Wei, “Review on first-principles study of defect properties of CdTe as a solar cell absorber,” *Semiconductor Science and Technology*, vol. 31, no. 8, p. 083002, 2016.
- [69] J.-H. Yang, W. Metzger, and S.-H. Wei, “Carrier providers or killers: The case of Cu defects in CdTe,” *Applied Physics Letters*, vol. 111, no. 4, p. 042106, 2017.
- [70] W. Metzger, D. Albin, M. Romero, P. Dippo, and M. Young, “CdCl₂ treatment, S diffusion, and recombination in polycrystalline CdTe,” *Journal of Applied Physics*, vol. 99, no. 10, p. 103703, 2006.
- [71] I. Dharmadasa, “Review of the CdCl₂ Treatment Used in CdS/CdTe Thin Film Solar Cell Development and New Evidence towards Improved Understanding,” *Coatings*, vol. 4, no. 2, pp. 282–307, 2014.
- [72] P. Paulson and V. Dutta, “Study of in situ CdCl₂ treatment on CSS deposited CdTe films and CdS/CdTe solar cells,” *Thin Solid Films*, vol. 370, no. 1, pp. 299–306, 2000.
- [73] A. Shah, A. Nicholson, A. Thiyagarajan, and W. Sampath, “First Principles assisted modeling to understand Chlorine passivation of CdTe grain boundary,” in *2020 47th IEEE Photovoltaic Specialists Conference*, 2020, pp. 1760–1764.
- [74] J. Moseley *et al.*, “Cathodoluminescence Analysis of Grain Boundaries and Grain Interiors in Thin-Film CdTe,” *IEEE Journal of Photovoltaics*, vol. 4, no. 6, pp. 1671–1679, 2014.
- [75] T. Biduad, J. Moseley, M. Amarasinghe, M. Al-Jassim, W. Metzger, and S. Collin, “Imaging CdCl₂ defect passivation and formation in polycrystalline CdTe films by cathodoluminescence,” *Physical Review Materials*, vol. 5, no. 6, 2021.

- [76] J. Sites and J. Pan, “Strategies to increase CdTe solar-cell voltage,” *Thin Solid Films*, vol. 515, no. 15, pp. 6099–6102, 2007.
- [77] M. Gloeckler, I. Sankin, and Z. Zhao, “CdTe Solar Cells at the Threshold to 20% Efficiency,” *IEEE Journal of Photovoltaics*, vol. 3, no. 4, pp. 1389–1393, 2013.
- [78] J. Sites, A. Munshi, J. Kephart, D. Swanson, and W. Sampath, “Progress and challenges with CdTe cell efficiency,” in *2016 IEEE 43rd Photovoltaic Specialists Conference*, 2016, pp. 3632–3635.
- [79] D. O’Connor and D. Phillips, *Time-Correlated Single Photon Counting*. London, UK: Academic Press, 1984.
- [80] W. Becker, *Advanced Time-Correlated Single Photon Counting Techniques*. Springer, 2005.
- [81] K. Smith, “Photoluminescence of semiconductor materials,” *Thin Solid Films*, vol. 84, no. 2, pp. 171–182, 1981.
- [82] C. Swartz *et al.*, “Radiative and interfacial recombination in CdTe heterostructures,” *Applied Physics Letters*, vol. 105, no. 22, p. 222107, 2014.
- [83] D. Kuciauskas, J. Moseley, P. Ščajev, and D. Albin, “Radiative Efficiency and Charge-Carrier Lifetimes and Diffusion Length in Polycrystalline CdSeTe Heterostructures,” *physica status solidi Rapid Research Letters*, vol. 14, no. 3, p. 1900606, 2020.
- [84] M. DiNezza, X.-H. Zhao, S. Liu, A. Kirk, and Y.-H. Zhang, “Growth, steady-state, and time-resolved photoluminescence study of CdTe/MgCdTe double heterostructures on InSb substrates using molecular beam epitaxy,” *Applied Physics Letters*, vol. 103, no. 19, p. 193901, 2013.
- [85] P. Jundt, D. Kuciauskas, and J. Sites, “Effect of Diode Field on Time-Resolved Photoluminescence of CdTe-Based Solar Cells,” *IEEE Journal of Photovoltaics*, vol. 12, no. 2, pp. 501–511, 2022.
- [86] P. Jundt, D. Kuciauskas, and J. Sites, “Simulating the Effect of p-n Junction Fields on TRPL Transients of Thin-Film CdTe Solar Cells,” in *2020 47th IEEE Photovoltaic Specialists Conference (PVSC)*, 2020, pp. 1408–1412.
- [87] *Pharos User’s Manual*. Vilnius, Lithuania: Light Conversion Ltd., 2012.
- [88] *Orpheus User’s Manual*. Vilnius, Lithuania: Light Conversion Ltd., 2018.
- [89] M. Wahl, *Time-Correlated Single Photon Counting*. Berlin, Germany: PicoQuant GmbH, 2014.
- [90] *InGaAs Single-Photon Detection Module User’s Manual*, 4.0.2. Bolzano, Italy: Micro Photon Devices, 2014.

- [91] I. Repins *et al.*, “Fiber-fed time-resolved photoluminescence for reduced process feedback time on thin-film photovoltaics,” *Review of Scientific Instruments*, vol. 86, no. 1, p. 013907, 2015.
- [92] W. Metzger *et al.*, “Recombination kinetics and stability in polycrystalline Cu(In,Ga)Se₂ solar cells,” *Thin Solid Films*, vol. 517, no. 7, pp. 2360–2364, 2009.
- [93] D. Kuciauskas *et al.*, “Optical-fiber-based, time-resolved photoluminescence spectrometer for thin-film absorber characterization and analysis of TRPL data for CdS/CdTe interface,” in *2012 38th IEEE Photovoltaic Specialists Conference*, 2012, pp. 1721–1726.
- [94] T. Kirchartz, J. Márquez, M. Stolterfoht, and T. Unold, “Photoluminescence-Based Characterization of Halide Perovskites for Photovoltaics,” *Advanced Energy Materials*, vol. 10, no. 26, p. 1904134, 2020.
- [95] W. Metzger *et al.*, “Time-resolved photoluminescence studies of CdTe solar cells,” *Journal of Applied Physics*, vol. 94, no. 5, pp. 3549–3555, 2003.
- [96] R. Ahrenkiel and S. Johnston, “An optical technique for measuring surface recombination velocity,” *Solar Energy Materials and Solar Cells*, vol. 93, no. 5, pp. 645–649, 2009.
- [97] M. Reese *et al.*, “Surface Passivation of CdTe Single Crystals,” *IEEE Journal of Photovoltaics*, vol. 5, no. 1, pp. 382–385, 2015.
- [98] A. Kanevce, D. Levi, and D. Kuciauskas, “The role of drift, diffusion, and recombination in time-resolved photoluminescence of CdTe solar cells determined through numerical simulation,” *Progress in Photovoltaics: Research and Applications*, vol. 22, no. 11, pp. 1138–1146, 2014.
- [99] R. Ahrenkiel, “Minority-Carrier Lifetime in III–V Semiconductors,” in *Semiconductors and Semimetals*, vol. 39, R. Ahrenkiel and M. Lundstrom, Eds. Elsevier, 1993, pp. 39–150.
- [100] T. Weiss, B. Bissig, T. Feurer, R. Carron, S. Buecheler, and A. Tiwari, “Bulk and surface recombination properties in thin film semiconductors with different surface treatments from time-resolved photoluminescence measurements,” *Scientific Reports*, vol. 9, no. 1, p. 5385, 2019.
- [101] D. Kuciauskas, A. Kanevce, P. Dippo, S. Seyedmohammadi, and R. Malik, “Minority-Carrier Lifetime and Surface Recombination Velocity in Single-Crystal CdTe,” *IEEE Journal of Photovoltaics*, vol. 5, no. 1, pp. 366–371, 2015.
- [102] X.-H. Zhao, M. DiNezza, S. Liu, C. Campbell, Y. Zhao, and Y.-H. Zhang, “Determination of CdTe bulk carrier lifetime and interface recombination velocity of CdTe/MgCdTe double heterostructures grown by molecular beam epitaxy,” *Applied Physics Letters*, vol. 105, no. 25, p. 252101, 2014.
- [103] S. Sze and K. Ng, *Physics of Semiconductor Devices*, 3rd ed. Hoboken, NJ: John Wiley & Sons, 2006.

- [104] A. Marshak and D. Assaf, "A generalized Einstein relation for semiconductors," *Solid-State Electronics*, vol. 16, no. 6, pp. 675–679, 1973.
- [105] M. Maiberg, T. Hölscher, S. Zahedi-Azad, and R. Scheer, "Theoretical study of time-resolved luminescence in semiconductors. III. Trap states in the band gap," *Journal of Applied Physics*, vol. 118, no. 10, p. 105701, 2015.
- [106] R. Ahrenkiel, "Measurement of minority-carrier lifetime by time-resolved photoluminescence," *Solid-State Electronics*, vol. 35, no. 3, pp. 239–250, 1992.
- [107] R. Davies and F. Gentry, "Control of electric field at the surface of P-N junctions," *IEEE Transactions on Electron Devices*, vol. 11, no. 7, pp. 313–323, 1964.
- [108] M. Burgelman, P. Nollet, and S. Degrave, "Modelling polycrystalline semiconductor solar cells," *Thin Solid Films*, vol. 361–362, pp. 527–532, 2000.
- [109] T. Song, "Design Strategies for High-Efficiency CdTe Solar Cells," PhD dissertation, Colorado State University, 2017.
- [110] D. Kuciauskas *et al.*, "Microsecond Carrier Lifetimes in Polycrystalline CdSeTe Heterostructures and in CdSeTe Thin Film Solar Cells," in *2020 47th IEEE Photovoltaic Specialists Conference*, 2020, pp. 82–84.
- [111] M. Maiberg and R. Scheer, "Theoretical study of time-resolved luminescence in semiconductors. II. Pulsed excitation," *Journal of Applied Physics*, vol. 116, no. 12, p. 123711, 2014.
- [112] W. Metzger, M. Romero, P. Dippo, and M. Young, "Characterizing Recombination in CdTe Solar Cells with Time-Resolved Photoluminescence," in *2006 IEEE 4th World Conference on Photovoltaic Energy Conference*, 2006, pp. 372–375.
- [113] T. Ablekim *et al.*, "Tailoring MgZnO/CdSeTe Interfaces for Photovoltaics," *IEEE Journal of Photovoltaics*, vol. 9, no. 3, pp. 888–892, 2019.
- [114] D. Swanson *et al.*, "Single vacuum chamber with multiple close space sublimation sources to fabricate CdTe solar cells," *Journal of Vacuum Science & Technology A: Vacuum, Surfaces, and Films*, vol. 34, no. 2, p. 021202, 2016.
- [115] P. Hatton, M. Watts, A. Abbas, J. Walls, R. Smith, and P. Goddard, "Chlorine activated stacking fault removal mechanism in thin film CdTe solar cells: the missing piece," *Nature Communications*, vol. 12, no. 1, p. 4938, 2021.
- [116] M. Watts *et al.*, "Chlorine passivation of grain boundaries in cadmium telluride solar cells," *Physical Review Materials*, vol. 5, no. 3, p. 035403, 2021.
- [117] T. Song, A. Moore, and J. Sites, "Te Layer to Reduce the CdTe Back-Contact Barrier," *IEEE Journal of Photovoltaics*, vol. 8, no. 1, pp. 293–298, 2018.
- [118] J. Guo *et al.*, "Effect of selenium and chlorine co-passivation in polycrystalline CdSeTe devices," *Applied Physics Letters*, vol. 115, no. 15, p. 153901, 2019.

- [119] A. Munshi *et al.*, “Polycrystalline CdSeTe/CdTe Absorber Cells With 28 mA/cm² Short-Circuit Current,” *IEEE Journal of Photovoltaics*, vol. 8, no. 1, pp. 310–314, 2018.
- [120] A. Bothwell, J. Drayton, P. Jundt, and J. Sites, “Characterization of thin CdTe solar cells with a CdSeTe front layer,” *MRS Advances*, vol. 4, no. 37, pp. 2053–2062, 2019.
- [121] M. Maiberg, C. Spindler, E. Jarzembowski, and R. Scheer, “Electrical characterization of Cu(In,Ga)Se₂-solar cells by voltage dependent time-resolved photoluminescence,” *Thin Solid Films*, vol. 582, pp. 379–382, 2015.
- [122] D. Shvydka, V. Karpov, and A. Compaan, “Bias-dependent photoluminescence in CdTe photovoltaics,” *Applied Physics Letters*, vol. 80, no. 17, pp. 3114–3116, 2002.
- [123] G. Brill, Y. Chen, P. Amirtharaj, W. Sarney, D. Chandler-Horowitz, and N. Dhar, “Molecular beam epitaxial growth and characterization of Cd-based II–VI wide-bandgap compounds on Si substrates,” *Journal of Electronic Materials*, vol. 34, no. 5, pp. 655–661, 2005.
- [124] A. Nagaoka, D. Kuciauskas, J. McCoy, and M. Scarpulla, “High p-type doping, mobility, and photocarrier lifetime in arsenic-doped CdTe single crystals,” *Applied Physics Letters*, vol. 112, no. 19, p. 192101, 2018.
- [125] W. Metzger *et al.*, “Exceeding 20% efficiency with in situ group V doping in polycrystalline CdTe solar cells,” *Nature Energy*, vol. 4, no. 10, pp. 837–845, 2019.
- [126] B. McCandless *et al.*, “Overcoming Carrier Concentration Limits in Polycrystalline CdTe Thin Films with In Situ Doping,” *Scientific Reports*, vol. 8, no. 1, p. 14519, 2018.
- [127] A. Munshi *et al.*, “Doping CdSe_xTe_{1-x}/CdTe Graded Absorber Films with Arsenic for Thin-Film Photovoltaics,” in *2019 IEEE 46th Photovoltaic Specialists Conference*, 2019, pp. 28–31.
- [128] A. Mavlonov *et al.*, “Doping efficiency and limits in (Mg,Zn)O:Al,Ga thin films with two-dimensional lateral composition spread,” *physica status solidi (a)*, vol. 212, no. 12, pp. 2850–2855, 2015.
- [129] Y. Samoilenko *et al.*, “Stable magnesium zinc oxide by reactive Co-Sputtering for CdTe-based solar cells,” *Solar Energy Materials and Solar Cells*, vol. 210, p. 110521, 2020.
- [130] J. Kephart, J. McCamy, Z. Ma, A. Ganjoo, F. Alamgir, and W. Sampath, “Band alignment of front contact layers for high-efficiency CdTe solar cells,” *Solar Energy Materials and Solar Cells*, vol. 157, pp. 266–275, 2016.
- [131] A. Munshi *et al.*, “Polycrystalline CdTe photovoltaics with efficiency over 18% through improved absorber passivation and current collection,” *Solar Energy Materials and Solar Cells*, vol. 176, pp. 9–18, 2018.
- [132] E. Artegiani *et al.*, “Analysis of magnesium zinc oxide layers for high efficiency CdTe devices,” *Thin Solid Films*, vol. 672, pp. 22–25, 2019.

- [133] A. Kanevce, D. Kuciauskas, T. Gessert, D. Levi, and D. Albin, “Impact of interface recombination on time resolved photoluminescence (TRPL) decays in CdTe solar cells (numerical simulation analysis),” in *2012 38th IEEE Photovoltaic Specialists Conference*, 2012, pp. 848–853.
- [134] D. Kuciauskas *et al.*, “Charge-carrier dynamics in polycrystalline thin-film $\text{CuIn}_{1-x}\text{Ga}_x\text{Se}_2$ photovoltaic devices after pulsed laser excitation: Interface and space-charge region analysis,” *Journal of Applied Physics*, vol. 117, no. 18, p. 185102, 2015.
- [135] B. Paez, “Thermoelectric Power and Hall Effect Measurements in Polycrystalline CdTe Thin Films,” *physica status solidi (b)*, vol. 220, no. 1, pp. 221–225, 2000.
- [136] C. Jácome, J. Flórez, and G. Gordillo, “Study of electrical transport properties in polycrystalline CdTe thin films,” *Thin Solid Films*, vol. 396, no. 1, pp. 257–263, 2001.
- [137] Q. Long, S. Dinca, E. Schiff, M. Yu, and J. Theil, “Electron and hole drift mobility measurements on thin film CdTe solar cells,” *Applied Physics Letters*, vol. 105, no. 4, p. 042106, 2014.
- [138] P. Ščajev *et al.*, “Excitation-dependent carrier lifetime and diffusion length in bulk CdTe determined by time-resolved optical pump-probe techniques,” *Journal of Applied Physics*, vol. 123, no. 2, p. 025704, 2018.
- [139] J. Moseley, D. Krasikov, C. Lee, and D. Kuciauskas, “Diverse simulations of time-resolved photoluminescence in thin-film solar cells: A $\text{SnO}_2/\text{CdSe}_y\text{Te}_{1-y}$ case study,” *Journal of Applied Physics*, vol. 130, no. 16, p. 163105, 2021.
- [140] M. Green, “Radiative efficiency of state-of-the-art photovoltaic cells,” *Progress in Photovoltaics: Research and Applications*, vol. 20, no. 4, pp. 472–476, 2012.
- [141] P. Würfel, “The chemical potential of radiation,” *Journal of Physics C: Solid State Physics*, vol. 15, no. 18, pp. 3967–3985, 1982.
- [142] A. Onno *et al.*, “Understanding what limits the voltage of polycrystalline CdSeTe solar cells,” *Nature Energy*, vol. 7, no. 5, pp. 400–408, 2022.
- [143] C. Reich *et al.*, “Photoluminescence Study of the $\text{Mg}_x\text{Zn}_{1-x}\text{O}/\text{CdSe}_y\text{Te}_{1-y}$ Interface: The Effect of Oxide Bandgap and Resulting Band Alignment,” in *2021 IEEE 48th Photovoltaic Specialists Conference*, 2021, pp. 1468–1471.
- [144] W. Shockley and H. Queisser, “Detailed Balance Limit of Efficiency of p-n Junction Solar Cells,” *Journal of Applied Physics*, vol. 32, no. 3, pp. 510–519, 1961.
- [145] C. Reich, “Investigations to Improve CdTe-Based Solar Cell Open Circuit Voltage and Efficiency Using a Passivation and Selectivity Theoretical Framework,” PhD dissertation, Colorado State University, 2022.
- [146] A. Danielson, “Investigation of Group V Doping and Passivating Oxides to Reduce the Voltage Deficit in CdTe Solar Cells,” PhD dissertation, Colorado State University, 2022.

- [147] T. Fiducia *et al.*, “Understanding the role of selenium in defect passivation for highly efficient selenium-alloyed cadmium telluride solar cells,” *Nature Energy*, vol. 4, no. 6, pp. 504–511, 2019.
- [148] M. Yamaguchi, K.-H. Lee, K. Araki, N. Kojima, H. Yamada, and Y. Katsumata, “Analysis for efficiency potential of high-efficiency and next-generation solar cells,” *Progress in Photovoltaics: Research and Applications*, vol. 26, no. 8, pp. 543–552, 2018.
- [149] D. deQuilettes *et al.*, “Maximizing the external radiative efficiency of hybrid perovskite solar cells,” *Pure and Applied Chemistry*, vol. 92, no. 5, pp. 697–706, 2020.
- [150] M. Green and A. Ho-Baillie, “Pushing to the Limit: Radiative Efficiencies of Recent Mainstream and Emerging Solar Cells,” *ACS Energy Letters*, vol. 4, no. 7, pp. 1639–1644, 2019.
- [151] D. Kuciauskas, J. Moseley, and C. Lee, “Identification of Recombination Losses in CdSe/CdTe Solar Cells from Spectroscopic and Microscopic Time-Resolved Photoluminescence,” *Solar RRL*, vol. 5, no. 4, p. 2000775, 2021.
- [152] G. Dummer, *Electronic Inventions and Discoveries: Electronics from its Earliest Beginnings to the Present Day*, 3rd ed. Elsevier, 1983.
- [153] B. von Roedern, “Physics of Photovoltaic Materials,” *Encyclopedia of Energy*, pp. 47–59, 2004.
- [154] D. Shi, Z. Guo, and N. Bedford, “Nanoenergy Materials,” *Nanomaterials and Devices*, pp. 255–291, 2015.
- [155] Y. Petukhov and W. Krop, “The research of polarization in CdTe P-I-N detectors of nuclear radiation,” in *2008 IEEE Nuclear Science Symposium Conference Record*, 2008, pp. 263–268.
- [156] S. Liu, X.-H. Zhao, C. Campbell, M. Lassise, Y. Zhao, and Y.-H. Zhang, “Carrier lifetimes and interface recombination velocities in CdTe/Mg_xCd_{1-x}Te double heterostructures with different Mg compositions grown by molecular beam epitaxy,” *Applied Physics Letters*, vol. 107, no. 4, p. 041120, 2015.
- [157] A. Kirk, *Solar Photovoltaic Cells: Photons to Electricity*. Academic Press, 2014.
- [158] Y. Zhao, V. Wang, and A. Javey, “Molecular Materials with Short Radiative Lifetime for High-Speed Light-Emitting Devices,” *Matter*, vol. 3, no. 6, pp. 1832–1844, 2020.
- [159] J. Almutlaq *et al.*, “CsMnBr₃: Lead-Free Nanocrystals with High Photoluminescence Quantum Yield and Picosecond Radiative Lifetime,” *ACS Materials Letters*, vol. 3, no. 3, pp. 290–297, 2021.
- [160] G. Smestad and H. Ries, “Luminescence and current-voltage characteristics of solar cells and optoelectronic devices,” *Solar Energy Materials and Solar Cells*, vol. 25, no. 1, pp. 51–71, 1992.

- [161] R. Brendel and H. Queisser, "On the thickness dependence of open circuit voltages of p-n junction solar cells," *Solar Energy Materials and Solar Cells*, vol. 29, no. 4, pp. 397–401, 1993.
- [162] N. Amin, A. Yamada, and M. Konagai, "Effect of ZnTe and CdZnTe Alloys at the Back Contact of 1- μ m-Thick CdTe Thin Film Solar Cells," *Japanese Journal of Applied Physics*, vol. 41, no. 5R, pp. 2834–2841, 2002.
- [163] A. Bothwell, J. Drayton, and J. Sites, "Performance Analysis of 0.4–1.2- μ m CdTe Solar Cells," *IEEE Journal of Photovoltaics*, vol. 10, no. 1, pp. 259–266, 2020.
- [164] R. Anderson, "Germanium-Gallium Arsenide Heterojunctions [Letter to the Editor]," *IBM Journal of Research and Development*, vol. 4, no. 3, pp. 283–287, 1960.
- [165] J. Davies, *The Physics of Low-dimensional Semiconductors: An Introduction*. Cambridge, UK: Cambridge University Press, 1998.
- [166] A. Banerjee and K. Chattopadhyay, "Recent developments in the emerging field of crystalline p-type transparent conducting oxide thin films," *Progress in Crystal Growth and Characterization of Materials*, vol. 50, no. 1, pp. 52–105, 2005.
- [167] H. Kawazoe, M. Yasukawa, H. Hyodo, M. Kurita, H. Yanagi, and H. Hosono, "P-type electrical conduction in transparent thin films of CuAlO₂," *Nature*, vol. 389, pp. 939–942, 1997.
- [168] S. Chen, T. Kuo, Y. Lin, and H. Lin, "Preparation and properties of p-type transparent conductive Cu-doped NiO films," *Thin Solid Films*, vol. 519, no. 15, pp. 4944–4947, 2011.
- [169] Di Xiao, X. Li, D. Wang, Q. Li, K. Shen, and D. Wang, "CdTe thin film solar cell with NiO as a back contact buffer layer," *Solar Energy Materials and Solar Cells*, vol. 169, pp. 61–67, 2017.
- [170] E. Hassan, A. Saeed, and A. Elttayef, "Doping and thickness variation influence on the structural and sensing properties of NiO film prepared by RF-magnetron sputtering," *Journal of Materials Science: Materials in Electronics*, vol. 27, no. 2, pp. 1270–1277, 2016.
- [171] M. Thomas and B. Ralph, "A study of the sputtering of copper–nickel using a combination of techniques," *Journal of Vacuum Science & Technology*, vol. 21, no. 4, pp. 986–993, 1982.
- [172] V. Drobny and L. Pulfrey, "Properties of reactively-sputtered copper oxide thin films," *Thin Solid Films*, vol. 61, no. 1, pp. 89–98, 1979.
- [173] D. Rioux, D. Niles, and H. Höchst, "ZnTe: A potential interlayer to form low resistance back contacts in CdS/CdTe solar cells," *Journal of Applied Physics*, vol. 73, no. 12, pp. 8381–8385, 1993.

- [174] B. Späth, J. Fritsche, A. Klein, and W. Jaegermann, “Nitrogen doping of ZnTe and its influence on CdTe/ZnTe interfaces,” *Applied Physics Letters*, vol. 90, no. 6, p. 062112, 2007.
- [175] T. Duc, C. Hsu, and J. Faurie, “Linearity (commutativity and transitivity) of valence-band discontinuity in heterojunctions with Te-based II-VI semiconductors: CdTe, HgTe, and ZnTe,” *Physical Review Letters*, vol. 58, no. 11, pp. 1127–1130, 1987.
- [176] T. Shimpi, J. Drayton, D. Swanson, and W. Sampath, “Properties of Nitrogen-Doped Zinc Telluride Films for Back Contact to Cadmium Telluride Photovoltaics,” *Journal of Electronic Materials*, vol. 46, no. 8, pp. 5112–5120, 2017.
- [177] A. Kindvall, A. Munshi, T. Shimpi, A. Danielson, and W. Sampath, “Effect of Process Temperature and Copper Doping on the Performance of ZnTe:Cu Back Contacts in CdTe Photovoltaics,” in *2019 IEEE 46th Photovoltaic Specialists Conference*, 2019, pp. 189–192.
- [178] O. Oklobia, G. Kartopu, and S. Irvine, “Properties of Arsenic-Doped ZnTe Thin Films as a Back Contact for CdTe Solar Cells,” *Materials*, vol. 12, no. 22, p. 3706, 2019.
- [179] J. Tang, D. Mao, T. Ohno, V. Kaydanov, and J. Trefny, “Properties of ZnTe:Cu thin films and CdS/CdTe/ZnTe solar cells,” in *Conference Record of the Twenty Sixth IEEE Photovoltaic Specialists Conference - 1997*, 1997, pp. 439–442.
- [180] T. Gessert, W. Metzger, P. Dippo, S. Asher, R. Dhere, and M. Young, “Dependence of carrier lifetime on Cu-contacting temperature and ZnTe:Cu thickness in CdS/CdTe thin film solar cells,” *Thin Solid Films*, vol. 517, no. 7, pp. 2370–2373, 2009.
- [181] J. Burst *et al.*, “The effect of CdTe growth temperature and ZnTe:Cu contacting conditions on CdTe device performance,” in *2012 38th IEEE Photovoltaic Specialists Conference*, 2012, pp. 188–191.
- [182] S. Uličná, P. Isherwood, P. Kaminski, J. Walls, J. Li, and C. Wolden, “Development of ZnTe as a back contact material for thin film cadmium telluride solar cells,” *Vacuum*, vol. 139, pp. 159–163, 2017.
- [183] P. Meyers, “Polycrystalline thin film cadmium telluride n-i-p solar cells,” Solar Energy Research Institute, Golden, CO, 1990.
- [184] P. Meyers, “Design of a thin film CdTe solar cell,” *Solar Cells*, vol. 23, no. 1, pp. 59–67, 1988.
- [185] P. Meyers, “Advances in CdTe n-i-p photovoltaics,” *Solar Cells*, vol. 27, no. 1, pp. 91–98, 1989.
- [186] V. Ramanathan, L. Russell, C. Liu, and P. Meyers, “Indoor stability tests on CdS/CdTe/ZnTe n-i-p submodules,” *Solar Cells*, vol. 28, no. 2, pp. 129–133, 1990.
- [187] M. Simmons, H. Al Allak, A. Brinkman, and K. Durose, “Electrical and optical characterisation of epitaxial ZnTe/CdTe/CdS and ZnTe/CdTe/GaAs p-i-n solar cell

- structures grown by metalorganic vapour phase epitaxy,” *Journal of Crystal Growth*, vol. 117, no. 1, pp. 959–963, 1992.
- [188] D. Goren, G. Asa, and Y. Nemirovsky, “Photocurrent in CdTe NIP solar cells,” *Solar Energy Materials and Solar Cells*, vol. 60, no. 4, pp. 367–377, 2000.
- [189] T. Gessert, A. Mason, P. Sheldon, A. Swartzlander, D. Niles, and T. Coutts, “Development of Cu-doped ZnTe as a back-contact interface layer for thin-film CdS/CdTe solar cells,” *Journal of Vacuum Science & Technology A: Vacuum, Surfaces, and Films*, vol. 14, no. 3, pp. 806–812, 1996.
- [190] R. Bohn, C. Tabory, C. Deak, M. Shao, A. Compaan, and N. Reiter, “RF sputtered films of Cu-doped and N-doped ZnTe,” in *Proceedings of 1994 IEEE 1st World Conference on Photovoltaic Energy Conversion - WCPEC (A Joint Conference of PVSC, PVSEC and PSEC)*, 1994, vol. 1, pp. 354–356.
- [191] S. Demtsu, D. Albin, J. Sites, W. Metzger, and A. Duda, “Cu-related recombination in CdS/CdTe solar cells,” *Thin Solid Films*, vol. 516, no. 8, pp. 2251–2254, 2008.
- [192] J. Burst *et al.*, “Carrier density and lifetime for different dopants in single-crystal and polycrystalline CdTe,” *APL Materials*, vol. 4, no. 11, p. 116102, 2016.
- [193] D. Kuciauskas *et al.*, “The impact of Cu on recombination in high voltage CdTe solar cells,” *Applied Physics Letters*, vol. 107, no. 24, p. 243906, 2015.
- [194] E. Jones, N. Stewart, and J. Mullin, “The diffusion of copper in cadmium telluride,” *Journal of Crystal Growth*, vol. 117, no. 1, pp. 244–248, 1992.
- [195] A. Barati, A. Klein, and W. Jaegermann, “Deposition and characterization of highly p-type antimony doped ZnTe thin films,” *Thin Solid Films*, vol. 517, no. 7, pp. 2149–2152, 2009.
- [196] E. Deligoz, K. Colakoglu, and Y. Ciftci, “Elastic, electronic, and lattice dynamical properties of CdS, CdSe, and CdTe,” *Physica B: Condensed Matter*, vol. 373, no. 1, pp. 124–130, 2006.
- [197] M. Watts, T. Fiducia, B. Sanyal, R. Smith, J. Walls, and P. Goddard, “Enhancement of photovoltaic efficiency in CdSe_xTe_{1-x} (where 0 ≤ x ≤ 1): insights from density functional theory,” *Journal of Physics: Condensed Matter*, vol. 32, no. 12, p. 125702, 2020.
- [198] A. Denton and N. Ashcroft, “Vegard’s law,” *Physical Review A*, vol. 43, no. 6, pp. 3161–3164, 1991.
- [199] D. Noda, T. Aoki, Y. Nakanishi, and Y. Hatanaka, “Epitaxial Growth and Nitrogen Radical Doping of CdZnTe,” *Journal of The Electrochemical Society*, vol. 146, no. 9, pp. 3482–3484, 1999.
- [200] F. Alfadhili *et al.*, “Potential of CdZnTe Thin Film Back Buffer Layer for CdTe Solar Cells,” in *2019 IEEE 46th Photovoltaic Specialists Conference*, 2019, pp. 140–143.

- [201] S. Stolyarova *et al.*, “Structure of CdZnTe films on glass,” *Journal of Physics D: Applied Physics*, vol. 41, no. 6, p. 065402, 2008.
- [202] A. Bansal and P. Rajaram, “Electrochemical growth of CdZnTe thin films,” *Materials Letters*, vol. 59, no. 28, pp. 3666–3671, 2005.
- [203] H.-G. Junginger, “Electronic band structure of tellurium,” *Solid State Communications*, vol. 5, no. 7, pp. 509–511, 1967.
- [204] J. Hack, C. Lee, S. Grover, and G. Xiong, “Hole Transport Material for Passivated Back Contacts on CdTe Solar Cells,” in *2021 IEEE 48th Photovoltaic Specialists Conference*, 2021, pp. 1880–1882.
- [205] L. Nhari, R. El-Shishtawy, and A. Asiri, “Recent progress in organic hole transport materials for energy applications,” *Dyes and Pigments*, vol. 193, p. 109465, 2021.

PUBLICATIONS

Journal Publications

P. Jundt, D. Kuciauskas, and J. Sites, “Effect of diode field on time-resolved photoluminescence of CdTe-based solar cells,” in *IEEE Journal of Photovoltaics*, 2022.

R. Pandey, A. Shah, A. Munshi, T. Shimpi, **P. Jundt**, J. Guo, R. Klie, W. Sampath, and J. Sites, “Mitigation of J-V distortion in CdTe solar cells by Ga-doping of MgZnO emitter,” in *Solar Energy Materials and Solar Cells*, 2021.

A. Bothwell, J. Drayton, **P. Jundt**, and J. Sites, “Close-space sublimation-deposited ultra-thin CdSeTe/CdTe solar cells for enhanced short-circuit current density and photoluminescence,” in *Journal of Visualized Experiments*, 2020.

A. Bothwell, J. Drayton, **P. Jundt**, and J. Sites, “Characterization of thin CdTe solar cells with a CdSeTe front layer,” in *MRS Advances*, 2019.

Conference Proceedings

P. Jundt and J. Sites, “Leveraging undoped CdSeTe for >950 mV,” at *IEEE 49th Photovoltaic Specialists Conference*, 2022.

P. Jundt, R. Pandey, A. Munshi, and J. Sites, “Transparent buffer layer for back surface passivation in CdTe photovoltaics,” at *IEEE 48th Photovoltaic Specialists Conference*, 2021.

R. Pandey, A. Shah, A. Munshi, **P. Jundt**, T. Shimpi, D. Kuciauskas, and J. Sites, “Transparent MgO for back-contact passivation of CdTe-based solar cells,” at *IEEE 48th Photovoltaic Specialists Conference*, 2021.

P. Jundt, D. Kuciauskas, and J. Sites, “Simulating the effects of pn junction fields on TRPL transients of thin-film CdTe solar cells,” at *IEEE 47th Photovoltaic Specialists Conference*, 2020.

A. Bothwell, J. Drayton, **P. Jundt**, and J. Sites, “CdMgTe as an electron reflector for MgZnO/CdSeTe/CdTe Solar Cells,” at *IEEE 46th Photovoltaic Specialists Conference*, 2019.

J. Sites and **P. Jundt**, “Device structure of high-efficiency thin-film CdTe solar cells,” at *UK-ISES 15th Photovoltaic Science, applications, and Technology Conference*, 2019.

LIST OF ABBREVIATIONS

Abbreviation	Description
AM1.5	“air mass 1.5” solar irradiance spectrum
APD	avalanche photodiode
CBO	conduction band offset
CSS	close-space sublimation
CSU	Colorado State University
DH	double-heterostructure
ERE	external radiative efficiency
FTO	fluorine-doped tin oxide ($\text{SnO}_2\text{:F}$)
IRF	instrument response function
J-V	current-voltage curve
NREL	National Renewable Energy Lab
OPA	optical parametric amplifier
PDE	partial differential equation
PL	(steady-state) photoluminescence
PV	photovoltaics
RA	regenerative amplifier
SRH	Shockley-Read-Hall (recombination)
TCO	transparent conductive oxide
TCSPC	time-correlated single photon counting
TRPL	time-resolved photoluminescence
VBO	valence band offset